DYNAMICS OF AGGREGATION IN SHEARED ALBUMIN-FIBRONECTIN THIN FILMS

By

Naveena Janakiraman Narayanan

A thesis submitted to the University of Ottawa

in partial fulfillment of the requirements for

Master of Applied Science

in

Biomedical Engineering

FACULTY OF ENGINEERING

UNIVERSITY OF OTTAWA

Abstract

Articular joints are one of the most robust bearing systems found in the natural world. Healthy joints can withstand over 100 million shearing and compressive cycles without wear. This phenomenal lubrication is due to both the cartilage that forms the bearing surface and the synovial fluid (SF) that lubricates the joint. Common approaches that seek to elucidate such remarkable lubrication usually focus on the roles of high molecular weight SF components such as lubricin and hyaluronic acid, however, recent work in our group reports that the smaller globular protein serum albumin (SA) is crucial in mimicking the lubrication behaviour of SF, in particular the formation of shear-induced aggregates.

This finding is relevant for artificial joint lubrication because protein aggregates have been recognised to improve wear protection between metal surfaces in-vitro. In this thesis, we investigated the structural, mechanical, and lubrication properties of shear-induced SA aggregates. More specifically, we used the Surface Forces Apparatus and Confocal Microscopy to investigate in detail the response of SA thin films when confined and sheared between model surfaces coated with fibronectin (FN), a glycoprotein present in the superficial zone of cartilage.

Our data indicate that, under shear, SA films exhibit instantaneous thickening (dilation) and systematic formation of numerous aggregates accompanied by low friction and efficient surface protection against damage. Additionally, our detailed investigation of shearing conditions reveals that (i) aggregates are comprised of both SA and FN, most likely denatured/unfolded, (ii) aggregates material properties (stiffness, size, shape) are FN concentration-dependent, and (iii) aggregates formation is irreversible, which makes them long-lived (though mobile) and acting as robust ball bearings at the shearing interface.

Collectively, our results provide experimental evidence of the complementary roles of both the lubricant and the bearing surface properties in lubrication. Although our findings are based on experiments involving rigid, nonporous surfaces which can hardly be generalized to compliant and porous cartilage surfaces, they apply to other rigid tribosystems such as artificial joints and will certainly advance our understanding of joint implants' lubrication in SF mediated by protein aggregation, with implications for the future design of artificial joints and therapeutic interventions.

Table of Contents

List of Figures

List of Tables

List of Abbreviations

SF Synovial fluid

OA Osteoarthritis

RA Rheumatoid arthritis

NSAIDs Nonsteroidal anti-inflammatory drug

DMARDs (Disease-modifying anti-rheumatic drugs)

SA Serum albumin

SFA Surface Forces Apparatus

ECF Extracellular fluids

ICF Intracellular fluids

HA Hyaluronic acid

LA Lubricin

PL Phospholipids

HSA Human Serum Albumin

BSA Bovine Serum Albumin

FN Fibronectin

PBS Phosphate Buffer Saline

AFM Atomic force microscopy

FECO Fringes of equal chromatic order

Cu-Be Copper-Beryllium

CLSM Confocal laser scanning microscopy

UHMWPE Ultra High Molecular Weight Polyethylene

P1 Protocol 1

P2 Protocol 2

P2-P Protocol 3

P3 Protocol 4

P3-P Protocol 5

Acknowledgements

First, I would like to express my sincere gratitude to my mentor Dr. Delphine Gourdon, for providing me with essential support both personally and academically without which this study would not have been possible. Her approach to problem-solving and academic proficiency was influential for my evolution as a researcher. I will forever be grateful for the rewarding experience I had working under her. I acknowledge the Natural Sciences and Engineering Research Council of Canada (NSERC) Discovery Grant for supporting this work financially.

Following which, I extend my gratitude to my marvellous colleagues Parisa Sadeghi, who ever so graciously travelled with me throughout this whole journey, Halimo Aden, who supported me in all of my decisions, Dr. Elie Ngandu Mpoyi, who always made sure we got our dose of positivity and finally Mihir Samak for teaching me the fundamentals of Surface Force Apparatus. Secondly, I would like to thank my friends like family, Aadhi, my wonderful roommates Tharika, Mathura, Nandhinee for constantly feeding me with their love, support, and delicious food. I am thankful for my buddies, for their constant support and laughter which got me through my roughest times. Thirdly, I am grateful for my grandparents, the standing pillars of my family, to my late grandpa Krishnamoorthy, who believed in me. Vasanthi ammama, Janakiraman thatha, Rukumani nannamma, thankful for the eternal love they shower on me and keeping me in their prayers.

Special thanks to Avinesh Suresh, for whom I will be perpetually grateful for a never-ending supply of positive driving force, his immense patience and constant comfort. Thank you for making me feel at home even during a pandemic.

Finally, the most dynamic duos in my life, Kalpana and Narayanan, without whom I would not be standing here today proudly presenting my work. Thank you for your strong foundation, endless encouragement, and unconditional love. I am indebted to the countless sacrifices made by my mom, and innumerable hard work put in by my dad in helping me be the person I am today. They are my greatest treasures ever and I am thankful for them every day.

"*Life is a circle*" – have faith through hard times; good times are on the way.

Chapter 1 – Introduction

1.1 Overview and Motivation

Synovial fluid (SF), also called synovia, is defined as the semi-transparent viscous fluid (egg white-like consistency) found in the cavities of synovial joints. Within the joints, the SF has lubricating, metabolic, and regulatory functions[1]. SF is also known for protecting the joints' surfaces. The SF that fills the joint capsule lubricates the articular cartilage, which is a soft tissue that lines the ends of our long bones and forms the bearing surface in synovial joints such as the knee and hip joint[2]. The articular cartilage, along with SF, forms one of the most extraordinary lubricating systems. Few examples to understand the extent of this exceptional lubrication would be to imagine supporting a 1-ton weight on our hands and being able to slide it along our palm with just a push of a finger. To perform such an act requires roughly the level of lubrication that is being provided in the majority of healthy joints of our body[3]. Another remarkable example would be the friction coefficient (namely the ratio of the force of friction between two bodies and the force pressing them together), which is five times lower for cartilage sliding against cartilage than for ice against ice[4]. The composition and structure of both the cartilage and the SF contribute to this efficient lubrication. Additionally, another notable characteristic of the SF-cartilage system is its longevity, since it can withstand over 100 million shearing and loading cycles[5]. No human-made engineered bearing or material can match the ultra-low friction and durability of the naturally occurring synovial joints.

Unfortunately, healthy joints do not last for a full lifetime, and diseases and/or injury in joints can result in pain and dysfunction. Osteoarthritis (OA) is a degenerative disease that leads to destructive changes to the joint structure[1]. OA is the most common joint disease worldwide, affecting an estimated 10% of men and 18% of women over 60 years of age[6]. OA leads to severe pain, loss of joint function, and limited mobility with a direct impact on the quality of life due to the comorbidities associated with it, such as obesity and hypertension[7]. Another notable disease that affects synovial joints is Rheumatoid arthritis (RA) which is a chronic systemic autoimmune disease. RA is characterized by joint swelling, joint tenderness, and destruction of synovial joints[1]. Together with OA, RA impacts the quality of life leading to progressive disability, premature death, and socioeconomic burdens[8]. Traumatic joint injury

can also result in cartilage damage, articular and bone fractures, damage to soft tissues such as ligaments and menisci, and lesions in the joint capsule and synovium[1]. Contrasting to that of natural joints, lubrication, and protection of artificial joints/implants proves to be a struggle, leading to critical problems such as surface wear and implant loosening. Despite improvements of both the design and the material(s) used in implants, nano- and micro- wear debris occurring at the shearing interface remains a serious health constraint[9]. In a majority of patients, these wear debris are unfortunately associated with osteolysis (bone desorption), leading to reduced joint functions and eventually to implant failure[10].

Despite being one of the most studied and more ubiquitous conditions of our population, OA still does not have clear pathophysiology or a single most efficient intervention to treat the symptoms and degeneration associated with the disease[6,11,12]. The current approaches focus on extending the functional lifetime of the joint rather than finding a cure for the disease. Therapeutic instructions include physical therapy, non-steroidal anti-inflammatory drugs (NSAIDs), corticosteroid injections, viscosupplementation, and arthroplasty depending on the severity of the disease. Likewise, there also exists no cure for RA, and rheumatologists need to monitor the disease activity continuously and accurately to adjust the treatment regime accordingly. Recommendations for relieving symptoms such as joint stiffness and pain include the use of NSAIDs and corticosteroids, but these do not moderate disease progression. Over the last 20 years, the effectiveness of disease-modifying anti-rheumatic drugs (DMARDs) has earned much awareness, as these can efficiently mitigate disease activity and considerably decrease or delay joint deformity[8]. Despite the existence of an increasing number of drugs and novel treatment regimes, complete long-term disease remission has not been achieved yet[8]. As for implants, although total joint replacement has been a successful landmark in the orthopedic history of the 20th century, a report by Davidson et al.[13] states that the total number of revisions performed due to wear of the acetabular component of the implant reaches 10,000 per year. This high number of revisions indicates the severity of the problem at hand and proves the need for a proper understanding of the mechanisms by which wear occurs[9].

Tribology is defined as “the science and technology of interacting surfaces in relative motion and of related subjects and practices”[9]. It includes phenomena such as friction, wear, and lubrication, and it is described at length in Chapter 2 together with the tool we used to

measure tribological properties at the nanoscale, called nanotribology. The relative motion of interacting surfaces produces friction, which consequently may result in wear, a progressive loss of material resulting from solid surfaces in contact, whereas lubrication acts as a preventive measure to restrict consequences. Along with cartilage properties (such as its composition and structure), the tribological properties of SF are central to unravel the mystery of the remarkable lubrication in naturally occurring joints. More specifically, being able to quantify surface and interfacial forces, especially the friction and lubrication, are essential for restoring the native lubricating function. In diseases, both the chemical and the mechanical properties of joints are usually altered and understanding the molecular mechanisms by which healthy joints work may help us mitigating or restoring those properties. SF consists of numerous components that were stated to contribute either individually or synergistically to the lubrication of cartilage surfaces[14,15]. Most of the current research seeking to untangle the lubricating properties of SF focuses on the roles of its high molecular weight (hence high viscosity) components, such as hyaluronic acid and lubricin, but it often overlooks the smaller globular protein albumin. However, ironically 90% of the protein contents of SF consists of serum albumin (SA).[15]

In a recent study conducted by Sierra G. Cook, the role of the main components of SF (individually and/or in combination) was investigated and systematically compared with the lubrication profile of "full" native SF [2]. Her results show that (i) SF exhibits thickening as soon as it is sheared, (ii) aggregates are then formed in the SF film, and (iii) among all SF components tested, SA is a key contributor to the formation of these (shear-induced) aggregates, which seem to have a protective function of surfaces, as no wear was observed. While there exist studies where these 'protecting' protein gels otherwise known as aggregates/agglomerates have been observed, this research paper was the first to link the potential role of globular proteins aggregation in SF with surface protection in natural joints. SA was previously identified for its protective role in artificial joints, preventing wear of implants surface by providing aggregates 'ball-bearing' lubrication (keeping surfaces separated), and reducing friction[16,17]. These findings motivated the research at the heart of this thesis, as we wanted to correlate the material properties (composition, structure, mechanics) of SA aggregates with their tribological function. To do so, we used a tool called the Surface Forces Apparatus (SFA), which allowed us to monitor aggregates characteristics while

measuring friction and lubrication of thin films under shear. This technique is described at length in Chapter 2.

1.2 Synovial Joint

1.2.1 Functions

At four weeks of age of a human embryo is when the fore and hind limb buds appear as outgrowths of primitive mesenchyme [18]. A joint or articulation is formed where two or more bones of the body meet. A synovial joint is the most common type of joint found in mammals (Figure 1.1). A key characteristic of these joints is that they articulate to allow free movement. They are a crucial part of mammalian life span as they permit movement, locomotion, and fundamental functions of the skeleton. The presence of a joint cavity distinguishes the synovial joint from other fibrous or cartilaginous joints. The articulating surfaces of the bones are made of articular cartilage (see section 1.2.2) and able to shear past each other in this fluid-filled

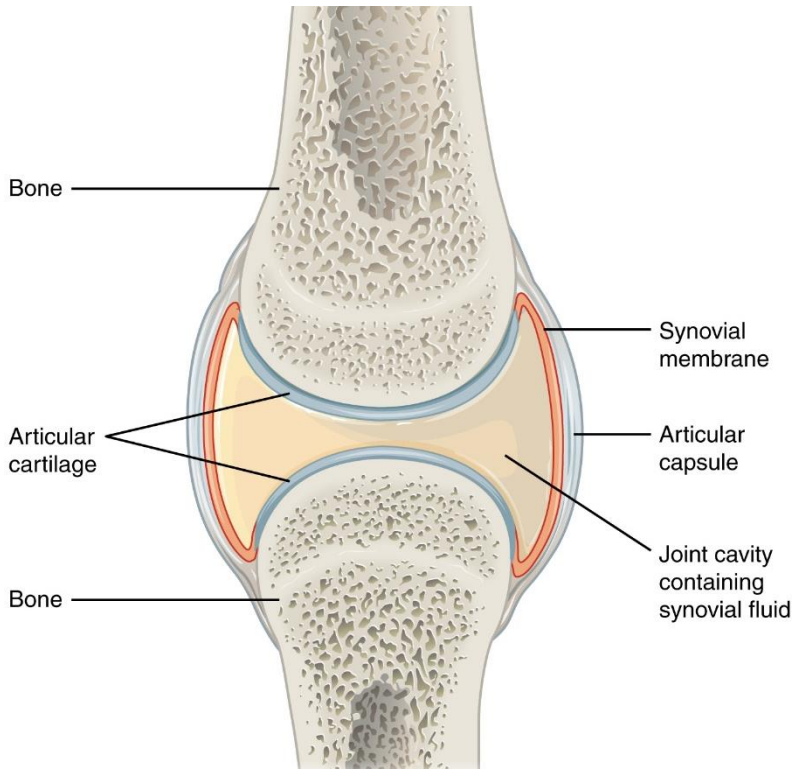

Figure 1.1 Synovial Joint diagram

(*Anatomy & Physiology, ConnexionsWebsite.http://cnx.org/content/col11496/1.6/,Jun19, 2013.)*

space. Another characteristic of synovial joints is that, since the surfaces are not directly in "contact", they can move smoothly against each other, enabling sustainable joint mobility.

1.2.2 Components

1.2.2.1 Articular cartilage

As seen in Figure 1.1, in a synovial joint, the entire articulating surface of each opposing bone is covered by a thin layer of hyaline cartilage. The hyaline cartilage is found in all articular joints and is a heterogeneous, aneural, and avascular tissue. It is highly hydrated (85% water by weight) and exhibits anisotropic mechanical properties[19]. Figure 1.2 (and insets) shows that, although non-collagenous proteins, glycoproteins, lipids, and other collagens are present in small amounts[19,20], collagen II and proteoglycans are the two most prominent constituents of articular cartilage. The categorization of the cartilage is as follows with correspondence to depth: superficial, transitional, and radial zones. The chemical composition and orientation of the collagen II vary with depth into the three zones.

The orientation of the bundles of collagen fibers in the deep/radial zone is radially outward from the surfaces of the subchondral bone[21]. The alignment provides resistance to compressive forces. The transitional/middle zone orientation is less organized but does follow a general diagonal pattern. This zone provides the anatomical and functional bridge between the other zones. The superficial/surface zone is the main region of the cartilage that is of greatest significance to the lubrication, as it acts as a sliding surface during motion. In the superficial zone, the orientation of the collagen fibrils is parallel to the surface tissue forming a dense mesh structure. Such orientation provides toughness enhancement as well as resistance to shear and tensile forces[21–23]. It also enables easy sliding of bones at the joint without rubbing against each other. The viscoelastic properties of the SF are attributed to a Hyaluronic acid (HA), a non-Newtonian shear-thinning fluid. It functions as an elastic shock absorber under impact and facilitates viscous lubrication under load. Proteoglycans are found in the lowest concentration, while water contents are the highest. Another abundant component in the superficial zone is the lubricating glycoprotein lubricin, which presence confirms the implication of proteins in cartilage lubrication. A link between the critical condition of lubricin and poor joint lubrication has also been widely reported [24–27]. Among proteins, the structural

protein fibronectin is also found in the superficial zone in the form of laterally oriented fibers but is not found in deeper zones of cartilage[28].

Remarkably low friction coefficients and efficient shock absorption are the principal functions of articular cartilage during movement. This mechanical response of the cartilage is attributed to the exclusive blend of collagen and proteoglycans. The proteoglycan present within the cartilage has negatively charged sites that are brought together when subjected to compression. This leads to an increase in mutual repulsive force which, in turn, increases compressive stiffness of the tissue [20–22]. The movement of interstitial fluid through the tissue also has intense effects on the system. The mechanics of the cartilage can be described as a biphasic material consisting of the solid-like collagen-proteoglycan network and fluid phase which flows through the network[2,20–22,24]. The bones of the articular cartilage are not connected, instead they act like Teflon coating over the bone surface allowing the articulating movement of the bones to glide past each other without causing any damage to the underlying bone tissue.

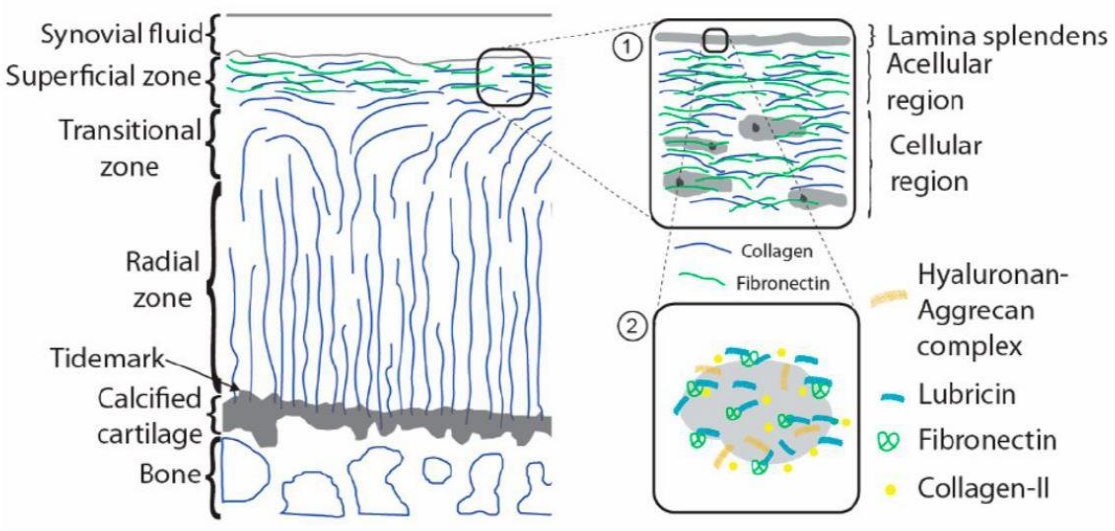

Figure 1.2 Structure and composition of articular cartilage[92]

1.2.2.2 Synovial Membrane

Articulating surfaces of conjoining bones connect with diarthrodial joints through collagenous connective tissue. This tissue is supported by ligaments, appends connections of the bones, and enables varying degrees of motion. On the inside of this collagenous connective

tissue facing the free joint space is the synovial membrane or more commonly called the synovium, which majorly contributes to the production of SF. It is composed of a thin layer of lining cells, consisting of both adipose and connective tissue. A rich vascular network supports the connective tissue. A compact interlacing layer of one to three cells in depth (thickness of 20 to 40 μm) comprises this lining of synovial cells.

1.2.2.3 Articular Capsule

The articular capsule, also known as the joint capsule, is key for the proper function of a synovial joint, as it enables the synovial fluid to stay trapped in the junction. It provides yielding stability by restraining joint movements, and dynamic stability via its interception nerve endings. A synovial joint capsule is made up of dense fibrous connective tissue lined with synovium [29]. The capsule enables nerves and blood vessels to pass through it, and the synovium protrudes to form pouches through the gaps. The stress endured in various regions determines the thickness as well as the fibre orientation of the capsule. Accessory ligaments support the joint capsule both inside and outside of the capsule, which restricts motion. A study conducted by Hoffmann and Grigg, 1989 [30] showcased the protection of the capsule from loading by accessory ligaments in the cat knee, while 4% of the load is being taken by the posterior joint capsule in full extension. In our knee joint, the anterior part is made up of the quadriceps and patellar tendons and the extensor tendon forms the dorsal part of the capsule.

1.2.2.4 Synovial fluid

There exist two types of fluids found abundantly in a human body, which are classified as extracellular (ECF) and intracellular fluids (ICF). ECF is present outside the cell and includes interstitial fluids (i.e. lymph and blood) whereas ICF is present within the cells. 62.5% of our body fluids are made up of ICF, whereas the rest 37.5% is made up ECFs[18]. Synovial fluid (SF) is an example of ECF which is reported to have egg-like ("synovial" partially derives from the ovum, latin for egg) consistency and to be thick and string-like. SF is found in the inner surface of the articular capsule and is produced by the synovial membrane (described previously).

The prime function of the joint is wearless low friction motion, and hence SF serves as a lubricant. SF must provide a nearly frictionless film on which the base of the joint can slide without binding under varying conditions of speed, motion (distance sheared), and weight-bearing. These requirements are fulfilled by normal/healthy SF in part due to its highly viscous nature [31].

SF also acts as an essential nourishment medium to the articular cartilage, which does not contain blood vessels. The molecular exchange is, therefore, slower than in the diffusion process involving intrinsic blood vessel [32]. The amount of SF present in a human knee joint has been reported to vary from 0.5 ml to 2 ml [33]. While the multiple functions of SF are well-understood thanks to intensive research and numerous studies published in recent years, how it functions as such an efficient lubricant is still unclear[34]. Arbitrarily the appearance of the fluid through naked eye may differ from joint to joint in the same species and with diverse species. The volume of fluid that could be extracted from humans is negligible for most chemical and physical observations, and hence resources from larger domestic animals are widely used.

There exists a consensus that SF is composed of hyaluronic acid (HA), lubricin (LUB) also referred to as the superficial zone protein, serum albumin (SA) and surface-active phospholipids (PL) [29]. Several studies have investigated the individual and/or synergistic roles of HA, LUB, and PL in lubrication and have been reported that they all contribute to the exceptional lubricating properties of SF[1,35,36]. However, the role of SA has been elusive and its contribution to articular lubrication remains scarce, which is why we are focusing on SA in this thesis, more specifically on its ability to mimic (qualitatively and quantitatively) the lubricating behaviour of SF under shear. For clarity, HA, LUB, and PL are described below, while a special section (Section 1.3) is dedicated to SA.

Hyaluronic Acid

Hyaluronic acid (HA) or otherwise known as hyaluronan was first found in 1934 by Karl Meyer and his colleague John palmer. They isolated a previously unknown chemical substance from the vitreous body of cow's eye [37]. Following which in 1942, Endre Balazs, filed a patent to use HA as a supplement for egg in bakery products due to its egg-like consistency [38]. After which, HA was later patented for its medical use in the 1950s [39]. In recent

decades, HA has been widely associated with an array of beauty procedures. As for clinical procedures, HA injections have been used on OA patients in a procedure called viscosupplementation that restores the viscosity of the synovial fluid which gets depleted in disease [2]. Additionally, SF is a non-Newtonian fluid exhibiting shear thinning, which is a phenomenon characteristic of some non-Newtonian fluids in which the fluid viscosity decreases with increasing shear rates [40]. At low speeds, SF forms long-chain molecules providing high viscosity to permit the flow of fluid yet keeping enough separation distance between sheared surfaces, whereas, at high speeds, the viscosity decreases but maintains efficient lubrication [41,42].

HA is a high molecular weight (6-7 MDa) non-sulfated glycosaminoglycan and is also one of the most abundantly found components in SF [1,35]. The structure of the disaccharide is energetically very stable. HA is unique in size and is synthesized at the plasma membrane rather than in the Golgi where sulfated glycosaminoglycans are added to protein cores[43–45]. There have been various studies that showcase the solutions of hyaluronan demonstrate very unusual rheological properties. The polymer chain in a solution of hyaluronan takes the structure of an expanded random coil. The unusual rheological properties of HA are attributed to the entanglement of these chains with each other at a very low concentration. Although HA was one of the first molecule of SF to have been identified as a lubricant[46], experiments performed with HA as early as 1968 demonstrated that degradation of HA with enzymes decreased the viscosity of SF but did not disrupt the lubricating ability of SF. Despite the development of HA-based therapeutics for OA patients, the beneficial effects were not uniformly observed amongst arthritic patient[15,47]. HA was reported to show no effect on lubricating behaviour and insignificant load-bearing abilities[48]. Due to this ambiguity and variable conclusions, the American College of Rheumatology and Osteoarthritis Research Society has remained neutral on the necessity of HA-based treatments [47].

Lubricin

After the role of HA being elusive and controversial in lubrication, other components of SF were investigated. Linn et al proposed that the primary lubricating component of SF was instead a mucin [49]. This theory was then supported by the documentation of proteoglycan 4 (PRG4), which was later concluded to be the lubricating mucin lubricin[24,50,51]. Lubricin (LUB)

comprises distinct lubricating and binding domains: the central glycosylated region is highly hydrated, negatively charged, and lubricates efficiently, while the end domains are non-glycosylated, positively charged, and enable surface attachment and self-aggregation.

LUB is a high molecular weight glycoprotein possessing a bottle brush-like configuration with a concentration of 0.2 mg/ml in SF [52]. The low coefficient of friction at the cartilage surface is achieved through the retention of water molecules at the cartilage surface via the large highly hydrophilic mucin region [48]. It was reported to significantly reduce friction between model surfaces and cartilage surfaces in-vitro, and also to mitigate cartilage damage [25,53] in-vivo[24,54] in animal studies.

The lubricating, highly hydrated central domain of LUB, paired with its ability to anchor to the cartilage surface results in the formation of a robust lubricating boundary layer on cartilage[55–57] There have been several research papers that showcase synergistic interaction between HA and LUB and their role in enhancing lubrication on both model surfaces and cartilages [58–61]. Based on reports of the effectiveness of visco-supplementary injections, LUB has potential for the development of OA therapies. However, despite these recent findings, the production of substantial volumes of LUB continues to be a critical challenge and hampers research into LUB tribosupplementation. Hence research is being conducted in the advancement of lubricin-mimetic molecules [62–64].

Phospholipids

Surface-active phospholipids (PL) impart the thin hydrophobic outermost lining to the normal articular surface. The role of PL has been identified as a boundary lubricant and has been shown to reduce friction in few studies [65–69]. They are generally phosphatidylcholines comprising diacyl tails and a phosphocholine head group; they form the major component of the lipids present both in SF and at the surface of articular cartilage. [70] PL are also present in other tissues (such as lungs). The source of indigenous PL in the joint is certainly lamellar bodies produced by type B synoviocytes. Interactions between HA and PL have been shown to provide exceptional low-friction properties[65–70].

1.3 Serum albumin

1.3.1 Concentration and structure

Human serum albumin (SA) is the most abundant constituent of SF, and the main object of this thesis, which is why it deserves its section. SA is the most abundant protein found in the circulatory system. It is one of the smallest existing globular proteins, with a molecular mass of 65 kDa[71,72]. It is synthesized in the liver and exported as a non-glycosylated protein. It is known majorly for the transport of unesterified fatty acids, also capable of binding an extraordinarily diverse range of metabolites, drug and organic compounds [73].

Several years ago, the crystal structure of human SA was published, with a 2.8 Å resolution.[52] As seen in Figure 1.3, the molecule possesses a tertiary structure: it is heart-shaped and it consists of three repeating domains labelled I, II, III, each of which is divided into two subdomains. Around ~67% of the protein has a high α-helical content with no β-sheet [72] secondary structures. It consists of 585 amino acids and is comparatively rich in cysteine, which allows the formation of 17 internal stabilizing disulfide bridges[71].

While the concentration of SA in the blood is marked at around 40 mg ml^{-1} , it ranges from 7 to 18 mg ml^{-1}in SF [74]. The remarkable binding properties of SA has led to a great deal of research on the nature of the drug-binding sites. A consensus exists that there are five

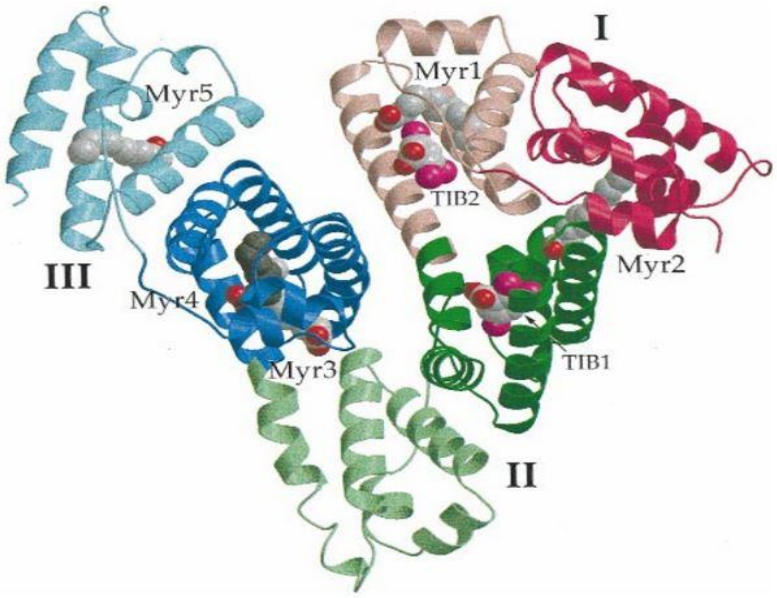

Figure 1.3 The heart-shaped albumin molecule structure[115]

principal sites for medium or long-chain fatty acids[75–77] in which three of them provide significantly stronger binding than the other two 'secondary' sites [78]. Nevertheless, an absolute unanimity has not been reached yet.

1.3.2 Aggregation of SA and its implications in SF lubrication

A recent study conducted by our group and collaborators at Cornell University demonstrates that, when confined and sheared between model mica surfaces, SF films thicken by more than 300% and readily form large and dense aggregates [2]. These aggregates were reported to act as transient protective ball bearings (made of globular protein and γ-globulin) reducing friction and keeping shearing surfaces far apart to prevent damage. The study also conducted shear experiments on various components of SF to try understanding which of its components best mimicked SF behavior under shear, in particular aggregates' formation. The authors concluded that albumin was a key contributor to both formations of aggregates and film thickening. Aggregation phenomena have been studied extensively on multi-components fluids sheared across a large range of surfaces. [17,34,41,79–82]. For example, a study conducted by Yang et al. reported that SA plays a vital role in boundary lubrication by acting as an interfacial layer between shearing surfaces [72], which is in agreement with the above-mentioned conclusion drawn by Sierra Cook et al. Another study conducted by Oates et al. concluded that protein aggregation of SF is responsible for observed rheopexy, namely another property of non-Newtonian fluids synonymous of time-dependent increase in viscosity (the longer the film is sheared, the higher its viscosity)[34]. The authors also speculated that the reported rheopexy may be responsible for the remarkable lubricating properties of SF, although this claim needs further investigation. In various SF studies, aggregates are sometimes referred to as the 'gel phase' or 'gel film', and are often associated with their ability to minimize wear of surfaces[79,82].

1.4 Presence of SA aggregates on surfaces of implants

One of the reasons for the appearance of wear, usually leading to failure of artificial implants, is the breakdown of the lubricating film that separates the surfaces. The formation of nanometer- to micron-sized wear debris, which are biologically active and provoke an adverse cellular response, is observed on failed implants [10,83,84]. The development of a shear-induced thick 'protein aggregate gel' has also been reported in in-vitro tests of artificial hip joints (Figure 1.4) when sheared across fetal bovine serum albumin (BSA)[74,85–87] and is believed to occur at the surface of an artificial implant in-vivo as shown in Figure 1.5. Aggregates present on implants consist of many "particles" and constituents. Along with denatured lubricating proteins, aggregates from implants also comprise metal and plastic debris from wear and surface damage. The amount of BSA adsorbed onto the sheared surface influences both the presence and the adherence of wear debris at the surface. This conclusion was drawn by Suwandi et al. while investigating prosthetics materials made of ultra-high-molecular-weight polyethene (UHMWPE) shearing against 316L stainless steel[88]. Furthermore, SA adsorption behaviour also controlled friction and wear behaviour[16]. However, the rate of BSA adsorption at the surface varies with the type of material and its hydrophobicity. It was reported that SA's adsorption was higher on hydrophobic materials than on a hydrophilic ones [16,72,88,89]. The attraction of SA towards the hydrophobic surfaces

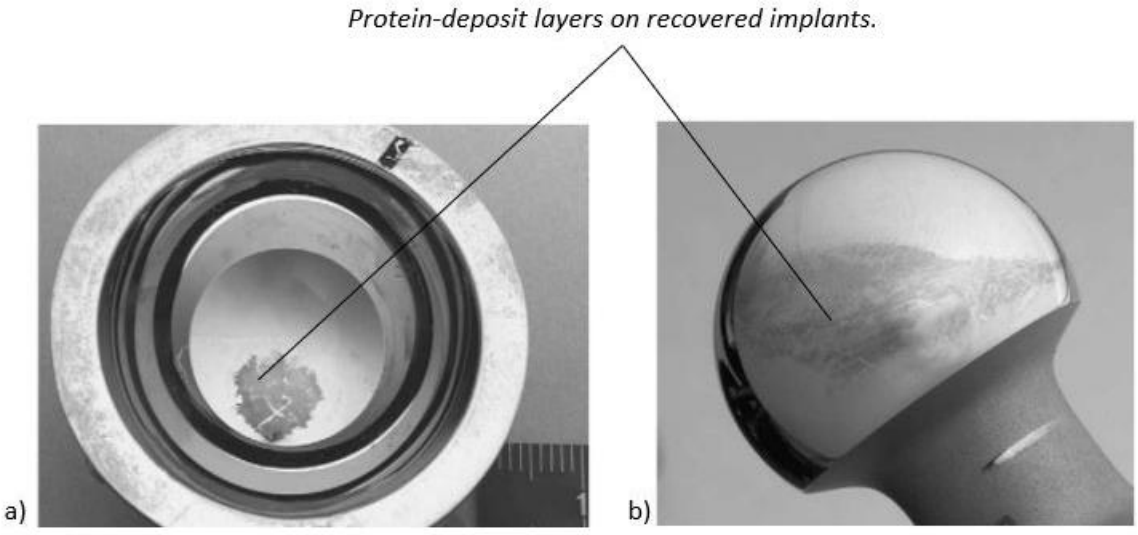

Figure 1.4 Photograph of femoral head surface [81]

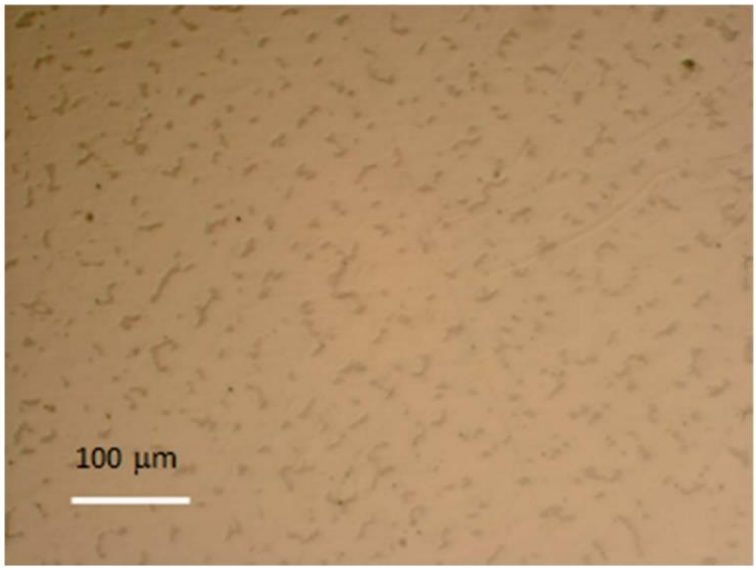

Figure 1.5 Cup (a) and head (b) of an explanted McKee–Farrar prosthesis made of cast cobalt–chromium alloy[116]

(and likely its ability to keep its molecular conformation) seems to determine the extent of wear produced during shear [90]. Interestingly, a study conducted by H. Mishina et al. using human SA shows that human SA continued its role of boundary lubricant even upon denaturation[16]. However, authors from the studies did not notice any type of denaturation of SA on opposing surfaces [16,72,88,89].

1.5 Fibronectin and its indirect role in joint lubrication

Fibronectin (FN) is a macromolecular glycoprotein (molecular weight: 0.22 MDa) abundantly found in the extracellular matrix of connective tissues as well as in body fluids. In synovial joints, FN is found in the superficial zone of cartilage. It is known to mediate the adhesion of SF constituents to the joints[91,92]. Its responsibility in the prevention of SF being expelled from the joints contributes indirectly to the lubrication process. Its specific role in being able to anchor and interact synergistically with SF proteins is still unclear. A recent study conducted by Andresen et al. suggests that FN does act as an efficient tethering component of boundary lubricant molecules. The study also suggests that FN strongly binds to boundary lubricants like LUB and HA and that LUB and FN synergistically ensure lower friction and provide efficient protection against surface damage[92].

The study does state the synergistic effects of SA and FN, but an in-depth analysis with varied concentrations of FN and SA has not been exhaustively studied. A foremost part of this thesis probes into the aggregation process of SA using various adsorption protocols and concentrations of FN. We are also asking whether SA aggregation in presence of FN (used as a coating of the mica substrates) promotes better lubrication and wear protection than SA aggregation occurring without FN (when shear is performed across bare mica surfaces). This is interesting since it is known that BSA is able to (at least partially) unfold FN, in particular, FN immunoglobulin-like type III modules, due to its high affinity towards hydrophobic sites. Hence, we tested protocols with and without SA passivation (using a low concentration of SA to block non-specific interactions at the FN surface) before injection and shear across bulk SA film. Figure 1.6 summarizes the proposed molecular schematics based on the study performed by Sierra Cook [2] for heart-shaped free-floating SA alone without any anchoring factor-like FN (Fig. 1.6.a), FN alone mesh at the mica surface (Fig. 1.6.b), and SA in the presence of FN involving the unfolding of FN and the anchoring of SA molecules to FN (Fig1.6.c).

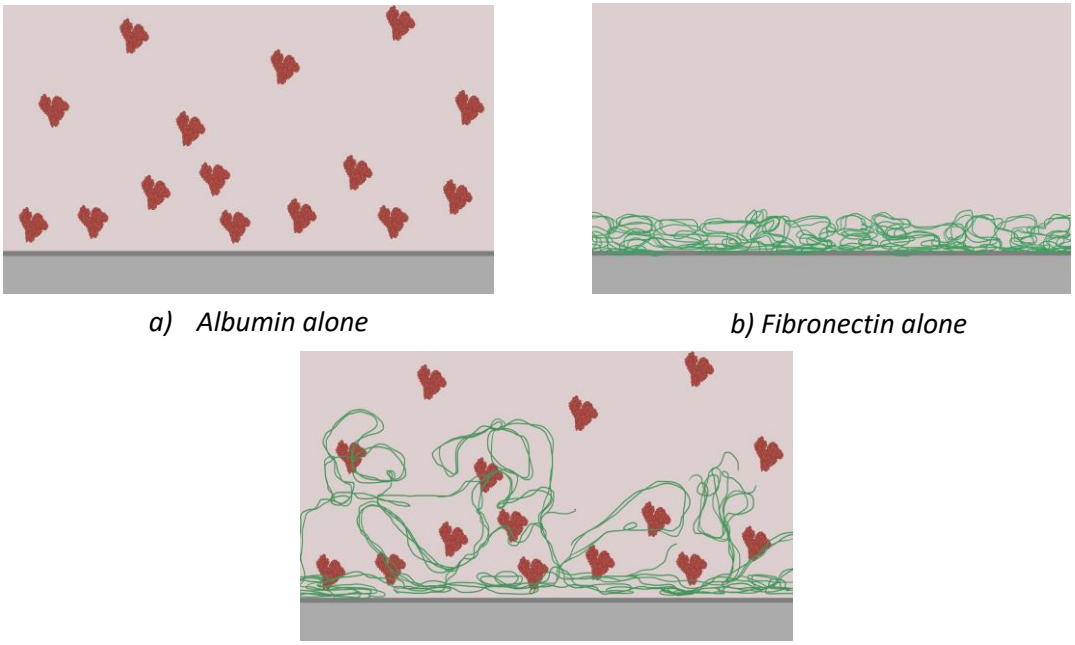

Figure 1.6 Schematics showing a) Albumin alone b) Fibronectin alone c) Fibronectin + Albumin

1.6 Thesis goal line

In summary, while most previous studies of SF lubrication focused on the tribological roles of individual SF constituents such as HA or LUB, a recent study from our group indicates that SA comes closest in mimicking the bulk behaviour of SF. In particular, sheared SA films thicken and form numerous and sustainable aggregates, as do SF films under the same conditions. These aggregates are believed to be at the origin of efficient lubrication, acting like ball bearings that keep the surface of the joints apart, minimizing friction and preventing surface damage.

Therefore, in this thesis, we are focusing on the investigation of (i) the dynamics of aggregates' formation and (ii) the detailed characterisation of the material properties of the resulting aggregates, which includes the measurements of:

i) Film thickness and presence of aggregates (if any)
ii) Average size and shape of aggregates
iii) Mobility and distribution of aggregates
iv) Longevity of aggregates
v) Stiffness of aggregates
vi) Composition of aggregates

while shearing and measuring friction forces across SA films, as permitted by the Surface Forces Apparatus (SFA), described in Chapter II.

Our study aims not only at providing experimental evidence of the complementary roles of both the lubricant (here the sheared globular protein SA) and the bearing surface (here the fibrillar protein FN) properties in lubrication but also at establishing a correlation between protein concentration, formation and stability of aggregates, low friction and wear protection. Although our findings will be based on experiments involving rigid, nonporous surfaces, which can hardly be generalized to compliant and porous cartilage surfaces, they will apply to other rigid tribiosystem such as artificial joints and will certainly advance our understanding of joint implants' lubrication in SF mediated by protein aggregation, with implications for the future design of artificial joints and therapeutic interventions.

.

1.7 References

1. Hui, A. Y., McCarty, W. J., Masuda, K., Firestein, G. S. & Sah, R. L. A Systems Biology Approach to Synovial Joint Lubrication in. *Wiley Interdiscip. Rev. Syst. Biol. Med.* **4**, 15–37 (2013).
2. Cook, S. G. Mechanism of synovial fluid of lubrication at the molecular and tissue scale. (2019).
3. Jahn, S. & Klein, J. Lubrication of articular cartilage. *Phys. Today* **71**, 48–54 (2018).
4. Abreu, E. Review of 'Basic Orthopaedic Biomechanics and Mechano-Biology' 3rd Edition, by Van C. Mow and Rik Huiskes. *Biomed. Eng. Online* **4**, 28 (2005).
5. Silva, M., Shepherd, E. F., Jackson, W. O., Dorey, F. J. & Schmalzried, T. P. Average patient walking activity approaches 2 million cycles per year: Pedometers under-record walking activity. *J. Arthroplasty* **17**, 693–697 (2002).
6. Glyn-Jones, S. *et al.* Osteoarthritis. *Lancet* **386**, 376–387 (2015).
7. Hunter, D. J., Neogi, T. & Hochberg, M. C. Quality of osteoarthritis management and the need for reform in the us. *Arthritis Care Res.* **63**, 31–38 (2011).
8. Guo, Q. *et al.* Rheumatoid arthritis: Pathological mechanisms and modern pharmacologic therapies. *Bone Research* vol. 6 (2018).
9. Menezes, P. L., Ingole, S. P., Nosonovsky, M., Kailas, S. V. & Lovell, M. R. Tribology for scientists and engineers: From basics to advanced concepts. *Tribol. Sci. Eng. From Basics to Adv. Concepts* **9781461419**, 1–948 (2013).
10. Wroblewski, B. M. & Siney, P. D. Charnley low-friction arthroplasty of the hip: Long-term results. in *Clinical Orthopaedics and Related Research* vol. 292 191–201 (1993).
11. Mora, J. C., Przkora, R. & Cruz-Almeida, Y. Knee osteoarthritis: Pathophysiology and current treatment modalities. *J. Pain Res.* **11**, 2189–2196 (2018).
12. Anandacoomarasamy, A. & March, L. Current evidence for osteoarthritis treatments. *Therapeutic Advances in Musculoskeletal Disease* vol. 2 17–28 (2010).
13. Parkes, M., Myant, C., Cann, P. M. & Wong, J. S. S. Synovial Fluid Lubrication: The Effect of Protein Interactions on Adsorbed and Lubricating Films. *Biotribology* **1**–**2**, 51–60 (2015).

14. Kosinska, M. K. *et al.* Articular joint lubricants during osteoarthritis and rheumatoid arthritis display altered levels and molecular species. *PLoS One* **10**, e0125192 (2015).
15. Cook, S. G. *et al.* Dynamics of Synovial Fluid Aggregation under Shear. *Langmuir* **35**, 15887–15896 (2019).
16. Mishina, H. & Kojima, M. Changes in human serum albumin on arthroplasty frictional surfaces. *Wear* **265**, 655–663 (2008).
17. Serro, A. P. *et al.* Adsorption of albumin on prosthetic materials: Implication for tribological behavior. *J. Biomed. Mater. Res. Part A* **78A**, 581–589 (2006).
18. Piper R, M. stafford. The structure and function of synovial fluid with particular reference to mechanism of their lubrication. *J. Chem. Inf. Model.* **53**, 1689–1699 (1972).
19. Cohen, N. P., Foster, R. J. & Mow, V. C. Composition and dynamics of articular cartilage: Structure, function, and maintaining healthy state. *Journal of Orthopaedic and Sports Physical Therapy* vol. 28 203–215 (1998).
20. Mansour, J. Biomechanics of Cartilage. in *Kinesiology: The Mechanics and Pathomechanics of Human Movement* (ed. Otis, C.) 68–77 (2013).
21. Sophia Fox, A. J., Bedi, A. & Rodeo, S. A. The basic science of articular cartilage: structure, composition, and function. *Sports Health* **1**, 461–8 (2009).
22. Camarero-Espinosa, S., Weder, C., Rothen-Rutishauser, B. & Foster, E. J. Articular cartilage: from formation to tissue engineering. *Biomater. Sci* **4**, (2016).
23. Kaab, M. J., Gwynn, I. A. & Notzli, H. Collagen fibre arrangement in the tibial plateau articular cartilage of man and other mammalian species. *J. Anat* **193**, 23–34 (1998).
24. Gleghorn, J. P. & Bonassar, L. J. Lubrication mode analysis of articular cartilage using Stribeck surfaces. *J. Biomech.* **41**, 1910–8 (2008).
25. Zappone, B., Ruths, M., Greene, G. W., Jay, G. D. & Israelachvili, J. N. Adsorption, lubrication, and wear of lubricin on model surfaces: polymer brush-like behavior of a glycoprotein. *Biophys. J.* **92**, 1693–708 (2007).
26. Jay, G. D., Torres, J. R., Warman, M. L., Laderer, M. C. & Breuer, K. S. The role of lubricin in the mechanical behavior of synovial fluid. *Proc. Natl. Acad. Sci. U. S. A.* **104**, 6194–6199 (2007).

27. Jay, G. D. *et al.* Prevention of cartilage degeneration and restoration of chondroprotection by lubricin tribosupplementation in the rat following anterior cruciate ligament transection. *Arthritis Rheum.* **62**, 2382–2391 (2010).
28. Andresen Eguiluz, R. C. *et al.* Synergistic Interactions of a Synthetic Lubricin-Mimetic with Fibronectin for Enhanced Wear Protection. *Front. Bioeng. Biotechnol.* **5**, 1–13 (2017).
29. Ralphs, J. R. & Benjamin, M. The joint capsule: structure, composition, ageing and disease. *J. Anat.* **184 (Pt 3**, 503–9 (1994).
30. Grigg, P. & Hoffman, A. H. Calibrating joint capsule mechanoreceptors as in vivo soft tissue load cells. *J. Biomech.* **22**, 781–785 (1989).
31. Schmid, F. R. & Ogata, R. I. Composition and Examination of synovial fluids. *J. Prosthet. Dent.* **8**, 449–457 (1967).
32. Lu, Y., Levick, J. R. & Wang, W. The mechanism of synovial fluid retention in pressurized joint cavities. *Microcirculation* **12**, 581–595 (2005).
33. Yehia, S. R. & Duncan, H. Synovial fluid analysis. *CLIN.ORTHOP.* **No. 107**, 11–24 (1975).
34. Oates, K. M. . N., Krause, W. E., Jones, R. L. & Colby, R. H. Rheopexy of synovial fluid and protein aggregation. *J. R. Soc. Interface* **3**, 167–74 (2006).
35. Bennike, T. *et al.* A normative study of the synovial fluid proteome from healthy porcine knee joints. *J. Proteome Res.* **13**, 4377–4387 (2014).
36. Swann, D. a *et al.* Role of hyaluronic acid in joint lubrication. *Ann. Rheum. Dis.* **33**, 318–26 (1974).
37. Tamer, T. M. Hyaluronan and synovial joint: Function, distribution and healing. *Interdiscip. Toxicol.* **6**, 111–125 (2013).
38. Necas, J., Bartosikova, L., Brauner, P. & Kolar, J. *Hyaluronic acid (hyaluronan): a review*. *Veterinarni Medicina* vol. 53 (2008).
39. Nečas, D., Vrbka, M., Urban, F., Křupka, I. & Hartl, M. The effect of lubricant constituents on lubrication mechanisms in hip joint replacements. *J. Mech. Behav. Biomed. Mater.* **55**, 295–307 (2016).
40. Itano, N. & Kimata, K. Mammalian hyaluronan synthases. *IUBMB Life* vol. 54 195–199 (2002).

41. Weigel, P. H., Hascall, V. C., Tammi, M. & Weigel PH. Hyaluronan synthases. *Journal of Biological Chemistry* vol. 272 13997–14000 http://www.xenbase.org/literature/article.do?method=display&articleId=16467 (1997).
42. Kogan, G., Šoltés, L., Stern, R. & Gemeiner, P. Hyaluronic acid: A natural biopolymer with a broad range of biomedical and industrial applications. *Biotechnology Letters* vol. 29 17–25 (2007).
43. Ogston, A. G. & Stanier, J. E. The Physiological Function of Hyaluronic Acid in Synovial Fluid; Viscous, Elastic and Lubricant Properties. *J. Physiol.* **4**, 244–252 (1952).
44. Bowman, S., Awad, M. E., Hamrick, M. W., Hunter, M. & Fulzele, S. Recent advances in hyaluronic acid based therapy for osteoarthritis. *Clin. Transl. Med.* **7**, 6 (2018).
45. Daniel, M. Boundary cartilage lubrication: Review of current concepts. *Wiener Medizinische Wochenschrift* **164**, 88–94 (2014).
46. Linn, F. C. Lubrication of Animal Joints II: The Mechanism. *J. Biomech.* **1**, 193–205 (1968).
47. Schmid, T. *et al.* Superficial Zone Protein (SZP) is an Abundant Glycoprotein in Human Synovial Fluid and Serum. *Trans. Orthopoedic Res. Soc.* (2001).
48. Swann, D. a, Slayter, H. S. & Silver, F. H. The molecular structure of lubricating glycoprotein-I, the boundary lubricant for articular cartilage. *J. Biol. Chem.* **256**, 5921–5 (1981).
49. He, X. M. & Carter, D. C. Atomic structure and chemistry of human serum albumin. *Nature* **358**, 209–215 (1992).
50. Coles, J. M., Chang, D. P. & Zauscher, S. Molecular mechanisms of aqueous boundary lubrication by mucinous glycoproteins. *Curr. Opin. Colloid Interface Sci.* **15**, 406–416 (2010).
51. Schmidt, T. A., Gastelum, N. S., Nguyen, Q. T., Schumacher, B. L. & Sah, R. L. Boundary lubrication of articular cartilage: Role of synovial fluid constituents. *Arthritis Rheum.* **56**, 882–891 (2007).
52. Bonnevie, E. D., Galesso, D., Secchieri, C., Cohen, I. & Bonassar, L. J. Elastoviscous

Transitions of Articular Cartilage Reveal a Mechanism of Synergy between Lubricin and Hyaluronic Acid. *PLoS One* **10**, (2015).

53. Jones, A. R. C. *et al.* Binding and localization of recombinant lubricin to articular cartilage surfaces. *J. Orthop. Res.* **25**, 283–292 (2007).
54. Flowers, S. A. *et al.* Lubricin binds cartilage proteins, cartilage oligomeric matrix protein, fibronectin and collagen II at the cartilage surface. *Sci. Rep.* **7**, (2017).
55. Das, S. *et al.* Synergistic Interactions between Grafted Hyaluronic Acid and Lubricin Provide Enhanced Wear Protection and Lubrication. *Biomacromolecules* **14**, 1669–1677 (2013).
56. Ludwig, T. E., Hunter, M. M. & Schmidt, T. A. Cartilage boundary lubrication synergism is mediated by hyaluronan concentration and PRG4 concentration and structure. *BMC Musculoskelet. Disord.* **16**, (2015).
57. Ye, H. *et al.* Interactions between Lubricin and Hyaluronic Acid Synergistically Enhance Antiadhesive Properties. *ACS Appl. Mater. Interfaces* **11**, 18090–18102 (2019).
58. Greene, G. W. *et al.* Adaptive mechanically controlled lubrication mechanism found in articular joints. *Proc. Natl. Acad. Sci. U. S. A.* **108**, 5255–9 (2011).
59. Samaroo, K. J., Tan, M., Putnam, D. & Bonassar, L. J. Binding and lubrication of biomimetic boundary lubricants on articular cartilage. *J. Orthop. Res.* **35**, 548–557 (2017).
60. Faivre, J. *et al.* Intermolecular interactions between bottlebrush polymers boost the protection of surfaces against frictional wear. *Chem. Mater.* **30**, 4140–4149 (2018).
61. Banquy, X., Burdyńska, J., Lee, D. W., Matyjaszewski, K. & Israelachvili, J. Bioinspired bottle-brush polymer exhibits low friction and Amontons-like behavior. *J. Am. Chem. Soc.* **136**, 6199–202 (2014).
62. Hills, B. A. & Crawford, R. W. Normal and prosthetic synovial joints are lubricated by surface-active phospholipid: A hypothesis. *Journal of Arthroplasty* vol. 18 499–505 (2003).
63. Trunfio-Sfarghiu, A. M., Berthier, Y., Meurisse, M. H. & Rieu, J. P. Role of nanomechanical properties in the tribological performance of phospholipid biomimetic surfaces. *Langmuir* **24**, 8765–8771 (2008).

64. Murakami, T., Yarimitsu, S., Nakashima, K., Sawae, Y. & Sakai, N. Influence of synovia constituents on tribological behaviors of articular cartilage. *Friction* **1**, 150–162 (2013).
65. Briscoe, B. J. & Evans, D. C. B. The shear properties of Langmuir—Blodgett layers. *Proc. R. Soc. London. A. Math. Phys. Sci.* **380**, 389–407 (1982).
66. Briscoe, W. H. *et al.* Boundary lubrication under water. *Nature* **444**, 191–194 (2006).
67. Sarma, A. V., Powell, G. L. & LaBerge, M. Phospholipid composition of articular cartilage boundary lubricant. *J. Orthop. Res.* **19**, 671–676 (2001).
68. Sugio, S., Kashima, A., Mochizuki, S., Noda, M. & Kobayashi, K. Crystal structure of human serum albumin at 2.5 Å resolution. *Protein Eng.* **12**, 439–446 (1999).
69. Yang, C. Bin *et al.* Frictional characteristics of the tribological unfolding albumin for polyethylene and cartilage. *Chem. Phys. Lett.* **431**, 380–384 (2006).
70. Curry, S., Mandelkow, H., Brick, P. & Franks, N. *Crystal Structure of HSA. Nature Structural Biology* vol. 5 http://structbio.nature.com (1998).
71. Fan, J., Myant, C. W., Underwood, R., Cann, P. M. & Hart, A. Inlet protein aggregation: A new mechanism for lubricating film formation with model synovial fluids. in *Proceedings of the Institution of Mechanical Engineers, Part H: Journal of Engineering in Medicine* vol. 225 696–709 (2011).
72. Reed, R. G. Location of long chain fatty acid-binding sites of bovine serum albumin by affinity labeling. *J. Biol. Chem.* **261**, 15619–15624 (1986).
73. Sklar, L. A., Hudson, B. S. & Simoni, R. D. Conjugated Polyene Fatty Acids as Fluorescent Probes: Binding to Bovine Serum Albumin. *Biochemistry* **16**, 5100–5108 (1977).
74. Hamilton, J. A., Era, S., Bhamidipati, S. P. & Reed, R. G. Locations of the three primary binding sites for long-chain fatty acids on bovine serum albumin. *Proc. Natl. Acad. Sci. U. S. A.* **88**, 2051–2054 (1991).
75. Spector, A. A. Fatty acid binding to plasma albumin. *Journal of Lipid Research* vol. 16 165–179 (1975).
76. Myant, C., Underwood, R., Fan, J. & Cann, P. M. Lubrication of metal-on-metal hip joints: The effect of protein content and load on film formation and wear. *J. Mech. Behav. Biomed. Mater.* **6**, 30–40 (2012).

77. Myant, C. & Cann, P. On the matter of synovial fluid lubrication: Implications for Metal-on-Metal hip tribology. *J. Mech. Behav. Biomed. Mater.* **34**, 338–348 (2014).
78. Banquy, X., Lee, D. W., Das, S., Hogan, J. & Israelachvili, J. N. Shear-induced aggregation of mammalian synovial fluid components under boundary lubrication conditions. *Adv. Funct. Mater.* **24**, 3152–3161 (2014).
79. Fan, J., Myant, C., Underwood, R. & Cann, P. Synovial fluid lubrication of artificial joints: Protein film formation and composition. *Faraday Discuss.* **156**, 69–85 (2012).
80. Myant, C. W. & Cann, P. The effect of transient conditions on synovial fluid protein aggregation lubrication. *J. Mech. Behav. Biomed. Mater.* **34**, 349–357 (2014).
81. Hart, A. J. *et al.* The association between metal ions from hip resurfacing and reduced T-cell counts. *J. Bone Jt. Surg. - Ser. B* **88**, 449–454 (2006).
82. Revell, P. A., Al-Saffar, N. & Kobayashi, A. Biological reaction to debris in relation to joint prostheses. *Proc. Inst. Mech. Eng. Part H J. Eng. Med.* **211**, 187–197 (1997).
83. Stevenson, H. *et al.* The development of a small-scale wear test for CoCrMo specimens with human synovial fluid. *Biotribology* **14**, 1–10 (2018).
84. Mavraki, A. & Cann, P. M. Lubricating film thickness measurements with bovine serum. *Tribol. Int.* **44**, 550–556 (2011).
85. Myant, C. & Cann, P. In contact observation of model synovial fluid lubricating mechanisms. *Tribol. Int.* **63**, 97–104 (2013).
86. Suwandi, J. S., Toes, R. E. M., Nikolic, T. & Roep, B. O. Adsorption of albumin on prosthetic materials: Implication for tribological behavior. *Clin. Exp. Rheumatol.* **33**, 97–103 (2015).
87. Karimi, S., Nickchi, T. & Alfantazi, A. Effects of bovine serum albumin on the corrosion behaviour of AISI 316L, Co-28Cr-6Mo, and Ti-6Al-4V alloys in phosphate buffered saline solutions. *Corros. Sci.* **53**, 3262–3272 (2011).
88. Samak, M. S. Role of serum albumin aggregation in lubrication and wear protection of shearing surfaces. (2019).
89. Przybysz, M., Borysewicz, K., Szechiński, J. & Katnik-Prastowska, I. Synovial fibronectin fragmentation and domain expressions in relation to rheumatoid arthritis progression. *Rheumatology* **46**, 1071–1075 (2007).
90. Andresen Eguiluz, R. C. *et al.* Fibronectin mediates enhanced wear protection of

lubricin during shear. *Biomacromolecules* **16**, 2884–2894 (2015).

91. R. Crockett. Biochemical composition of the superficial layer of articular cartilage. **67**, 1180–1185 (2017).

92. Wimmer, M. A., Sprecher, C., Hauert, R., Täger, G. & Fischer, A. Tribochemical reaction on metal-on-metal hip joint bearings. *Wear* **255**, 1007–1014 (2003).

Chapter 2 – Theoretical and technical background

2.1 Tribology

The study of friction, lubrication and wear is called tribology. It is a highly interdisciplinary field including physics, chemistry, materials science, mathematics, biology and engineering[1]. It aims at understanding the atomic processes that occur at the interface of two materials when brought in contact and sheared past each other; it provides an insight into many technological problems. When two surfaces are in contact, the interfacial interactions involve both static and dynamic forces. At interfaces, frictional forces are distributed over the various interacting contact points rather than being concentrated on a single contacting point or over the entire volume. It is a force that is linearly proportional to the number of asperities interacting with each other over the contact[2]. Because realistic surfaces are often rough and exhibit heterogeneous chemical composition, friction is always present at interfaces. Friction is the result of the interaction between asperities present on the contact area of two sliding surfaces and friction coefficient, μ, is the ratio of the force of friction between the two sliding surfaces and the force pressing them together. Asperities are nothing but smaller contact areas occurring purely due to the roughness of the surface. Table 2.1 is a summary of various models and their relationship between frictional force, area, and applied load at the macroscopic level.

Model - Multi-Asperity	$\boldsymbol{F_{fr}}$ *vs.* Area	$\boldsymbol{F_{fr}}$ *vs.* Load
Amontons' Law	Independent of contact area.	$F_{fr} = \bar{\mu}L$
Bowden and tabor	$F_{fr} = \tau \sum A_{asp}$	$F_{fr} = \bar{\mu}L$
Model- Single-Asperity	F_{fr} *vs.* Area	F_{fr} *vs.* Load
Hertz model (Non-adhesive contact)	$F_{fr} = \tau * A_{asp}$	$F_{fr} \propto L^{2/3}$
Maugis-Dugdale model (Adhesive contact)	$F_{fr} = \tau * A_{asp}$	F_{fr} the sublinear function of L

Table 2.1 Shows different models explaining the relationship between frictional force, area, and applied load at the macroscopic level[3]

2.2 Nanotribology with the Surface Force Apparatus

The measurement of interaction forces between robust materials started way back in the 1920s when Tomlinson measured the adhesion between crossed filaments of various metals[3]. Over the years, various research groups around the Netherlands and Russia developed different techniques for measuring forces between surfaces of quartz or glass as a function of their separation[3,4,5]. Soon the original work was adapted by many other groups. One such striking work performed was at Cambridge (Cavendish Laboratory), which led to the development of the Surface Force Apparatus (SFA)[6]. The researchers behind this remarkable machine were Israelachvili, Winterton and Tabor. While this device was developed in the early 1970s, it was not until a decade later in the 1980s that nanotribology studies with the SFA became a very active field of research. Since then, this technique has experienced various modifications. The SFA Mark III (SurForce, Santa Barbara CA) is the specific type of SFA used to carry out all the experiments presented in this thesis.

2.2.1 The Surface Force Apparatus (SFA) technique

A typical SFA nanotribology experiment (Figure 2.1) is conducted using preliminary substrates made of atomically smooth (back-silvered) mica-surfaces. The preparation of these surfaces and their mounting/alignment in the SFA chamber are mentioned in detail below. In short, mica pieces are glued to cylindrically curved silica discs. The use of mica as a substrate for SFA experiments was implemented by Bailey and Courtney-Pratt[7]. The axes of these silica cylinders are placed perpendicular to each other (inset Figure 2.1) to ensure a perfectly circular contact area between contacting surfaces. Further, it enables the examination of numerous spots on the same pair of surfaces. This examination can be achieved by displacing either one or both cylinders laterally. This trait is helpful in case of (insoluble) aggregate formation, surface contamination, or mica damage at the interface. Finally, the results of measurements are convenient to compare with the theoretical description, initially intended for flat surfaces[4]. One of the critical assets of this technique is its ability to simultaneously visualise the contact area (through multiple-beam interferometry) and measure the distance between the surfaces in contact. The SFA is one of the very few techniques that allow us to perform in-situ real-

time assessment of the size and geometry of contacting junctions with sub nanometric resolution and accurate force measurements under confinement and shear.

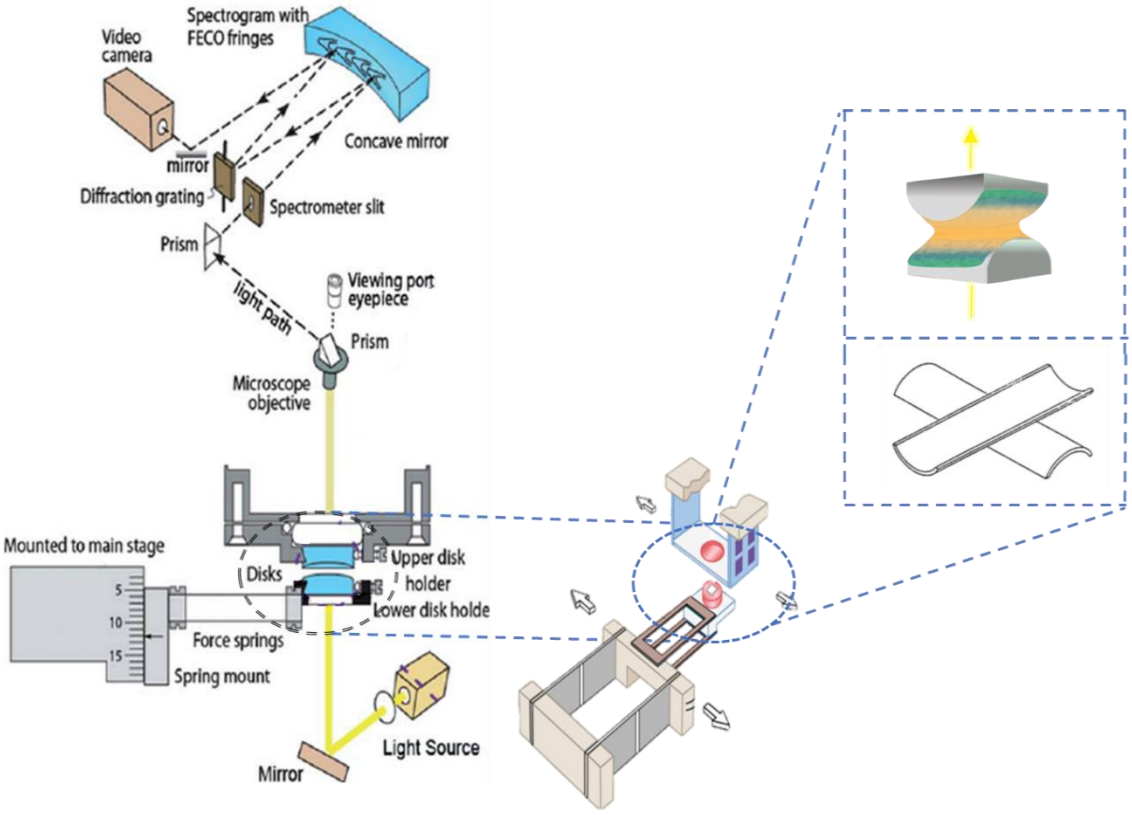

Figure 2.1 Optical and mechanical setup of SFA highlighting the cross-axial configuration of silica discs. [15]

2.2.2 Performing experiments with the SFA

Preparation of preliminary mica surfaces: cleaving, cutting, silvering, gluing, aligning

The entire preparation of the surfaces is done in a laminar flow hood. Clean tweezers and mini forceps are cleaned using ethanol and are placed in the hood. At first, a thick sheet of mica is taken, the edges are trimmed, and the excessive flakes from the sides are removed. The thick sheet is then cleaved into a "semi-thick" sheet. During this process, the sheets are slowly peeled away to expose two smooth surfaces. The surfaces need to be step-free, and for that, the bifurcation lines are required to move smoothly without any cracking or jerking while peeling. Tip of a sharp needle is inserted into the edge of the thick sheets to initiate cleaving.

These sheets are then inspected for the presence of steps (if any). One of the two initially semi-thick stepless cleaved sheets is selected as a 'backing sheet' and is stored in a petri-dish. This so-called backing sheet is used as temporary substrate for the final thin mica pieces later used as surfaces for our experiments. These final mica pieces are obtained via further (repeating) cleaving of much thinner and smaller sheets. The cleaving is usually done in the direction parallel to the step. If a sheet is of adequate thickness (2-3 um thick) bright interference colours are reflected by the surface, these colours change at the cleavage steps but remain uniform throughout stepless regions. Before the placement of these cleaved pieces onto the backing sheet, they are cut and cured using a hot platinum wire. Curing is done to produce ripples that reduce the surface energy of the edges of each piece, which later helps in efficient peeling of the pieces off the backing sheet prior to use in an experiment.

The process of cleaving is tedious and mostly arbitrarily done, it is repeated until we get surfaces that are large enough to cover at least two silica cylinders (namely circa 2 cm^2) and free of cracks or steps. Once a backing sheet is filled with numerous mica pieces, it is then

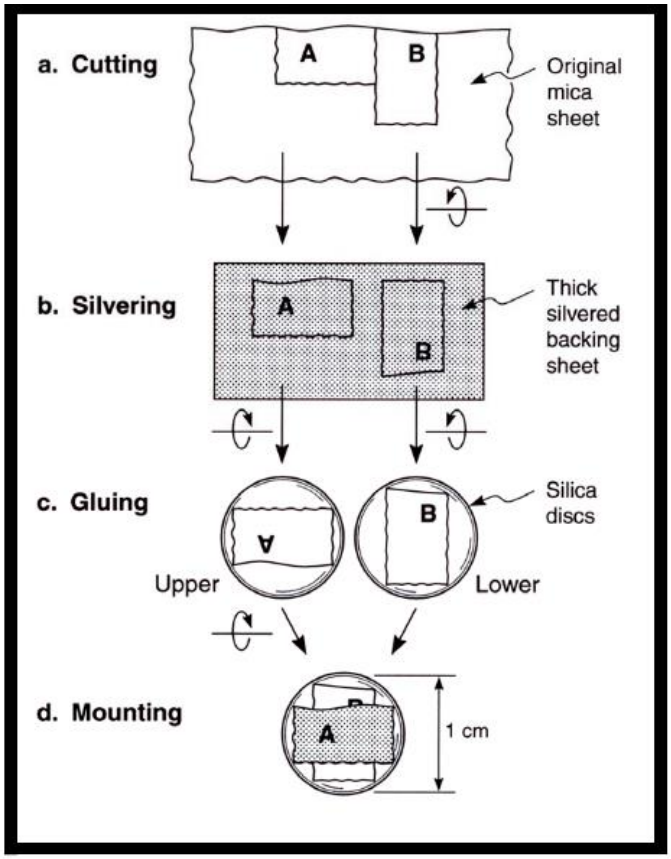

Figure 2.2 Procedure for surface preparation[9]

ready for silvering. A silver layer is deposited, using the e-beam (ANGSTROM NEXDEP) in a clean room, in a vacuum chamber of about 2.5 x 10-7 Torr, at a deposition rate of 0.05 nm/s evaporator[8]. The silver thickness is measured via atomic force microscopy (AFM) and is usually around 50-55 nm in thickness to obtain semi-transparent surfaces needed for optimal interferometric measurements. Once they are back silvered, the pieces are left on their backing sheet, sealed and stored in a desiccator. This process allows for the "perfectly adhering" mica surfaces to be protected from environmental impurities (until they are peeled off and used for experiments), therefore it is essential to ensure that the desiccator atmosphere is dry and free from greasy vapours. Failure to do so may result in uneven adhering and contamination of the mica on the surfaces.

The final preparation of surfaces consists in gluing and mounting/aligning of the mica pieces in the SFA. It is done using two silica disks with a radius of curvature of 1 cm, that are first cleaned and brought into the laminar hood to avoid contamination. Optical UV-curing glue (Norland, Cranbury, NJ), is used for gluing the mica pieces onto the cylinders. A speck of glue is poured on top of these surfaces and are rotated using curved forceps to help spread the glue evenly, and any excess glue is removed. The mica pieces are slowly peeled off the backing sheet and placed at the middle of the silica disks: They are glued, mounted in the SFA, and aligned in a manner that ensures a good matching of the crystallographic axes of each mica surface, in order to maximise birefringence, which will lead to a better splitting of the beta and gamma components of interference fringes and enhance spectral resolution during interferometric measurements.

Figure 2.2 summarises the sample preparation and mounting procedure. After the mica sheets are glued, the UV-glue is cured (crosslinked) under a UV light for about 2 hours. Importantly, all those steps are performed in a laminar hood to avoid contamination. After curing, the mounting of the two freshly prepared mica-covered silica disks is done with utmost care as not to damage the mica surfaces. One of them is placed in the upper (friction device) holder while the other one is placed in the lower (sliding device) holder. Both are firmly held in place by a Teflon-headed screw. The screwing must be done to make sure the orientation of the disks stays perfectly symmetrical, namely that both cylindrical axis are perfectly orthogonal (azimuthal angle) and that the top of both surfaces are parallel to each other, to ensure constant circular contact area during shear[9].

Preparation of lubricant solution and surfaces incubation

Two protocols were used for surface incubation in lubricant solution. The first method involved the direct incubation of the bare mica surfaces in a solution of Bovine Serum Albumin (BSA). BSA was prepared at a concentration of 8 mg/ml, 55 ul of this solution was injected in between the bare mica surfaces and left to incubate for an hour before starting an experiment. Before injection, the BSA was systematically centrifuged for 5 mins at 12 rpm to ensure that no protein aggregates were initially injected between the surfaces. Additionally, the BSA was left in the SFA experimental room to accelerate thermal equilibrium, as the room's temperature was higher than that of the sample preparation area.

The second method involved the preliminary coating of the mica surfaces with fibronectin before incubation in BSA solution. Bovine Fibronectin (FN) was prepared at a concentration of either 0.02 mg/ml or 0.3mg/ml (for experiments involving effects of FN concentration). 55 ul of this solution was injected in between the bare mica surfaces and left for an hour to ensure enough FN coverage of the mica. The FN was then gently rinsed three times using sterile PBS. Experiments involving high and low FN concentration was done two ways, either with FN surface passivation or without passivation. In the first (passivation) protocol, 55 ul of low concentration BSA (0.02 mg/ml) was injected immediately after the FN was rinsed and left to incubate for 30 mins. Following which a 55 ul droplet of high concentration BSA (8mg/ml) was left to incubate and left until the shearing experiment starts. In the second (no passivation) protocol, a 55 ul droplet of high concentration BSA (8 mg/ml) was directly injected and left to incubate till experiment starts. All the steps mentioned above were carried out in a laminar flow hood, in air, at room temperature (22-25 °C). Prior to start force measurements, a water reservoir and few droplets of DI water were added to the lower chamber of SFA to alleviate dehydration. The freshly prepared (either bare or FN-coated) mica surfaces were mounted into the SFA chamber before incubation, left in the chamber during incubation and the higher concentration BSA was used as a shearing medium. A summary of all systems tested (and associated abbreviations) is shown in Table 2.2.

Film composition	Experimental concentration (mg/mL in PBS)	Protocol abbreviation
BSA only	8.0 (BSA)	P1
BSA+$FN_{0.02}$ without passivation	8.0 (BSA), 0.02 (FN)	P2
BSA+$FN^{P}_{0.02}$ with BSA passivation	8.0 (BSA), 0.02(BSA), 0.02 (FN)	P2-P
BSA+$FN_{0.3}$ without passivation	8.0 (BSA), 0.3 (FN)	P3
BSA+$FN^{P}_{0.3}$ with BSA passivation	8.0 (BSA), 0.02(BSA), 0.3 (FN)	P3-P

Table 2.2 Materials and Concentrations Tested

2.3 Interferometric measurements of film thickness and refractive index

SFA uses interferometric Newton rings (Figure 2.3) to visualise the area of contact between the surfaces prior, during and after shear[9]. As priorly mentioned the two back silvered mica covered discs placed in a cross-axial configuration forms an optical interferometer allowing for multiple beam interferometric measurements. As white light passes through these discs, the light gets reflected back and forth by the two semi reflective silver layers forming a plano-convex "sandwich" around the two mica surfaces and the lubricant and enabling us to observe a succession of constructive (bright) and destructive (black) interference. This pattern is commonly known as Newton rings. The resulting light transmitted from this contacting surfaces' junction is then directed onto a grating spectrometer which is further connected to a CCD camera. This transmitted light consists of discrete wavelengths $\lambda_n^0 (n = 1,2,3 \dots)$ which

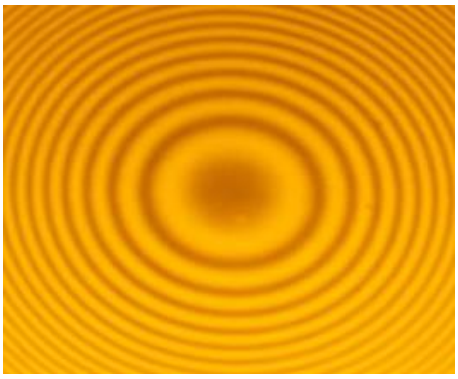

Figure 2.3 Newton rings interference pattern

can be separated and measured as sharp fringes in a grating spectrometer. These fringes of equal chromatic order (FECO) are then monitored in real-time to study the film (and mica surfaces) characteristics prior, during and after shear. More specifically, the film thickness,

the presence of aggregates (through refractive index measurements), the mica surface damage (if any) can all be assessed through the analysis of the FECO.

The SFA technique for measuring forces while visualising contacting surfaces via FECO monitoring allows us to accurately quantify the following data:

i) Simultaneous measurement of normal (adhesion) and lateral (friction) forces across surfaces subjected to pressure and/or shear in both static and dynamic conditions.

ii) Independent measurement of the separation distance between the two surfaces at their point of closest approach, at any time during the approach, shearing, and separation of the two surfaces.

iii) Quantitative assessment of the contact junction size and shape and its evolution over time while applying pressure and/or shear.

iv) Ability to monitor and characterise any type of asperities such as trapped aggregates, damage of surfaces and contamination between the surfaces. This visualization results from the alteration of both odd and even FECO interferometric fringes (see details later in this Chapter) that allow us to determine any heterogeneity in film thickness and/or film refractive index within the contacting junction.

As mentioned previously, white light passes through the back silvered sheets of mica in contact (first assessed without any medium in between them) and emerges out consisting of discrete wavelength measured as fringes. This emerging beam light is then focused into the slit of a grating spectrometer (the light must ideally enter the slit at exactly at 90°), which splits up the wavelengths as a result ordered collection of fringes are observed. They are called fringes of equal chromatic order (FECO). Using FECO, SFA allows us to measure surface separation, i.e., film thickness down to a few Å[9,10]. Considering that the two sheets of mica are of the same thickness T, when the surfaces are separated by a distance *D*, the FECO pattern shifts to a longer wavelength λ_n^D with respect to the contact position, i.e., when *D*=0, λ_n^0 (mica in contact with mica). These shifts in the wavelengths allows us to quantify accurately the distance, *D* between the surfaces. These fringe shifts are given by:

$$\tan\left(2\pi\mu\frac{D}{\lambda_n^D}\right) = \frac{2\bar{\mu}sin\left[\frac{1-\lambda_n^0/\lambda_n^D}{1-\lambda_n^0/\lambda_{n-1}^0}\pi\right]}{(1+\bar{\mu})\cos\left[\frac{1-\frac{\lambda_n^0}{\lambda_n^D}}{1-\frac{\lambda_n^0}{\lambda_{n-1}^0}}\pi\right] \pm (\bar{\mu}^2-1)}$$

where + refers to odd-order fringes (n odd), and – refers to even order fringes (n even)

$\lambda_n^D =$ Wavelength of the n odd fringe at distance *D*

$\lambda_n^0 =$ Wavelength of n odd fringe at *D*=0

$\lambda_{n-1}^0 =$ Wavelength of the even fringe $(n-1)$ at *D*=0

$\mu_{mica} =$ Refractive index of mica at λ_n^D

$\bar{\mu} = \frac{\mu_{mica}}{\mu}$

μ refers to the refractive medium between the two mica surfaces at λ_n^D.

For surface separation D<300Å, the above equation simplifies to the following two approximate equations,

$$D = \frac{nFn(\lambda_n^D - \lambda_n^0)}{2\mu_{mica}} \qquad for\ an\ n\ odd\ fringe$$

while

$$D = \frac{nFn(\lambda_n^D - \lambda_n^0)\mu_{mica}}{2\mu^2} \qquad for\ n-1\ even\ fringe$$

In the above expression, Fn is a correction factor and is given by the formula:

$$nFn = \frac{\lambda_{n-1}^0}{\lambda_{n-1}^0 - \lambda_n^0}$$

The film refractive index can then also be calculated using:

$$\mu = \mu_{mica}\sqrt{\frac{(n-1)F_{n-1}}{nF_n}\cdot\frac{\lambda_{n-1}^D - \lambda_{n-1}^0}{\lambda_n^D - \lambda_n^0}}$$

From the above equations, both the distance *D* (film thickness) and the refractive index μ can be determined independently by measuring the shifts in the wavelength of an odd and adjacent even fringe, respectively[9]. Mica is by nature a birefringent crystal; hence each fringe appears as a doublet consisting of β and γ components that correspond to the two crystallographic axes of the crystal. Therefore, the exact fringe location in the spectrum is determined by the mean of the refractive indexes of the two individual β and γ components. The mean refractive index of the medium is then equal to:

$$\mu_{mean} = 1.5820 + \frac{(4.76 * 10^5)}{\lambda^2(\text{Å})}$$

where λ = the mean of $\lambda_\beta(\text{Å})$ and $\lambda_\gamma(\text{Å})$, which are the wavelengths of the β and γ components, respectively.

Figure 2.4 shows a representative FECO pattern, as seen directly through the eyepiece of the spectrometer, of two mica surfaces in contact in air, in the absence of film (*D*=0, Fig. 2.4a) and the presence of a 10 nm film trapped between the mica surfaces (*D*=10 nm, Fig. 2.4b). The shift of wavelengths ($\Delta\lambda_n = \lambda_n^D - \lambda_n^0$ of the n-odd fringe,) between panels 4a and 4b corresponds to the difference between the 'position' of the n fringe before and after a film is introduced between the surfaces and allows us to determine the film thickness accurately. The additional three vertical lines visible in panel 4a are the green and yellow mercury lights, which are used as references for the calibration of spectrometer dispersion, as discussed below.

It can also be noted that the shape of odd and even fringes is significantly different. The even ordered fringes are wide and curvy. Even fringes have a maximum electric field at the centre of the junction (hence at the centre of the confined film) and are very sensitive to the optical properties of the film. During analysis, the even fringe is therefore preferred for identifying film aggregation, individual aggregates, and calculation of the refractive index. Instead, odd fringes appear sharper and narrower than their even ordered counterpart. Odd fringes have a minimum electric field at the centre of the junction and are therefore much less sensitive to film properties. In such a context, they are used for accurate distance (film thickness) measurements. The flattening of the FECO tip observed in particular in Fig. 2.4a,

i.e., at *D*=0, is due to elastic deformation of the glue used to mount the mica pieces onto their silica substrates, the larger the flattening, the larger the adhesion force between mica surfaces[6].

The first step towards quantitative measurements of film thickness and forces is to determine the spectrometer dispersion. This operation requires the use of a mercury white lamp, with well-defined lines of known wavelengths. In our experiments, the green and the two yellow lines (see associated wavelengths on next page) were used as reference wavelengths to (i) calculate spectrometer dispersion, and (ii) monitor the wavelength of odd(n) and even(n-1) contact fringes. The reason behind exclusively limiting the use of FECO located within the green-yellow spectral region is because our entire experimental setup (mica + glue + lubricant) had a minimum absorbance in such region.

The 0th position, i.e., the position at which *D*=0 is first considered where the surfaces are in contact with each other. This first snapshot is acquired using Light Field. The positions of the green and yellow lines respectively are calculated laterally using an ImageJ software (keeping the leftmost edge of the CCD screen as the reference, a.k.a., the 0th point). Various

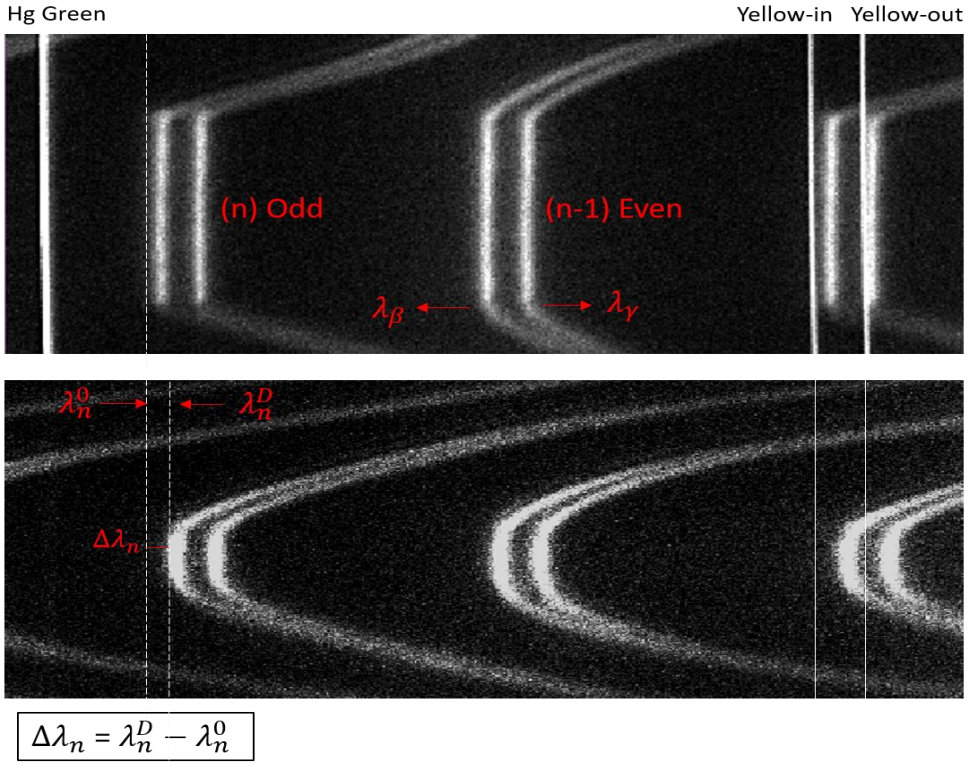

Figure 2.4 a) FECO pattern reflecting the size and shape of contacting mica surfaces at D=0 (no film in between); b) FECO pattern in presence of a film, i.e., when the mica surfaces are separated by a distance D

reading spread across are marked, and a mean value is calculated for further calculations. The absolute wavelength of the green, yellow-in, and yellow-out lines being already known, if the mean value which is calculated respectively for each wavelength of light is taken as *X*, we can use these to calculate the dispersion (***DP***) of the spectrometer in Å/pixel as follows:

$$\boldsymbol{DP} = \frac{\left(\lambda_{yellow-in} - \lambda_{Green} \Big/ X_{yellow-in} - X_{Green}\right) + \left(\lambda_{yellow-out} - \lambda_{Green} \Big/ X_{yellow-out} - X_{Green}\right)}{2}$$

where

$\lambda_{Green} = 5460.75$ Å

$\lambda_{Yellow-in} = 5769.59$ Å

$\lambda_{Yellow-out} = 5790.654$ Å.

The above estimate is based on the pixel distance calculated via the ImageJ software. A tiny miscalculation would lead to significant errors on film thickness, which is why multiple readings are performed to determine accurately ***DP***. Next step is to determine the wavelength of the odd(n) fringe at *D*=0, by averaging the pixel distances *X* of both the β and γ components, λ_n^0(Å):

For calculating λ_β(Å),

$$\lambda_\beta(\text{Å}) = \left[\left(X_{\beta\_\text{mean}} - X_{Green}\right) * DP\right] + \lambda_{Green}$$

Similarly,

$$\lambda_\gamma(\text{Å}) = \left[\left(X_{\gamma\_\text{mean}} - X_{Green}\right) * DP\right] + \lambda_{Green}$$

Finally,

$$\lambda_n^0(\text{Å}) = mean(\lambda_\beta, \lambda_\gamma)$$

where

X_{β_mean} =mean of all the pixel readings taken for the β component

X_{γ_mean} =mean of all the pixel readings taken for the γ component

The wavelength of even fringe (n-1) is also calculated with their corresponding wavelength of the components.

$$\lambda_{n-1}^{0}(\text{Å}) = mean(\lambda_{\beta}, \lambda_{\gamma}),$$

565nm	Green	Yellow in	Yellow out	n		n-1	
				β	γ	β	γ
	19	403	429	178	197	333	356
	20	403	430	178	197	333	356
	21	403	429	177	198	334	357
	22	404	430	175	198	335	357
	19	404	431	175	196	336	358
Average	20.2	403.4	429.8	176.6	197.2	334.2	356.8

Table 2.3 Pixel readings for green, yellow-in, yellow-out lines, n – odd fringe, and n-1 – even fringe

Mercury light	λ (Å)	λ (pixel)	Average Dispersion ***DP***	$\lambda_{n}^{0}(\text{Å})$	$\lambda_{n-1}^{0}(\text{Å})$
Green	5460.75	20.2	0.80569	5595.058	5722.841
Yellow-in	5769.59	403.4			
Yellow-out	5790.654	429.8			

Table 2.4 Wavelengths of green and yellow lines, corresponding average spectrometer dispersion calculated, and wavelengths of n- odd and n-1 even fringes of contacting mica surfaces.

Table 2.3 displays an example of such pixel readings extracted from one of our experiments. In Table 2.4, we calculate spectrometer dispersion ***DP***, by reporting the pixel readings of the green, yellow in and yellow out lines ($X_{Green} = 20.2$; $X_{Yellow-In} = 403.4$; $X_{Yellow-out} = 429.8$), in the following expression:

$$\boldsymbol{DP} = \frac{\left(5769.59 - 5460.75/403.4 - 20.2\right) + \left(5790.654 - 5460.75/429.8 - 20.2\right)}{2}$$

$$\boldsymbol{DP} = 0.80569.$$

Now to calculate the wavelength of the n – odd mica fringe $\lambda_n^0(\text{Å})$, we need to calculate the wavelengths of its two β and γ components first.

$$\lambda_\beta(\text{Å}) = [(176.6 - 20.2) * 0.80569] + 5460.75$$

$$\lambda_\beta(\text{Å}) = 5586.76\,;\ \lambda_\gamma(\text{Å}) = 5603.357$$

$$\lambda_n^0(\text{Å}) = \frac{5586.76 + 5603.357}{2}$$

Finally,

$$\lambda_n^0(\text{Å}) = 5595.058;\ \lambda_{n-1}^0(\text{Å}) = 5692.16$$

Line	Time (Sec)	β_n (Pixel)	γ_n (Pixel)	$\lambda_n^D(\text{Å})$
626	218.88	497.18	506.02	5848.60906

$\lambda_n^D - \lambda_n^0(\text{Å})$	μ_{mica}	$D_n(\text{Å})$	$D_n(nm)$	F/R *(mN/m)*
253.5506	1.595935	3557.667	355.7667179	2.728487

Table 2.5 A snippet of the data from the FECO shown in Figure 2.4

Table 2.5 reports from left to right, the line which denotes the frame number, the real time associated with that frame number, β_n which corresponds to the pixel distance of the nth

fringe β component and next its γ component. Similarly, to previously shown calculation for λ_n^0, λ_n^D is determined from the pixel values of both its components. Next column corresponds to the subtraction of both the wavelengths $\lambda_n^D - \lambda_n^0$. Refractive index of mica is also reported, as calculated using the formula below. For every position of n (odd) fringe, film thickness *D* can be calculated once λ_n^D and μ_{mica} are known (here in Angstroms). *D* is further used to measure forces between the surfaces at that time and position using pixel values and other known reference values mentioned later.

Now to calculate μ_{mica}

$$\mu_{mica} = \mathbf{1.582} + \frac{\mathbf{4.76 * 10^5}}{(\lambda_n^D)^2}$$

We can calculate λ_n^D, using the prior method, $\lambda_n^D = 5848.60906$

$$\mu_{mica} = \mathbf{1.582} + \frac{\mathbf{4.76 * 10^5}}{(5848.60906)^2}$$

$$\mu_{mica} = \mathbf{1.5959}$$

Once λ_n^D and μ_{mica} are known, D_n can be calculated using the following formula:

$$D_n = \frac{nFn * (\lambda_n^D - \lambda_n^0)}{2 * \mu_{mica}}$$

nFn is the fringe number that needs to be followed while analysing all our force runs and can be calculated using the following expression:

$$nFn = \frac{\lambda_{n-1}^0(\text{Å})}{\lambda_{n-1}^0(\text{Å}) - \lambda_n^0(\text{Å})}$$

$$nFn = 44.78583$$

$$D_n = \frac{44.78583 * (5851.239643 - 5595.058488)}{2 * 1.5959}$$

$$D_n = 3594.606011 \text{ Å}$$

$$D_n = 359.4606011 \text{ nm.}$$

2.4 Normal force measurements

In the SFA, the lower mica surface is mounted on a horizontal double cantilever spring, which is calibrated and used for the measurement of normal forces between the surfaces. The spring constant K ($^{N}/_{m}$) is calculated before the experiment by using a series of small weights of known mass, and by measuring spring deformation. The value of the normal spring K in our experiment was $1656\ ^{N}/_{m}$. During an SFA experiment, Hooke's law is then applied using the information from the surface separation distance and the amount of spring deflection, to measure the normal force between the two surfaces. While the upper mica surface is fixed, the double spring holding the lower surface is moved up and down using a step motor connected to a DC power supply. Surfaces are brought in contact and normal forces are applied (by the upper surface onto the lower surface), because of the interaction, the spring is deflected. During compression, the spring is deflected in a downward direction, and repulsive forces are measured. When surfaces are separated, when/if the spring is deflected in an upward direction towards the upper surface, then attractive forces can also be measured. In all experiments reported in this thesis, no adhesion forces were ever observed, therefore only repulsive forces are reported.

Importantly, the speed and linearity of the step motor are calibrated before each experiment by monitoring the displacement of the FECO pattern *vs*. time, while the motor is "on" and no forces are acting on the surfaces. Concretely, while approaching the surfaces (but still far from contact) the position of the lower surface, called D_0 is recorded as a function of time, to calculate motor speed and to check motor linearity. When the lower surface comes in contact and starts pushing against the upper surface, it causes the spring to deflect. At any time (and surface position), the spring deflection is given by $D - D_0$. Where D is given as the distance between the two surfaces caused by the deflection D_0. The force at this position is therefore simply given by:

$$F = K(D - D_0)$$

This equation allows us to determine the nature of surface forces:

$i)$ $D < D_0$, we are in presence of attractive (adhesion) forces.

$ii)$ $D > D_0$, we are in presence of repulsive forces.

Therefore, as displayed in Figure 2.5, in all our normal forces measurements, surface separations are first reported as a function of time, away from contact (where $F = 0$) to (i) get the speed of the motor[9], and (ii) establish the range of the linear regime, i.e., determine the surface separation at which forces start being present ($F \neq 0$), not shown here.

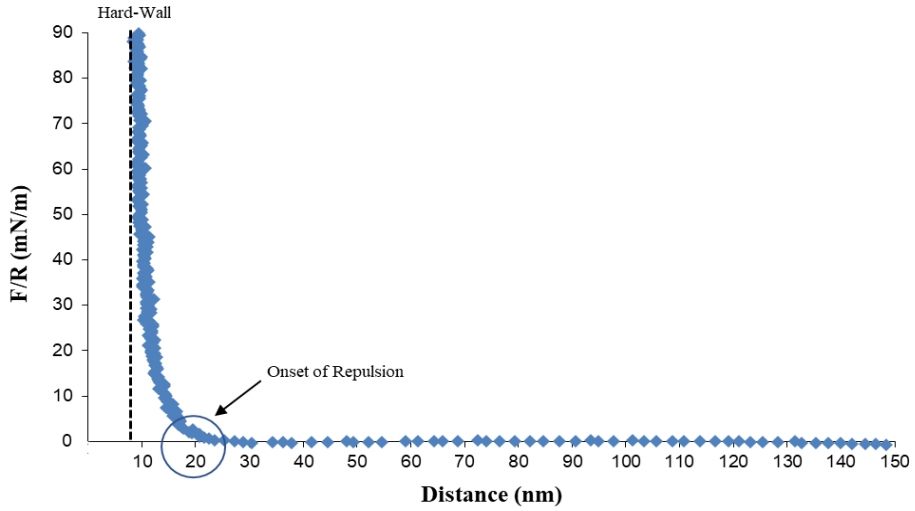

Figure 2.5 Normal force F/R vs. distance profile of a BSA film under compression

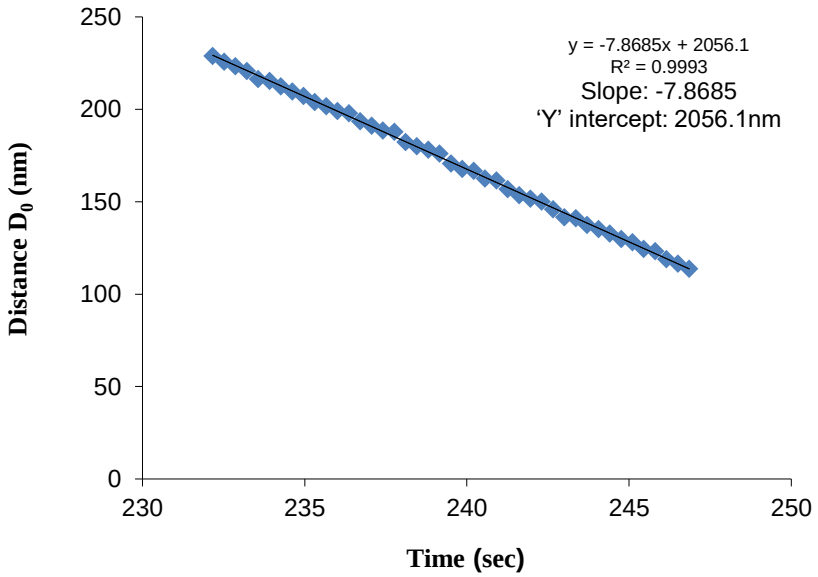

Figure 2.6 The linear regime of the distance vs. time is used to calculate the speed of the step motor used to displace the lower surface.

Note that, in Table 2.5, the last column reports the Force/Radius (F/R) value for a given frame number (FPS) and distance (D_n), correspondingly. F/R measurements are performed at any time during the approach of surfaces, and are plotted against surface separation, i.e., distance, to get the normal force profile. When a film is present between the surfaces, the distance is then equal to the film thickness and the force profile denotes the overall response of the film under compression, as displayed in Figure 2.6. The radius of the silica discs used in our experiments was R = 1 cm.

In presence of a film between the surfaces, since the normal loads applied in our experiments were not strong enough to deform significantly the mica sheets glued to the silica discs, the radius R of the surfaces remained constant throughout our measurements. Also, because of the geometry of our setup, namely, a sphere interacting with a sphere, the interaction energy increases linearly with radius R, but the distance dependence of the interaction will not change to that corresponding to two planar surfaces. In other words, the effective area of interaction of a sphere with a surface is the circular zone centred at a distance - D from the surface (inside the sphere). This is known as the Derjaguin approximation. The effective area of interaction increases linearly with both R and D as may be expected and hence we report Force as a function of R[11,12].

Table 2.5 displays our methodology for calculating F/R values, by giving "one" example of *F/R* measurement (based on the FECO snapshot captured in Figure 2.4). FPS (Frames Per Sec.) are previously acquired while recording the data via our CCD camera (attached to the spectrometer). The FPS for this experiment was 2.86, which means that each frame took 0.34965 sec. So, the time at which frame 626 was captured can be simply be calculated by multiplying FPS by the time taken for one frame., i.e., $t = 218.88\, sec$. Now, at $t = 0$, we know that the position of the motor was at $2056.1\, nm$ ('Y' intercept). Therefore, the total displacement at $t = 218.88\, sec$ will be $-7.8685\, nm/sec$. The negative sign indicates a negative slope of the linear regime, which is normal when surfaces are approaching from one another (distance decreasing). This value will be considered as the speed of the motor.

Hence,

$$displacement_{t=218.8809} = (speed * time)$$

$$displacement_{t=218.8809} = -1722.264\ nm$$

Now,

$$D_0(total\ displacement) = displacement_{t=218.8809} + position\ at\ t = 0$$

$$D_0 = -1722.264 + 2056.1$$

$$D_0 = 333.836\ nm$$

Since the radius R of the silica discs remains approximately constant throughout our force application (unless high pressures are applied, which was not the case here), the force F could be measured over radius R as follows:

$$F/R = K(D_n - D_0)/R$$

$$F/R = 1656000[355.766717-(333.836)]mN/cm$$

$$F/R = 2.728487\ mN/m$$

To display the entire force profile shown in Figure 2.6, *F*/*R* values are calculated for each frame and plotted against distance. In the large distances' regime, the lower surface is far from contact with the upper surface, leading to $F = 0$. Such regime is used to determine motor speed and linearity (Figure 2.5). Upon further approach, surfaces enter in "contact", spring deflection starts and $F \neq 0$. When a film is present between surfaces, the distance at which such onset of interactions occur corresponds to the undeformed 'equilibrated' film thickness. If we continue pressing, *F* increases nonlinearly with distance, and we called "hard wall" the thickness of the film under maximum applied load.

2.5 Friction forces measurements

2.5.1. Shearing surfaces using a piezoelectric bimorph slider

The bimorph slider (Figure 2.7) is an important accessory part of the SFA. It consists of two parallel sectored piezoelectric ceramics strips that enable smooth lateral (shear) motion of the lower surface. When a voltage is applied using a function generator, one of these strips expands while the other contracts, resulting in bending of the ceramic, and overall lateral displacement of the lower surface. Various types of displacement time functions (step-

function, saw-tooth, sinusoidal) can be generated, ranging from few micro-Hertz to 100Hz. In our experiments, a triangular signal, which amplitude was centered on 0 Volts, was used to achieve symmetric back and forth lateral movement at constant velocity, as the deformation of each strip is proportional to the applied voltage. A frequency of 0.5 Hz and a peak to peak amplitude ranging from 5 V to 20 V were used, corresponding to sliding speeds from 0.875 to 3.5 μm/s. Sliding speeds is obtained by first calculating the time taken for one shearing cycle by using the using frequency (Time (sec) = 1/ frequency (Hz)). We are then able to calculate velocity by known time and distance. The unit shown in Figure 2.7 consists of (i) the bimorph slider described above, which is used to actuate shear and which is attached to a double cantilever *horizontal* spring holding the lower SFA surface (used for the normal forces measurements mentioned in Section 2.4) and (ii) the friction device, which is used to detect the resulting friction forces and which is attached to a double cantilever *vertical* spring holding the upper SFA surface (used for the friction forces measurements mentioned in Section 2.5.2 below)

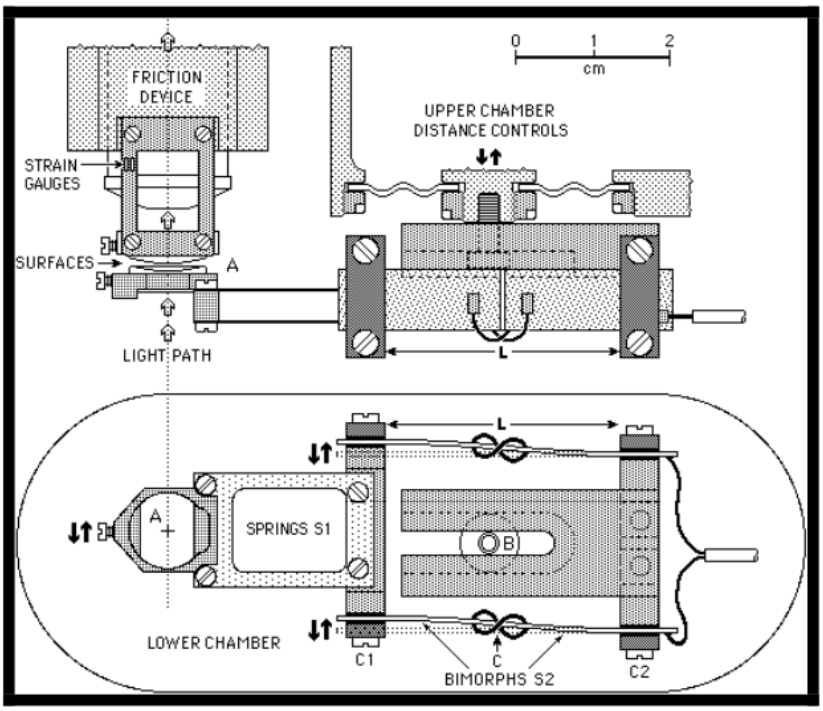

Figure 2.7 The bimorph slider attachment and the friction device used for shearing and detecting friction, respectively. Shearing can be applied over a large range of driving amplitudes and frequencies, hence of sliding velocities.

2.5.2. Measuring lateral (friction) using a friction device attachment

The upper surface is mounted on the so-called the friction device, which consists of a vertical double-cantilever, Cu-Be (copper-beryllium) springs holding the upper SFA surface. One of these vertical springs serves as a force sensor by attachment of four strain gauges to it, shaping the four arms of a Wheatstone bridge. The friction device is rigidly clamped on top of the main chamber. This device comes in varied sensitivity levels (spring stiffness) depending on the range of frictional forces that needed to be detected.

When shear is applied (via the bimorph slider) while the two SFA surfaces are in contact, the vertical springs of the friction device will deflect, and the strain gauges attached to the springs will measure this deflection. Figure 2.8 displays the triangular signal applied to the bimorph slider to shear the surfaces and Figure 2.9 shows the resulting friction signal, in the form of rectangular friction loops. The upper (positive) section of the loop denotes the friction between opposing surfaces during left-to-right displacement, while the lower (negative) section of the loop denotes the friction between opposing surfaces during right-to-left displacement. Overall, the friction force is measured as an average between the two left-

Figure 2.8 Triangular signal used as input for the bimorph slider, typically here 5V peak-to-peak amplitude at 0.05Hz

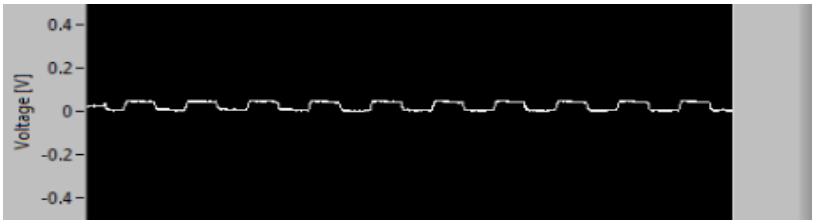

Figure 2.9 Friction output signal (friction loops), as recorded by our friction device.

to-right and right-to-left values, first in Volts (V) and later converted into mN after calibration of the friction device. Such calibration is similar to that of the horizontal double spring (using a series of weights of defined mass) to (i) establish the relation between voltage readout (V)

and force (mN), (ii) ensure linearity of friction *vs*. spring deflection and (iii) correct the balance between left-to-right and right-to-left displacements.

2.6 Fitting normal force profile to quantify film stiffness

Normal force data such as the one displayed in Figure 2.5 was not only used to extract film thickness under normal load, but also estimate film stiffness, i.e., determine its (compressive) Young modulus. To do so, further curve fitting was performed using the Johnson contact mechanics[13] (Figure 2.10) in which the indentation of the matrix under compression, δ, is related to the normal force *F* by the following equation:

$$\frac{F}{R} = E\pi\frac{\delta^2}{D_0}$$

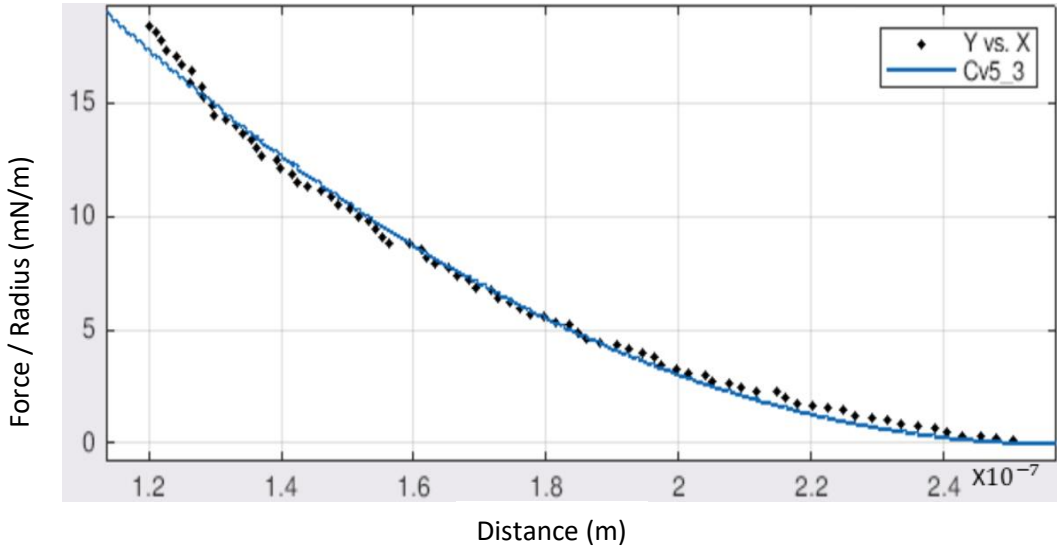

Figure 2.10 Example of normal force profile fit using the Johnson contacts mechanics; here for a BSA+FN (0.02) film, a value of E= 109.2±9.4 kPa was found. R-square: 0.96

where $\frac{F}{R}$ is the force over the radius of curvature, D_0 is the constant value at which the surfaces start 'feeling' each other, i.e., the film thickness at rest (uncompressed) mentioned previously as the onset of repulsion, and *E* the resulting Young modulus. δ^2 is defined as $(D - D_0)^2$ where *D* is the distance between the two surfaces. Fitting of curves for the estimate of stiffness was done using MATLAB (MathWorks, Natick MA).

2.7 Estimating size and shape of aggregates using FECO pattern

FECO patterns were recorded before, during, and after shearing to monitor the size and shape of the surfaces, the formation of aggregates, and their evolution over time. Because the even-ordered fringes are very sensitive to optical properties of medium (they combine refractive index and distance information) we avoided using them to quantify aggregate size. We here show how we used odd-ordered fringes for accurate measurement of average film thickness and size of aggregates. Since a right-angle triangle prism was used for directing the resulting Newton interference rings from the objective onto the spectrometer slit, we also used it to "scan" through the sheared junction and estimate the number of aggregates formed over time (Figure 2.11). It is important to note that, when using a spectrometer, the FECO display only one cross section of the entire Newton rings pattern. During normal force measurements, we usually focus on the middle contact section, which is also called the point of closest approach, i.e., the minimum film thickness. However, during shearing measurements, aggregates form and the confined/sheared film becomes heterogeneous so we may miss out lots of events when monitoring only the middle contact of junction. Rotating back and forth the right-angled prism (See schematics Figure 2.11) allows us to "image" various cross-sections of the sheared junction and to estimate number, size, and shape of the aggregates present. The rotation of the prism around the middle section should be small and slow, to assess aggregates properties, otherwise the entire FECO pattern quickly gets out of focus.

2.7.1 Estimating the dimensions of aggregates

To calculate aggregate thickness, we used the same method already described in Section 2.3 for calculation of average film thickness, except that we focused on small lateral portions of the FECO pattern, where we "saw" aggregates had formed (Figure 2.11). Briefly, the pixel location of $\lambda_{(n)\beta}^{A0}$ was first measured using Image J software, as the reference point (no film present), also called the zero point. In all aggregate's measurements, we systematically use the β component of each fringe as clear endpoint (since it could get difficult to distinguish precisely β and γ components when aggregates formed) Likewise, the pixel positions of $\lambda_{(n)\beta}^{Ax}$ were also measured. Where x corresponds to the number of aggregates that were visible in each frame number. Each small rotation of the prism was recorded at different

frame numbers. Overlapping aggregates were identified and averaged, and new aggregates in each frame number were marked as $x = 1,2,3 \ldots n$.

$\lambda^{A0}_{(n)\beta} = Wavelength\ of\ (n) odd\ fringe\ at\ distance\ (A)$

$\lambda^{Ax}_{(n)\beta} = Wavelength\ of\ (n)\ odd\ fringe\ at\ each\ aggregates\ (Ax)$

Finally, we could calculate the difference between the positions of the reference and each aggregate giving us both the distribution and the individual aggregate size using the expression:

$$\Delta\lambda^{Ax}_{(n)\beta} = \lambda^{Ax}_{(n)\beta} - \lambda^{A0}_{(n)\beta}$$

In an attempt to measure the size of possible small aggregates which may be "hidden" by the bigger ones separating the surfaces (See schematics Figure 2.11), more pressure was applied at the end of each experiment to flatten the surfaces. Another inspection of the contacting junction was then performed by rotating the prism to measure the size of smaller aggregates that were not documented/visible before. However, the drawback of this method is that there is a chance of underestimating the size of those aggregates since pressure likely leads to their flattening/deformation. The results of this size distribution curve are then compared with the data obtained via the new force-runs performed after shear, where the onset of repulsion between surfaces was designated as the average size/diameter of the biggest aggregates formed during our shearing experiment.

The friction data was acquired using LabView (National Instruments, Austin TX) meanwhile Light-field (Princeton Instruments, Trenton NJ) was used to carry out the experiments to acquire interferometric (FECO) data. Analysis of the acquired data was carried out using MATLAB (MathWorks, Natick MA), Microsoft Excel and Image J (NIH, Wisconsin).

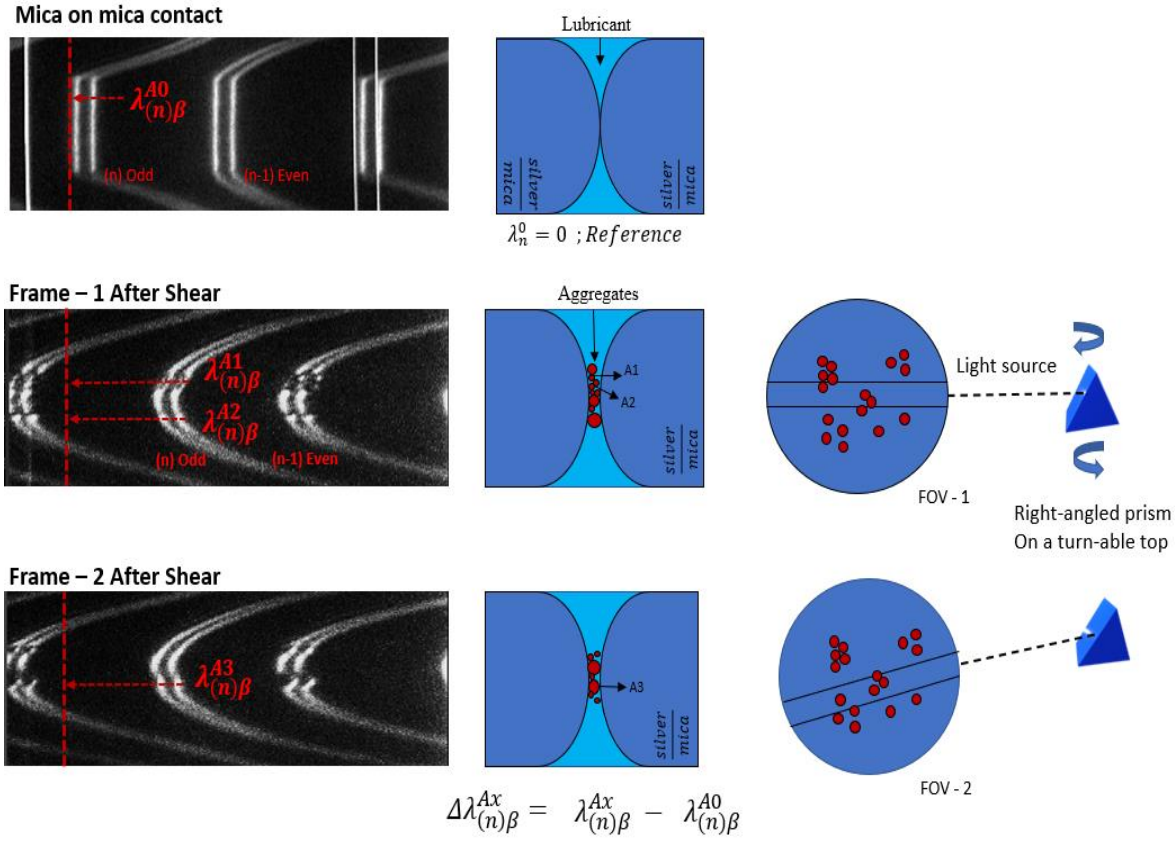

Figure 2.11 schematic showing the measurement of aggregate size using the scanning of right-angled prism.

2.8 Confocal microscopy

Finally, we also used fluorescence microscopy to image our shear-induced aggregates with the aim of evaluating their composition, after we labelled both fibronectin and albumin with Alexa fluorophores. Confocal microscopy or most frequently referred to as confocal laser scanning microscopy (CLSM) is defined as an optical imaging technique using a spatial pinhole to block out of focus light in image formation for increasing optical resolution and contrast of a micrograph[14]. For our experiments involving CLSM, single labelling of BSA was done using Alexa-488 green fluorophore, and single labelling of fibronectin was done using Alexa-594 red fluorophore. Thin focal planes of fluorescence (as seen in Figure 2.12) from both fluorophores were collected sequentially after samples were hit with respective laser lines (λ = 488 nm and λ = 561 nm), and out of focus emitted light below and above the focal planes were filtered via a pinhole (Figure 2.12).

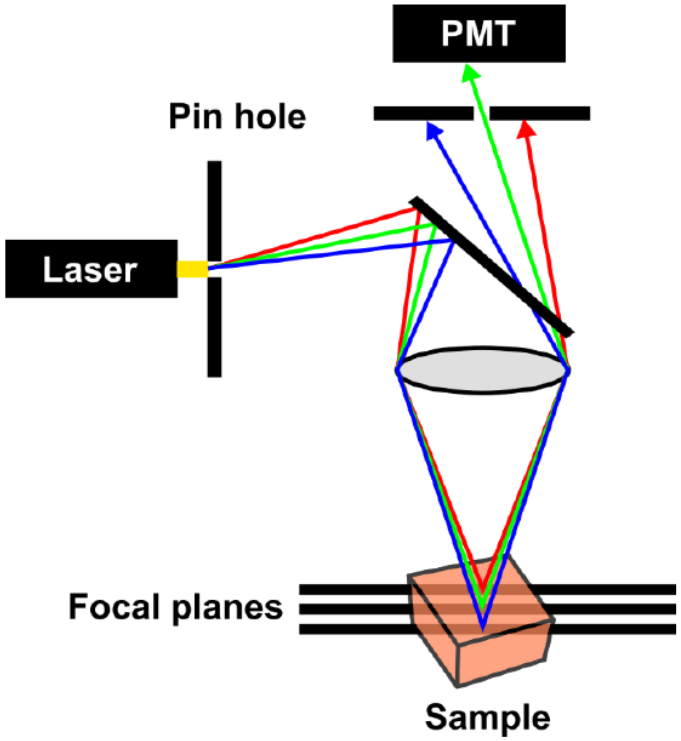

Figure 2.12 Confocal microscope light path.

This technique was used in this thesis to characterise the composition of the aggregates, more specifically to understand if they comprised only albumin (sheared medium protein) or both albumin and fibronectin (surface coating protein). Since the confocal microscope enables

for optical sectioning of tiny specimen, we used it to slice up aggregates and "quantify" its constituents (BSA / FN) by investigating the colocalization of fluorescence emitted by both the BSA and FN channels at specific locations (pixels) of the specimen slices. Following a shearing experiment, SFA surfaces were separated and then imaged using a Zeiss LSM 880 confocal microscope (Zeiss, Munich, Germany) with an apochromat oil-immersion 63x/1.4 objective, a pinhole of 11.3 AU, a 488 nm laser and 561 nm laser lines set at 30% power to capture 12-bit z-stack images. A large numerical aperture (1.4) was used as larger apertures ensure a greater magnification (by increasing the emission cone angle).

Initially, we intended to use the confocal microscope to assess both the composition and the size of aggregates. However, our resolution was too low (mainly diffraction-limited) to clearly image single aggregates, so we used our microscope to assess the composition of various small ensembles of shear-induced aggregates left at the surface.

To image our samples, we proceeded as follows: At the end of a shearing experiment, the two surfaces were separated and the silica disks supporting the surfaces were carefully removed from the SFA chamber. This step was done in a biosafety hood, after carefully removing the liquid meniscus of sheared lubricant from the junction, to avoid disrupting the aggregates formed at (and adhering to) the sheared surfaces. For imaging purposes, the surfaces were then placed inside home-made PDMS holders, covered with a microscope cover slip, and positioned upside down (curved surface facing the objective lens) to enable direct imaging of the curved surface area previously sheared. The difficulties we encountered using confocal microscopy to image the aggregates were due to (i) the rather large overall size of our mica surfaces (nearly 1 cm^2), (ii) the significantly smaller size of the sheared area where aggregates were located (circa $962.11\ \mu m^2$), and finally the size of the aggregates (average diameter between 50 nm and 400 nm). Therefore, a low magnitude objective (20x, air) had to be used first to identify the sheared spot, and once the shear spot was located, a higher aperture objective (63x, oil) was utilized to capture a close-up view of the sheared spot.

2.9 References

1. Jost, H. P. Lubrication (Tribology)–A report on the present position and industry's needs. *Dep. Educ. Sci. HM Station. Off. London, UK* (1966).

2. Mo, Y., Turner, K. T. & Szlufarska, I. Friction laws at the nanoscale. *Nature* **457**, 1116–1119 (2009).

3. Pina, C. M., Pimentel, C. & Gnecco, E. *Fundamentals of Friction and Wear on the Nanoscale*. *NanoScience and Technology* (Springer International Publishing, 2015).

4. Drummond, C. & Richetti, P. Surface forces apparatus in nanotribology. *Nanosci. Technol.* **31**, 17–34 (2015).

5. Gourdon, D. *et al.* Mechanical and structural properties of BaCrO4 nanorod films under confinement and shear. *Adv. Funct. Mater.* **14**, 238–242 (2004).

6. Israelachvili, J. *et al.* Recent advances in the surface forces apparatus (SFA) technique. *Reports Prog. Phys.* **73**, (2010).

7. Tabor, D. Mica in the service of surface science. *Colloids and Surfaces* **65**, ix–xiii (1992).

8. Samak, M. S. Role of serum albumin aggregation in lubrication and wear protection of shearing surfaces. *MSc Thesis Univ. Ottawa* (2019).

9. Israelachvili, J. *USER'S MANUAL for SFA3 and SFA2000 with Attachments*. (2009).

10. Israelachvili, J. N. Thin film studies using multiple-beam interferometry. *J. Colloid Interface Sci.* **44**, 259–272 (1973).

11. Israelachvili, J. *Intermolecular and Surface Forces*. *Intermolecular and Surface Forces* Amsterdam: Academic Press and Elsevier (2011)

12. Lang, P. Physics of Soft Colloidal Matter – Interaction potentials and colloidal stability –. (2007).

13. Wang, K. *et al.* Stiffening and unfolding of early deposited-fibronectin increase

proangiogenic factor secretion by breast cancer-associated stromal cells. *Biomaterials* **54**, 63–71 (2015).

14. Cheng PC & PC, C. *Handbook of Biological Confocal Microscopy (Pawley JB, 3rd ed.). Springer* **189**–**90**, (2006).

15. Lu, Q., Wang, J., Faghihnejad, A., Zeng, H. & Liu, Y. Understanding the molecular interactions of lipopolysaccharides during E. coli initial adhesion with a surface forces apparatus. *Soft Matter* **7**, 9366–9379 (2011).

Chapter 3 – Results

3.1 Dynamics of aggregates' formation

This research aimed at measuring and interpreting the shear-mediated transformation of serum albumin (SA) films, in presence of the linker protein fibronectin (FN). Specific focus was concentrated on SA film's roles in surface protection against wear and lubrication, using various concentrations of FN to anchor SA at the surfaces. To achieve that, we first focused on understanding the dynamics of aggregation of SA, a protein abundantly found in SF yet often overlooked. This chapter includes the measurement of the tribological properties of SA films (friction/lubrication and wear), simultaneous to the monitoring of film thickness evolution and aggregates formation. Additionally, structure, mechanics and composition of those aggregates were documented in detail. Along with studying the role of SA behaviour under shear, we also investigated the effect of SA attachment to the underlying mica surface by using various concentrations of FN. The three FN concentrations used, and adsorption/shearing protocols are reported in Table 3.1. Prior research in our group allowed us to identify the variables responsible for the formation of aggregates by investigating a large range of shearing parameters[1]. These studies show that low applied load/pressure and slow shearing speeds ensure the formation of aggregates in the films[2]. Therefore, in all the experimental protocols of this thesis, the surfaces were systematically sheared for one hour at a fixed slow shearing velocity of 3.5 μm/s under average applied loads of 1–2 mN, corresponding to average pressures of 3.5–5.5 MPa.

Overall, our dynamic study of aggregation reports the following structural and mechanical information:

vii) Film thickness and presence of aggregates
viii) Average aggregate size and shape (aggregate diameter)
ix) Distribution of aggregates (homogeneity/heterogeneity)
x) Longevity of aggregates
xi) Stiffness of aggregates
xii) Mobility of aggregates
xiii) Composition of aggregates

Each of these properties was investigated for four different proteins films and protocols, while simultaneously shearing the films and measuring (lateral) friction forces.

Film composition	Experimental concentration (mg/mL in PBS)	Protocol abbreviation
BSA only	8.0 (BSA)	P1
BSA+$FN_{0.02}$ without passivation	8.0 (BSA), 0.02 (FN)	P2
BSA+$FN_{0.02}^{P}$ with BSA passivation	8.0 (BSA), 0.02(BSA), 0.02 (FN)	P2-P
BSA+$FN_{0.3}$ without passivation	8.0 (BSA), 0.3 (FN)	P3
BSA+$FN_{0.3}^{P}$ with BSA passivation	8.0 (BSA), 0.02(BSA), 0.3 (FN)	P3-P

Table 3.1 Materials and Concentrations Tested

Table 3.1 summarizes our testing conditions. The first series of experiments performed was shearing a simple film of bovine SA (BSA) between bare mica surfaces (no FN present), referred to as 'BSA only' experiments or P1. In the next series of experiments, we used FN to anchor BSA to the mica surfaces, varying FN concentration and/or incubation (passivation) protocol: a low FN concentration (0.02 mg/ml) referred to as BSA+$FN_{0.02}$ film or P2 and a high FN concentration (0.3 mg/ml) referred to as BSA+$FN_{0.3}$ or P3 were tested at first without BSA passivation, second with BSA passivation, referred as BSA+$FN_{0.02}^{P}$ or P2-P (for low FN concentration) and BSA+$FN_{0.3}^{P}$ or P3-P (for high FN concentration), respectively. The last two protocols (P3 and P3-P) allowed us to compare our data with already known (and published) phenomenon associated with the effect of BSA on the unfolding of FN, which significantly affects the resulting friction of the system. [3,4]

3.1.1 Evolution of aggregates' formation of 'BSA only' films (P1)

The monitoring of both film characteristics and aggregates formation (via FECO images) were acquired in real-time during shear. Figure 3.1 and Figure 3.2 show the evolution of film thickness and the corresponding FECO pattern, respectively, when 'BSA only' (P1) films were subjected to shear. As explained in detail in Chapter 2, the SFA technique permits simultaneous monitoring of both FECO position and FECO shape, which allow us to quantify both film thickness and presence of heterogeneities/aggregates in the junction, respectively. Figure 3.1 indicates that 'BSA only' (P1) films thicken with time, abruptly at first, then slowly when shear is prolonged. The magnitude of initial film thickening is given by $\Delta D_{BSA} = 56.6 \pm 3.6\, nm$. The occurrence of the first aggregates is shown in Figure 3.2 (top panel) by the multiple ripples observed on the even fringe (indicative of nascent regions in the film that exhibit a different refractive index (RI) than the bulk surrounding film, as shown in detail in section 3.4). These aggregates form almost concomitantly with the start of shear, namely after 19 sec, which roughly translates into 0.97 shearing cycle (one cycle of shearing equals to 20 sec) and 69.75 µm of shearing distance (shearing amplitude is 70 µm per cycle). As shear is prolonged (Fig. 3.2, middle panel), the ripples get not only more pronounced on the even fringe but also start being noticeable on the odd fringe, indicating that aggregates are now more numerous and larger, as they start obstructing the light path across the sheared junction.

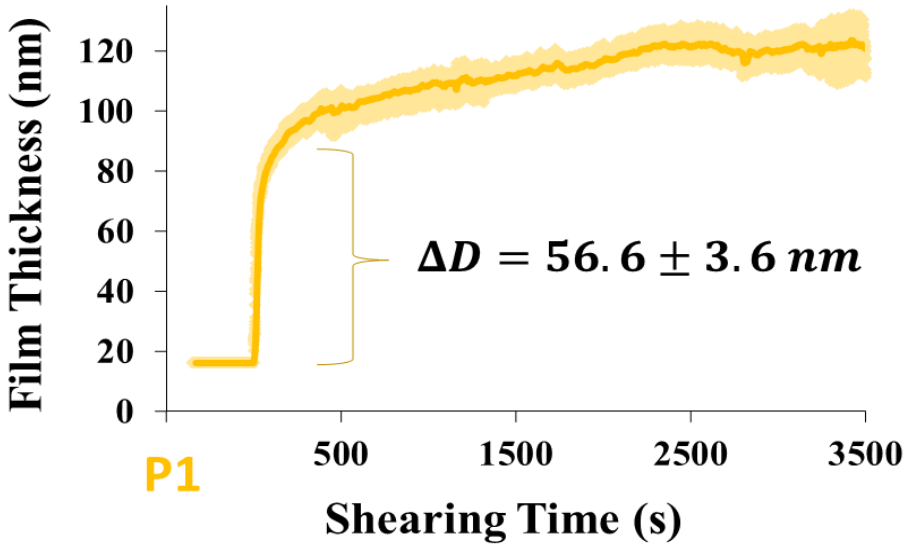

Figure 3.1 Evolution of average film thickness vs. time of shearing for "BSA only" (P1) films (n=7).

This odd fringe deformation is accounted quite rapidly at 27 sec (1.3 shearing cycles; 94.2 µm of distance sheared), indicating a relatively fast growth of aggregates. As shear is further prolonged, more significant deformation of the odd fringe is observed (Fig. 3.2, bottom panel) suggesting coalescence of aggregates into even bigger agglomerates, accompanied by a slower film thickening (Fig. 3.1) till a plateau in film thickness is reached after circa 40 min of shear.

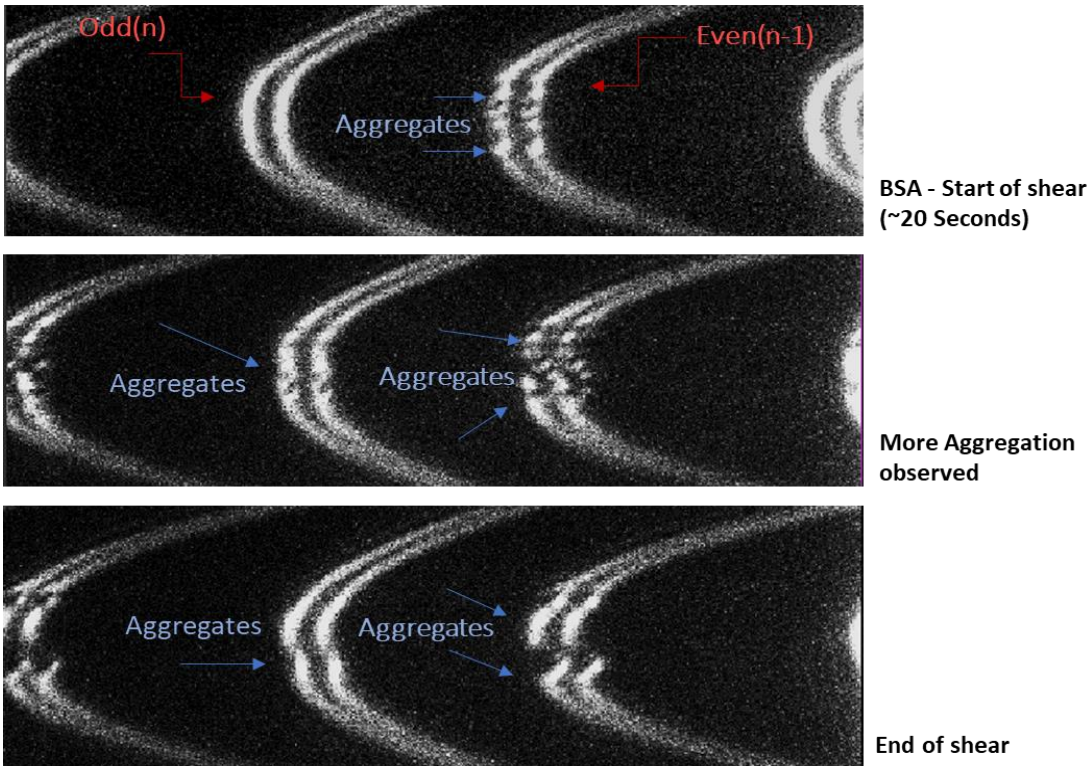

Figure 3.2 Representative FECO pattern observed for BSA only, P1 films (start, middle and end of shear).

3.1.2 Evolution of aggregates' formation of BSA+$FN_{0.02}$ films (P2)

Figure 3.3 and Fig. 3.4 show the evolution of film thickness and FECO pattern respectively for '$BSA{+}FN_{0.02}$' (P2) films, when subjected to the same shearing conditions. Figure 3.3 indicates that P2 films also abruptly thicken with time ($\Delta D_{BSA+FN(0.02)} = 56.4 \pm 11.4$ nm), however, unlike 'BSA only' P1 films, their thickness reaches a maximum after circa 20 min and starts decreasing slowly with time as shear is prolonged. As shown in the FECO of Figure 3.4, the aggregate formation in P2 films follows a similar pattern to that of P1 films, but on a different time scale. Although aggregates form almost simultaneously with the start of shear, that is after 0.97 shearing cycle (Fig. 3.4, top panel), the odd fringe deformation (Fig. 3.4, middle panel) occurs only after circa 7 min (corresponding to 26.3 shearing cycles and 1840.5 µm of distance sheared), indicating that aggregates do not grow as fast as in P1 films. Towards the end of shear, merging of aggregates into bigger agglomerates occurs, as indicated by both a greater deformation of even fringes and onset of deformation of odd fringes (Fig. 3.4, bottom panel). Note that, during shear, aggregates were also observed far from the center of the contact (marked by yellow dotted arrows on the FECO of Fig. 3.4 middle panel), suggesting that they were likely able to roll out of shearing junction (more details about aggregates' mobility in Section 3.5).

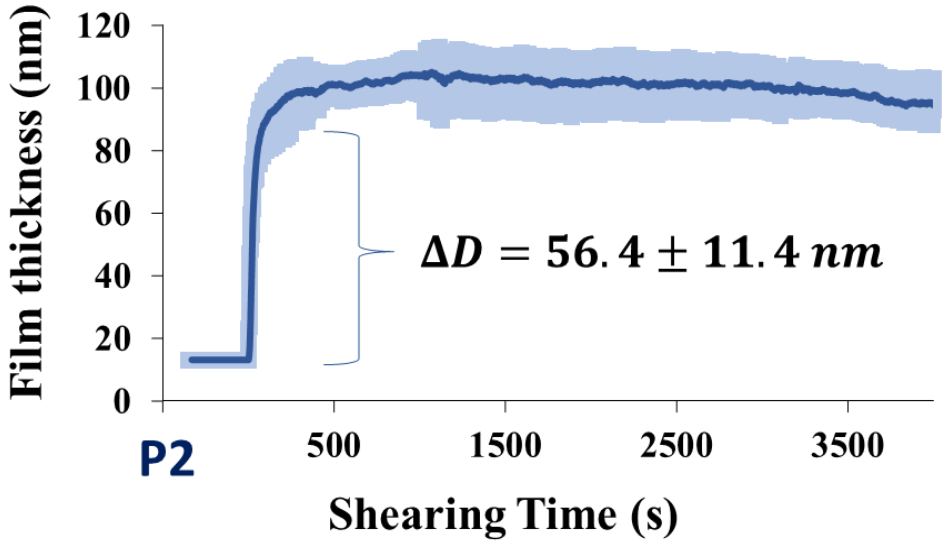

Figure 3.3 Evolution of average film thickness vs. time of shearing for "BSA+FN (0.02)" (P2) films (n = 6).

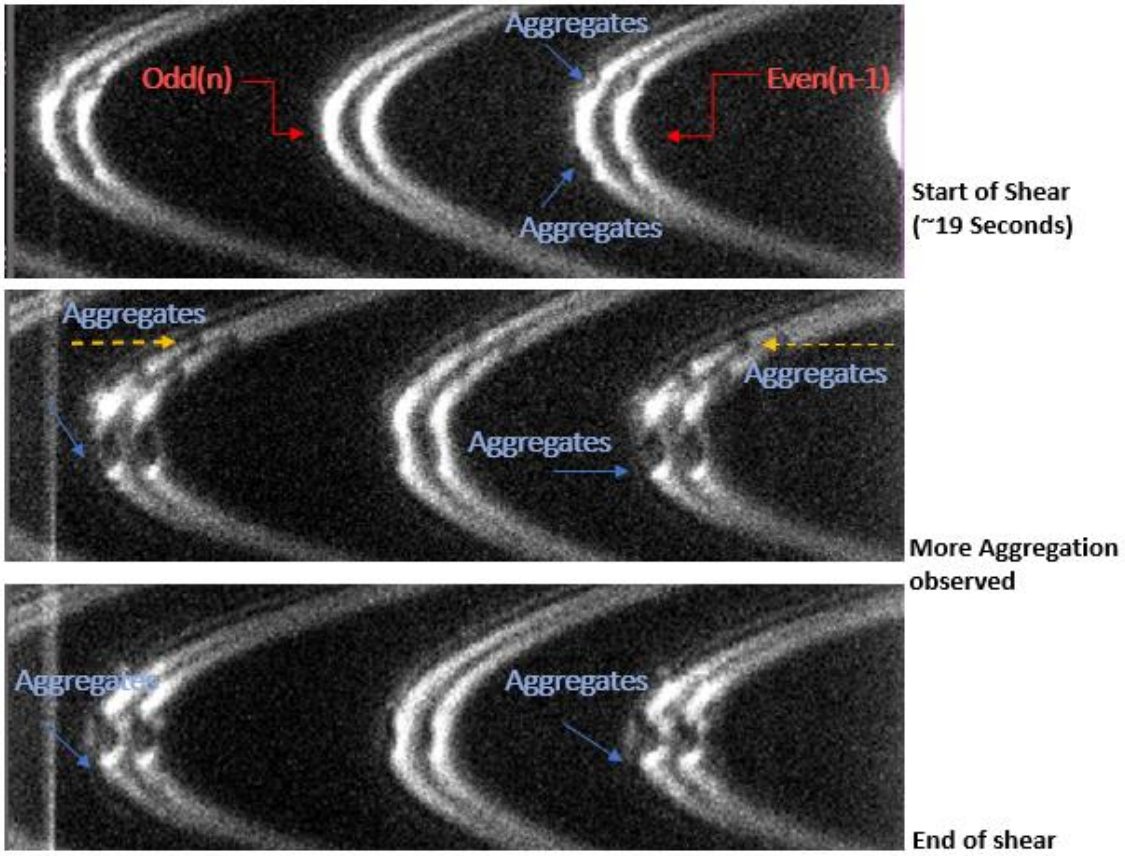

Figure 3.4 Representative FECO pattern observed for BSA+FN (0.02) P2 films (start, middle and end of shear).

3.1.3 Evolution of aggregates' formation of BSA+FN$_{0.02}$ films (P2-P)

Figure 3.5 and Fig. 3.6 show the evolution of film thickness and associated FECO pattern when '$BSA{+}FN^{P}_{0.02}$ with BSA passivation' (P2-P) films were subjected to shear. As seen in Fig. 3.5, P2-P films exhibit a greater initial abrupt thickening ($\Delta D_{BSA+FN(0.02)\,w/\,P} = 81.25 \pm 10.56\,nm$) than P1 and P2 films, then their overall thickness follows the same trend for P2 films: a quick increase ending in a plateau. The dynamics of aggregates formation was different too. Aggregates would form readily after 10 sec (Fig 3.6, top panel), multiple ripples on the even fringe accompanied by deformation of the odd fringe (Fig 3.6, middle panel) occurred at 13 seconds of shearing, illustrating a growth of aggregates faster than in P2 films. The magnitude of deformation of the odd fringe was similar to that of P3-P films discussed later. Towards the end of the experiment (Fig 3.6, bottom panel) both odd and even fringes exhibited faint ripples at their lower half, suggesting that bigger aggregates initiated at the middle were moving towards the edge of the junction.

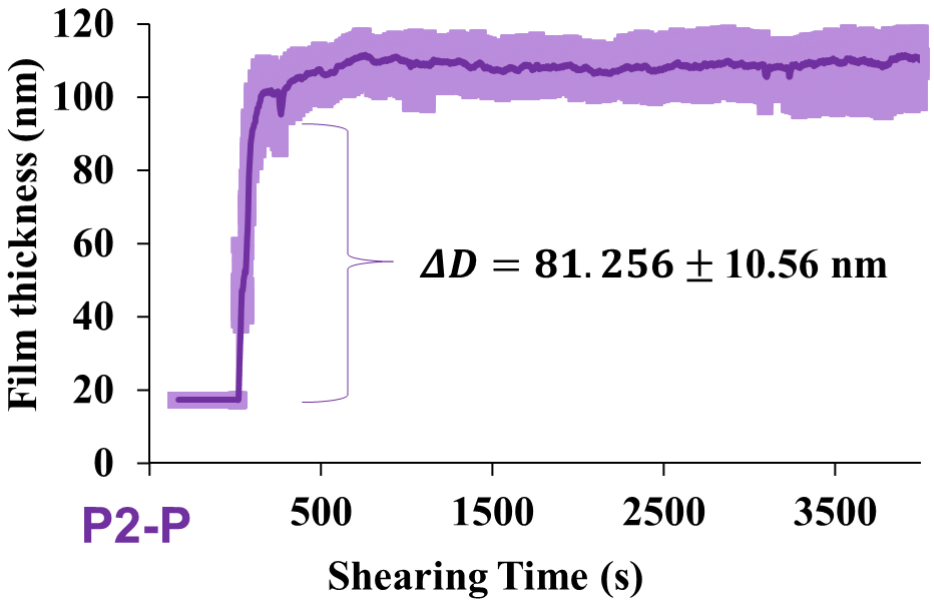

Figure 3.5 Evolution of average film thickness vs. time of shearing for "BSA+FN (0.02) w/ passivation" (P2-P) film (n=2).

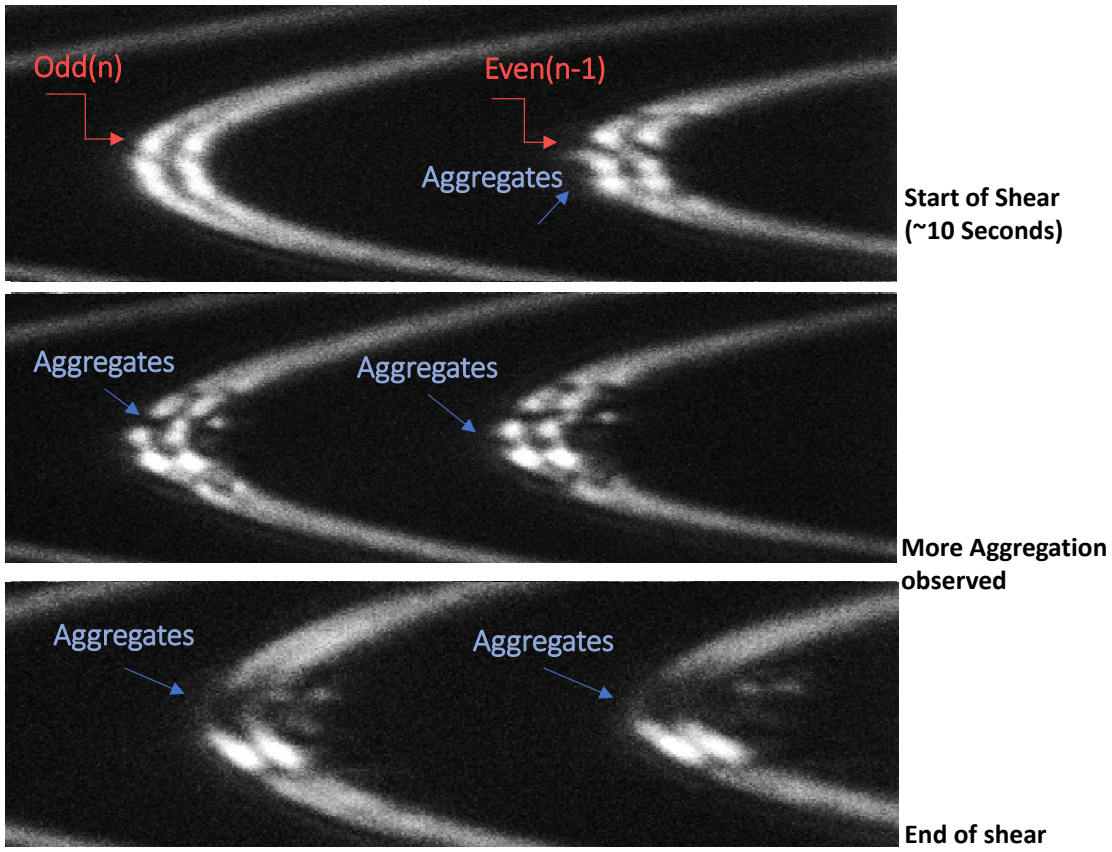

Figure 3.6 Representative FECO pattern observed for BSA+FN (0.02) w/ passivation P2-P films (start, middle and end of shear).

.

3.1.4 Evolution of aggregates' formation of BSA+FN$_{0.3}$ without passivation (P3)

Figure 3.7 and Fig. 3.8 show the evolution of film thickness and associated FECO pattern when '$BSA{+}FN_{0.3}$ without passivation' (P3) films were subjected to shear. As seen in Fig. 3.7, P3 films exhibit a greater initial abrupt thickening ($\Delta D_{BSA+FN(0.3)\ w/o\ P} = 66.2 \pm 4.3\ nm$) than P1 and P2 films, then their overall thickness follows the same trend than for P2 films: a slow increase ending in a plateau. The dynamics of aggregates formation was different too. Aggregates would form readily after only 20 sec (Fig 3.8, top panel), however, multiple ripples on the even fringe accompanied by deformation of the odd fringe (Fig 3.8, middle panel) occurred only after 15 min (27.5 shearing cycles; 1928.6 µm of distance sheared), illustrating a growth of aggregates even slower than in P2 films. The magnitude of deformation of the odd fringe was similar to that of P1 films, indicating similar size of aggregates. Towards the end of the experiment (Fig 3.8, bottom panel) both odd and even fringes exhibited faint ripples at their lower half, suggesting that many aggregates were likely pushed out of the sheared junction rather than growing bigger within the contact, which would have obstructed the light path as in the case of P1 and P2 films.

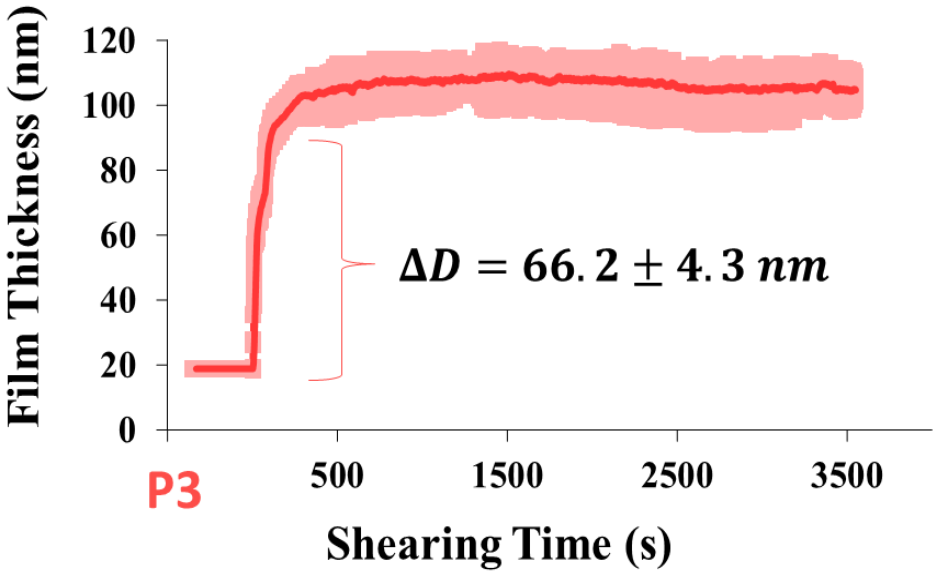

Figure 3.7 Evolution of average film thickness vs. time of shearing for "BSA+FN (0.3) w/o passivation" (P3) films (n=5).

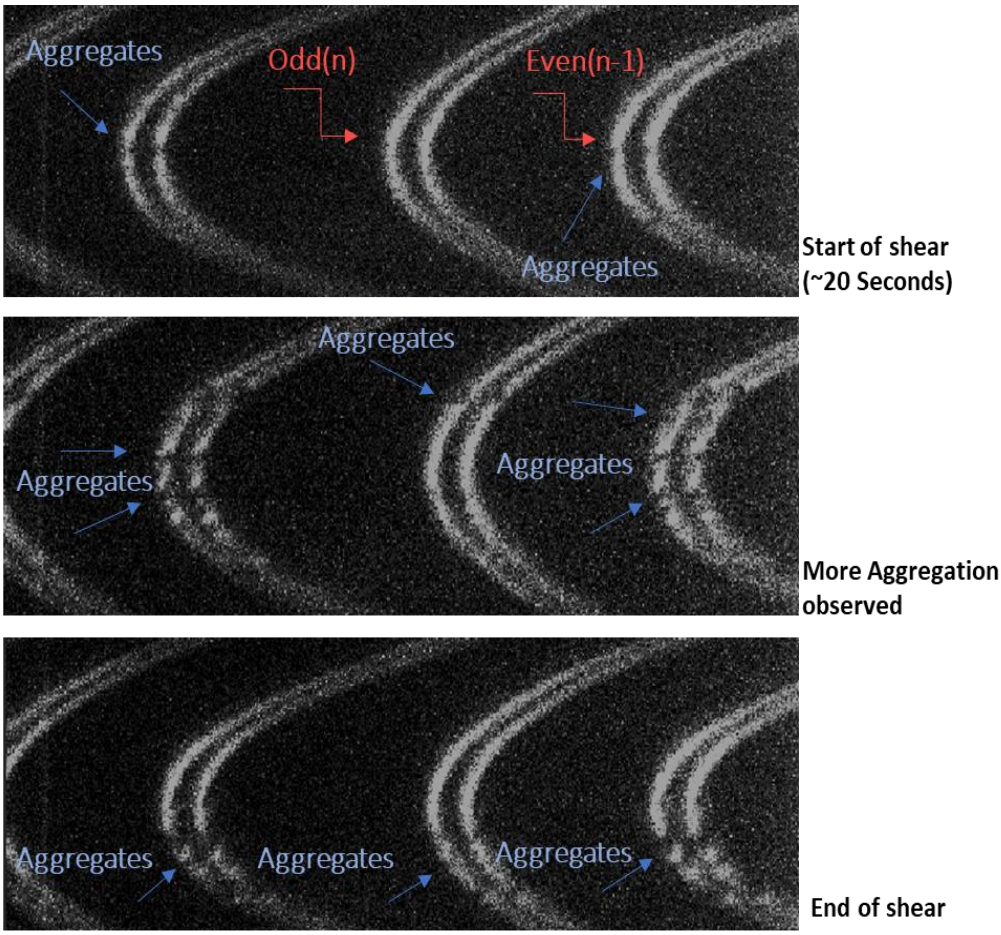

Figure 3.8 Representative FECO pattern observed for BSA+FN (0.3) w/o passivation P3 films (start, middle and end of shear).

3.1.5 Evolution of aggregates' formation of BSA+FN$^{P}_{0.3}$ with BSA passivation (P3-P)

Finally, Fig. 3.9 and Fig. 3.10 show respective film thickness and FECO pattern evolution for '$BSA+FN^{P}_{0.3}$' (P3-P) films under shear. Although Figure 3.9 "looks like" Figure 3.1, the magnitude of initial thickening for P3-P films ($\Delta D_{BSA+FN(0.3)P} = 190 \pm 19.8\, nm$) was nearly four times greater compared to P1 (and all other) films. The dynamics of aggregation was also different: the occurrence of the first aggregates (Figure 3.10, top panel) was observed quasi instantly at the beginning of shear, namely after 9 sec (0.4 shearing cycle, sheared distance of 30.5 µm), which was even faster than in P1 films. Odd fringe deformation followed after only 12 sec (0.6 shearing cycles, sheared distance of 45.3 µm) and both even and odd fringes were dramatically affected at the end of the first shearing cycle (Fig 3.10 middle panel). Upon further shear, FECO showed even deeper alterations, which indicates not only that bigger aggregates had formed but also that they had started moving from the middle to the edges of the junction (Fig. 3.10, bottom panels).

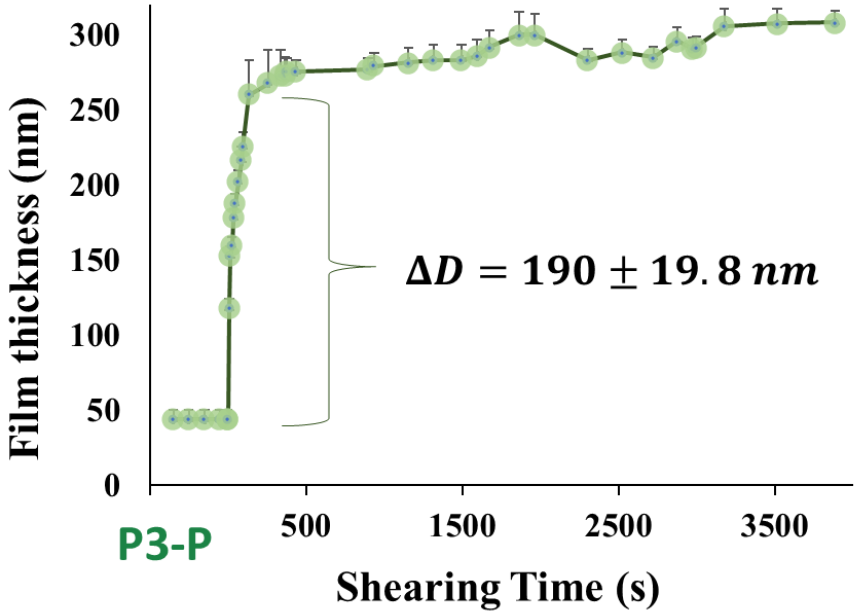

Figure 3.9 Evolution of average film thickness vs. time of shearing for "BSA+FN (0.3) w/ passivation film" (P3-P) films (n = 5).

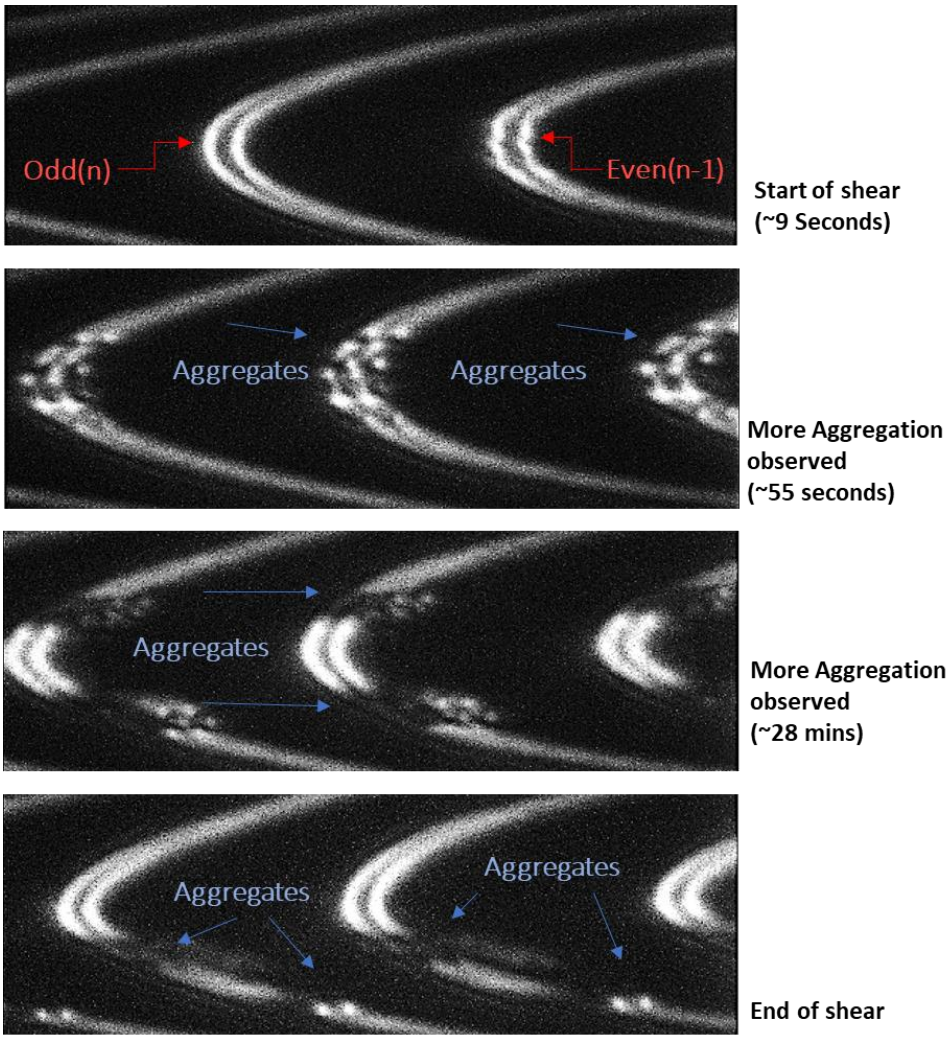

Figure 3.10 Representative FECO pattern observed for BSA+FN (0.3) w/ passivation P3-P films (start, middle and end of shear).

3.2 Structural and morphological properties of aggregates

3.2.1 Aggregates' size and distribution

Along with monitoring the dynamics of aggregates' formation, FECO also allow us to estimate their average size. To do so, we used two different approaches. Our first method relied upon normal force measurements performed both before and after each shearing experiment to compare force profiles before and after aggregate formation in the films. As detailed in Chapter 2 section 2.4, from a force profile, we can extract the 'onset of repulsion'

between surfaces, namely the separation distance between surfaces prior to compression, which is directly related either to the thickness of the uncompressed film (before shear) or to the cumulative thickness of film + aggregates present (after shear). Our second approach was to record a series of FECO snapshots after shear, using a scanning prism to visualize various cross sections of the shearing junction, as explained in Chapter 2 section 2.7. This method enabled to quantify both the size of individual aggregates but also to estimate their distribution through the entire sheared junction.

3.2.1.1 First approach: Quantifying aggregates' size via force profiles

Normal force runs were systematically carried out on all films before every experiment to extract their initial thickness, D_0, namely the thickness of each film prior to compression and shear. A representative force-distance profile measured on P1 films is shown in Chapter 2 Figure 2.6 and similar profiles were acquired on all films in order to estimate the onset of interaction between surfaces, in each case.

Figure 3.11 displays a summary of all D_0 values extracted from those measurements. While P1, P2, P2-P and P3 films had similar thickness ($22.3 \pm 4.2\ nm$, $26.8 \pm 1.3\ nm$,

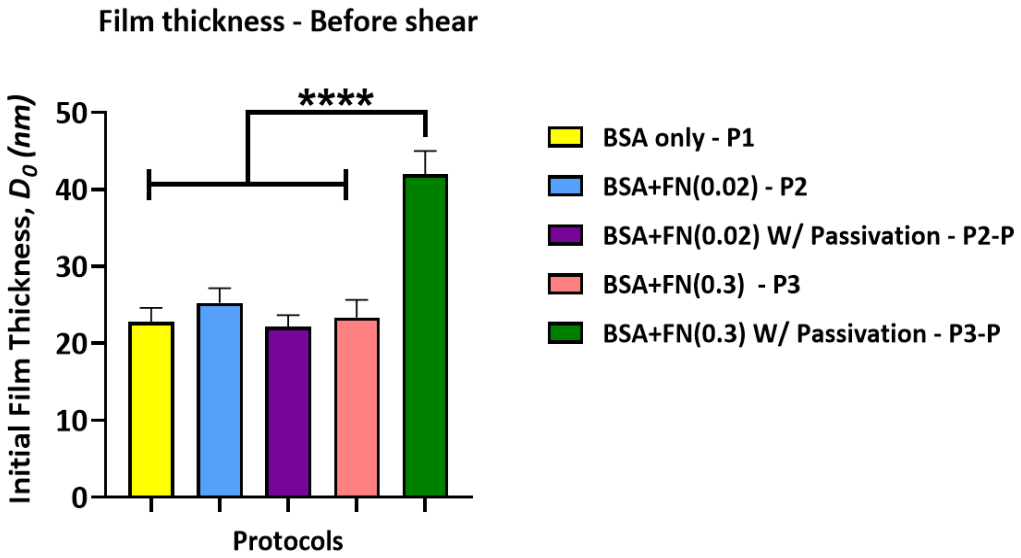

*Figure 3.11 Average value of film thickness before shear, D_0 (measured from force profile's onset of repulsion). n=7 for P1, n=6 for P2, n= 2 for P2-P, n=5 for P3 and n=5 for P3-P); P value < 0.0001 is indicated by ****.*

$22.12 \pm 1.5\ nm$, $24.2 \pm 1.8\ nm$, respectively), P3-P films were nearly twice as thick ($40.2 \pm 6.5\ nm$). Since P2 and P3 have different FN concentrations, these results indicate that FN does not have a linear effect on film thickness. Additionally, since P3 and P3-P had different BSA passivation during preparation, these results also suggest that denaturation and/or molecular exchange likely occur at the surfaces prior to start shearing. However, low FN concentration P2 and P2-P films also had different BSA passivation but show no difference in film thickness, suggesting that passivation might be concentration-dependant.

Following shear, surfaces were separated, and new normal force measurements were performed (at the same location), after the films were left at rest for 20 minutes. Figure 3.12 displays a summary of all *D* values measured, which now correspond to the cumulative thickness of the sheared film together with its sheared-induced aggregates. Note that the onset of interactions values reported here tend to characterize the largest aggregates present between the surfaces (since they are the 'first' ones interacting with the opposing surface). The trend after shear was significantly different: P1 and P3 films exhibited similar thickness ($180.0 \pm 9.9\ nm$ and $184.0 \pm 16.7\ nm$, respectively), while P2 films and P2-P were circa 28% thicker

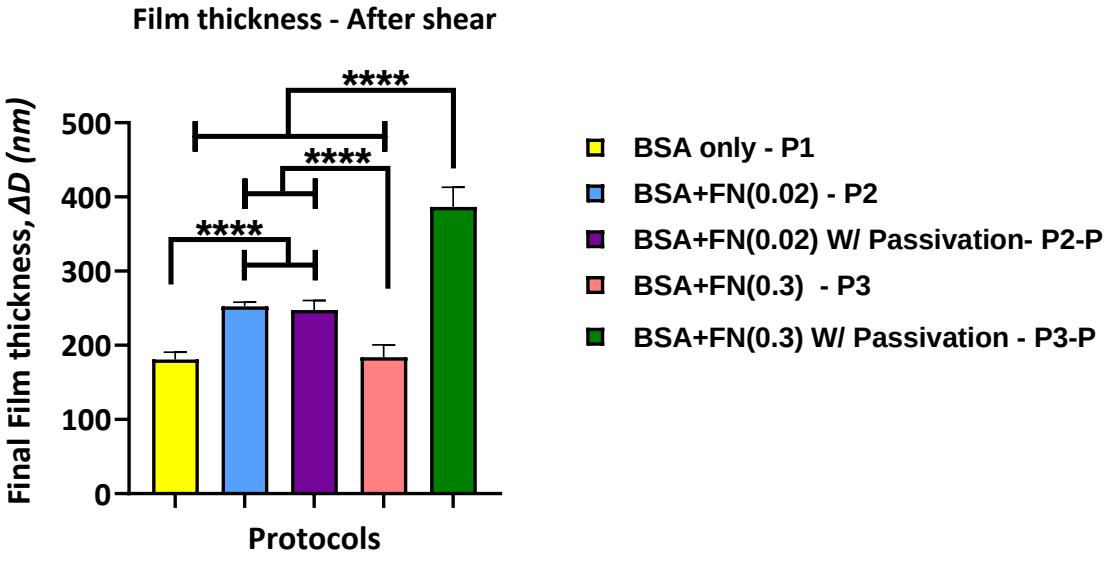

*Figure 3.12 Average value of film thickness after shear, D (measured from force profile's onset of repulsion). (n=7 for P1, n=6 for P2, n= 2 for P2-P, n=4 for P3 and n=3 for P3-P). P value < 0.0001 is indicated by ****.*

($252.2 \pm 5.7\ nm$, $247.42 \pm 12.92\ nm$) and P3-P films, again, were more than twice as thick ($386.5 \pm 26.58\ nm$) as P1 and P3 films. These results confirm that, although shear promotes the formation of SA aggregates in all films, their resulting size (or at least the average size of the largest aggregates formed) largely depends on the presence of FN and/or on the surface passivation process of the surfaces prior to shear, with small aggregates present in P1 and P3 films and significantly larger aggregates (likely composed of merged small aggregates, as mentioned previously in Section 3.1) present in P2 , P2-P and P3-P films. The respective roles of FN concentrations to anchor SA at the surfaces and BSA passivation to prevent nonspecific interactions between FN and SA prior to shear on aggregates size are discussed at length in Chapter 4, Section 4.3.

3.2.1.2 Second approach: Quantifying aggregates' size and distribution via FECO cross sections of the sheared junction

To validate the results obtained in Section 3.2.1.1, we used a second (independent and complementary) approach to assess not only aggregate dimensions but also size distribution. Briefly, we used a prism to scan through the sheared junction by acquiring FECO snapshots of multiple cross sections to capture all the events that were missed out during normal force measurements. In such a way, we could image via FECO the entire sheared junction rather than just the middle section of the contact (as usually done during force profile), and we could assess the average size of all aggregates present in the junction rather than only the largest ones (as estimated from force profiles).

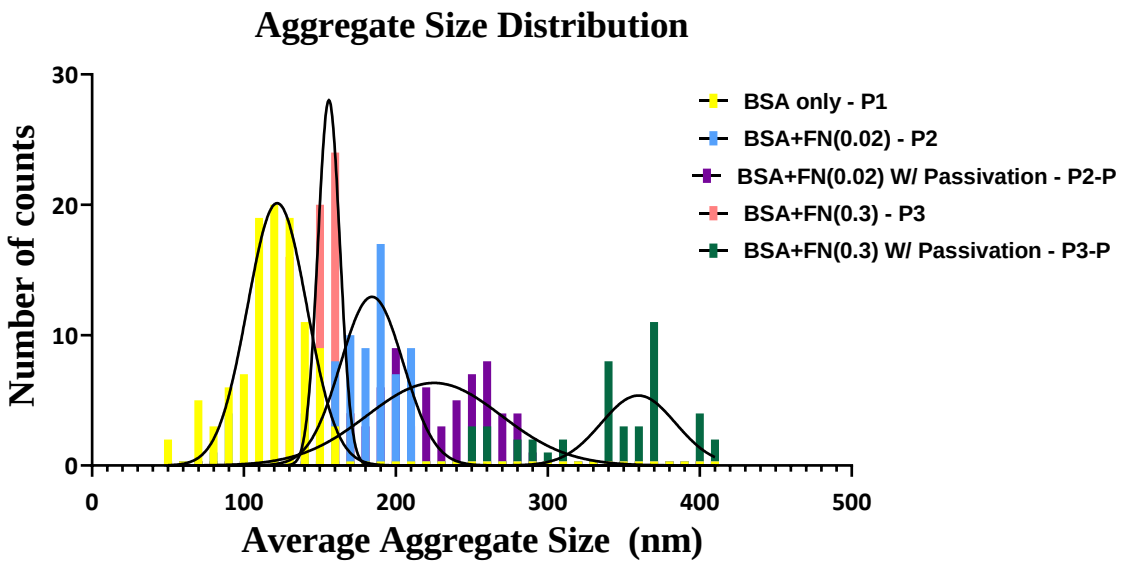

Figure 3.13 Distribution graph showing the average counts of aggregates occurring vs average aggregate size for each of the protocol indicated by distributive histogram fitted with a non-linear regression fit and a bin size of 10 nm (n=106 for P1, n=71 for P2, n=66 for P2-P, n= 66 for P3, n= 45 for P3-P.

As all details of our calculation and analysis of single aggregates size can be found in Chapter 2 section 2.7, Fig. 3.13 summarizes the distribution of aggregates size, obtained for all films. In each case, distribution function was carried out with a bin size of 10 nm for the average size of each aggregate. The distributive histogram was then fitted with a non-linear Gaussian regression fit. This allowed us to determine the best fit values that in turn aided in the extraction of average individual aggregate size and distribution of aggregates. Mean and standard deviation of each distribution were as follows: P1 films contained the smallest aggregates ($121.9 \pm 19.5\, nm$), followed by P3 films ($155.9 \pm 7.2\, nm$) , P2 films ($184.3 \pm 20.6\, nm$) and P2-P films $224.23 \pm 35.79\, nm$), while P3-P films exhibited the largest aggregates ($359.6 \pm 24.4\, nm$). Although the standard deviation was rather large in P1, P2 and P2-P cases, indicating a broad range of sizes for aggregates within the films, it was extremely narrow in P3 films, suggesting the presence of much more uniform aggregates. The case of P3-P films was different, as shown by the poor quality of the Gaussian regression (a large amount of data fell 'outside' the fit), which was due not only to the extremely large

distribution of aggregates but also to the smaller number of aggregates present in P3-P films, compared to the other ones. Overall, these data validate the results from Section 3.2.1.1 and add important information regarding the size distribution and the average number of aggregates (as indicated by *n* in the caption of Fig. 3.13) present in each film. These findings are discussed in Chapter 4, Section 4.3.

3.2.2 Aggregates' shape, merging and alignment during shear.

To assess aggregates' shape, we also captured pictures of the full Newton rings patterns after each shearing experiment. As we systematically observed that, under shear, SA films gradually thickened and started forming aggregates in the films, we next asked whether those aggregates (of different size and distribution) had also different shape and if they were randomly distributed in the sheared junction. By capturing and analyzing Newton rings we could estimate the shape of aggregates (or agglomerates made of merged aggregates) and localize them in the shearing junction, in order to monitor their tendency to merge with each other and to align (or not) in a specific direction (with respect to the shearing direction).

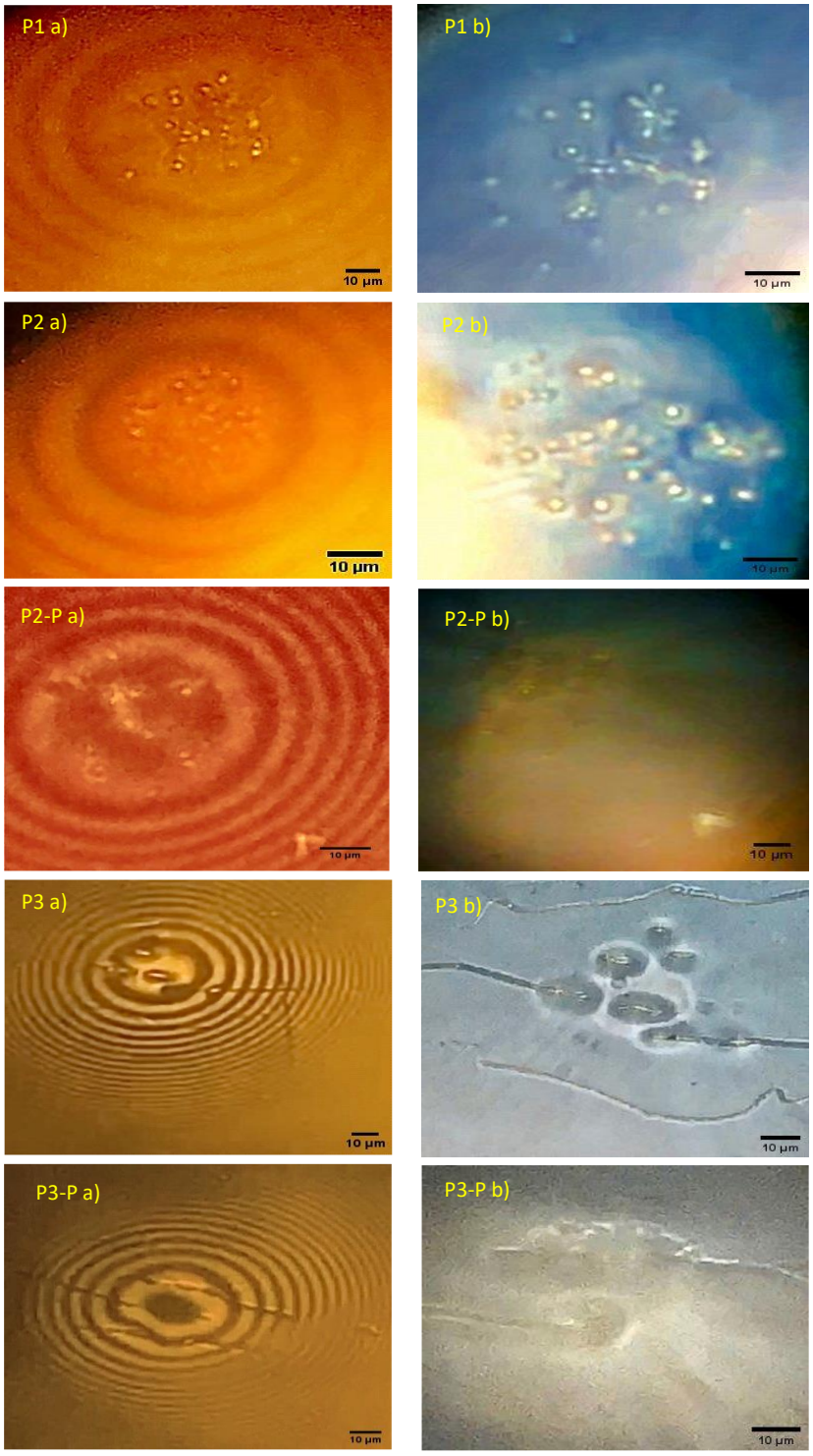

Figure 3.14 Shape and alignment of aggregates in P1, P2, P2-P, P3, P3-P films, as measured right after shear; (a) Newton rings recorded through a narrow bandpass yellow/orange filter of the sheared area, (b) magnified versions of the same area recorded without filter.

Figure 3.14 displays a summary of all Newton rings patterns recorded right after shearing each film, left panels were recorded through a narrow bandpass yellow/orange filter for better visualization of the rings using white light, right panels were magnified versions of the left panels recorded without any filter. P1 and P2 films showcased the presence of well-defined rounded aggregates, randomly distributed everywhere in the contact junction.

P2-P showed rounded aggregates as well but were not as defined as seen in P2 and were also randomly distributed across the junction. Instead, P3 films showed some sort of strings of aggregates, resulting in fewer though larger rod-like shaped agglomerates, Interestingly, the magnified version of P3 rings indicated more strings located at the top and bottom edge of the contact junction, suggesting that those aggregates were expelled from junction (when subjected to high compressive force). Similarly, P3-P films contained string-like aggregates coalesced together. Significantly longer than in the case of P3 films, theses aggregates extended far beyond the sheared region. In both P3 and P P3-P films, aggregate "strings" tended to orient roughly 45° with respect to the shear direction (horizontal direction in all panels of Fig. 3.14. These results are in agreement with previously published studies[5].

3.2.3 Aggregates' density assessed via refractive index (RI) measurements

As explained in detail in Chapter 2 Section 2.3, the SFA-FECO technique also allows for refractive index (RI) measurements to be performed in the films under confinement and shear, by investigating specifically the position of even fringes patterns. Although the resolution of RI measurements is significantly lower than that of thickness measurements presented earlier, we decided to monitor and analyze RI as well, as it provides valuable indirect information regarding the density of the medium (here the fluid and its aggregates). Briefly, we focused our analysis onto three independent sections: (i) RI of films before shear, (ii) RI of films during shear (regions without aggregates), (iii) RI of aggregates (during shear as well). In all cases, the FECO sections analyzed were randomly chosen in the contacting junction to ensure average properties. Our data are summarized in Figure 3.15 for P1, P2, P2-P, P3 and P3-P films. The first noticeable feature is that, in the cases of P1 and P2 films, there was no major difference in IR values before and after shear, indicating no major (detectable) variations in film density through the whole shearing process. Instead, in P2-P, P3 and P3-P films, the IR of aggregates were significantly larger, suggesting local alterations in density

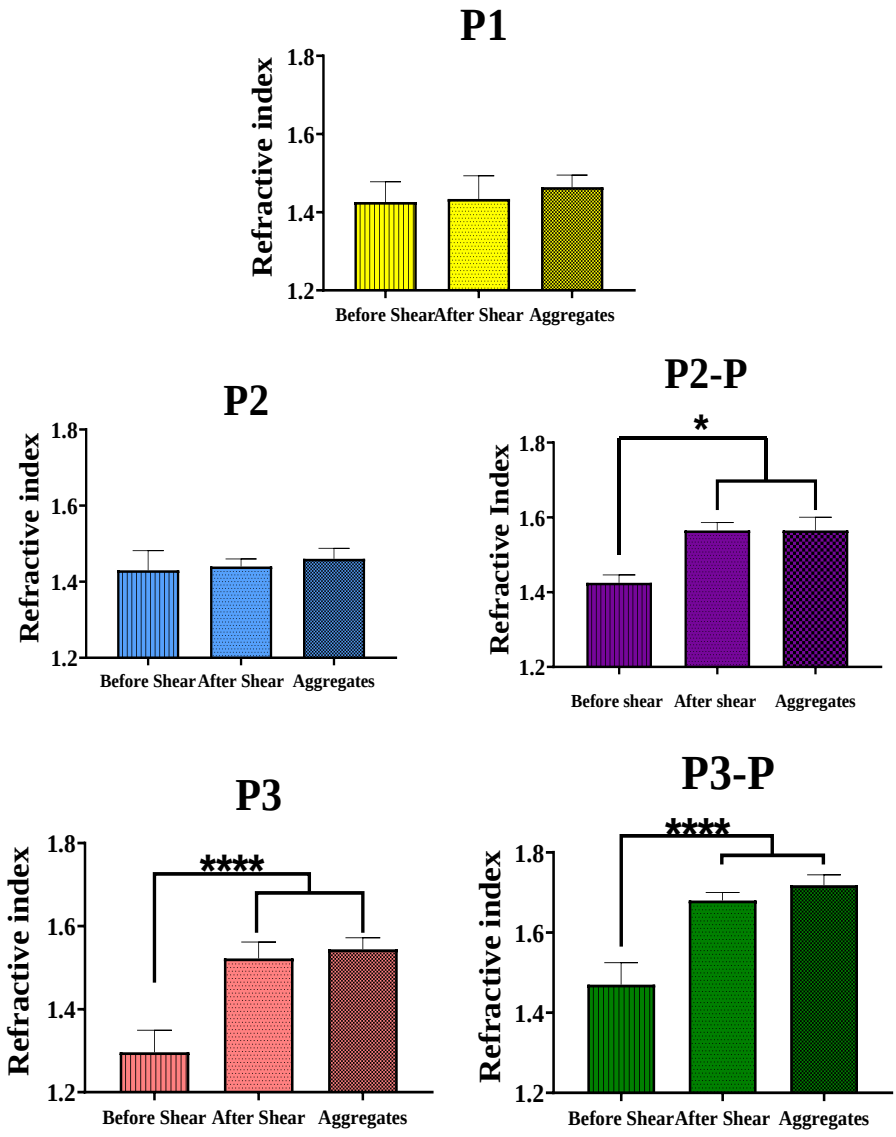

*Figure 3.15 Refractive Index (RI) calculation for each film; before shear, after shear and with aggregates. P1 films: RI mean BS = 1.42 ± 0.05; RI mean AS = 1.43 ±0.05; RI mean Agg = 1.46 ± 0.03; n=7; P2 films: RI mean BS = 1.43 ± 0.05; RI mean AS = 1.44 ±0.01; RI mean Agg = 1.46 ± 0.02; n=6; P2-P films : RI means BS = 1.56 ± 0.03; RI mean AS = 1.66 ±0.02; RI mean Agg = 1.67 ± 0.03; P3 films: RI mean BS = 1.29 ± 0.05; RI mean AS = 1.52 ±0.03; RI mean Agg = 1.54 ± 0.02; n=5; P3-P films: RI mean BS = 1.47 ± 0.05; RI mean AS = 1.68 ±0.02; RI mean Agg = 1.71 ± 0.02. P values < 0.01 are indicated by * and P values < 0.0001 are indicated by ****.*

likely related with molecular structural/conformational and/or orientational changes within the sheared films. Additionally, among all films, aggregates present in P3-P had the highest IR values, followed aggregates found in P3 films. These data suggest that, in P3 and P3-P

aggregates, molecular density was significantly higher than in P1 and P2 ones, due to tighter packing of molecules that might be associated with (partial of full) denaturation and unfolding. P2-P also shows significance in density higher than P1 and P2 but lower than P3 and P3-P. These interesting findings and their correlation with the mechanical properties presented below in Section 3.4 are discussed in Section 4.5.

3.3 Stability of aggregates

Next, we assessed the longevity of aggregates, as an indication of their stability over time. Importantly, we asked whether the aggregation process was temporary (reversible) or permanent (irreversible), and if such process depended on the presence of FN. Figure 3.14 summarizes our method to quantify aggregates' longevity: Newton rings were first recorded right after shear, the surfaces were then separated and kept circa 1 mm apart for 24 hours

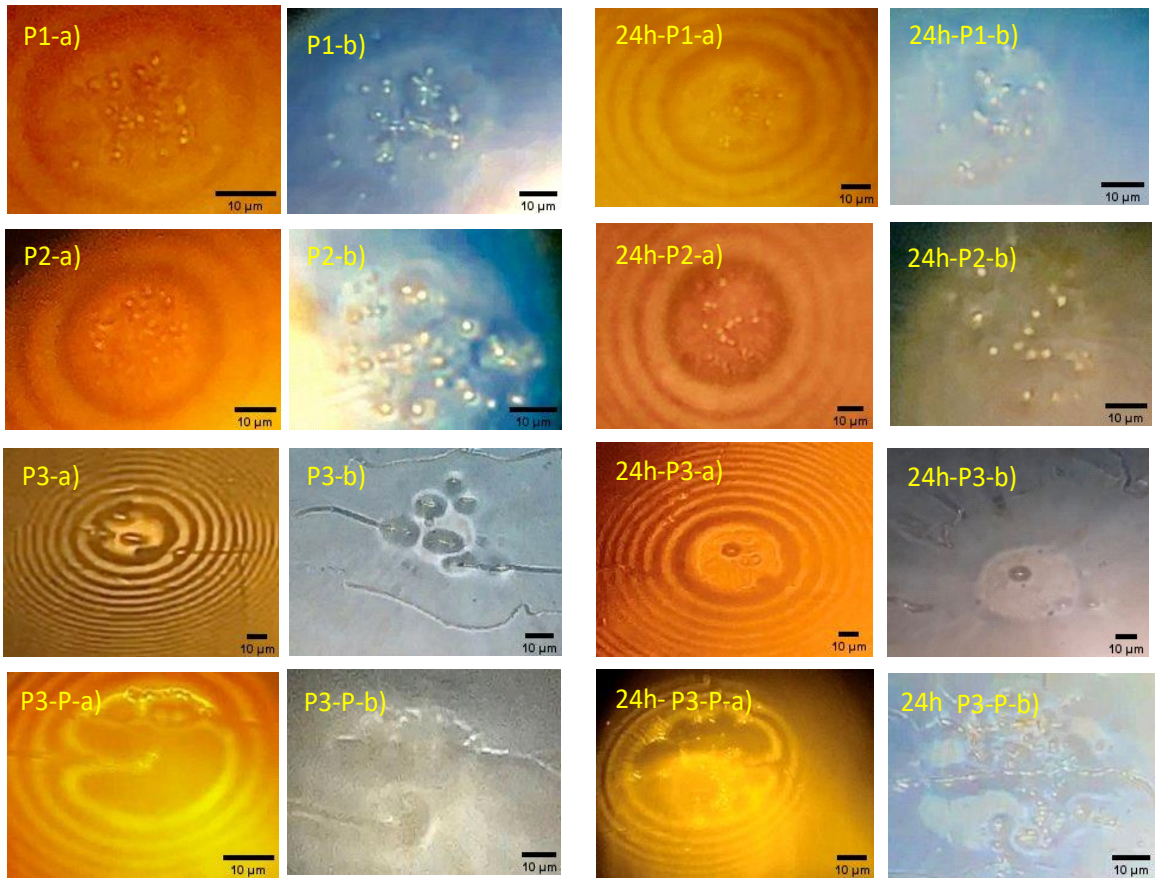

Figure 3.16 Pictures of newton rings right after shear with and without filter (a, b) and pictures of newton rings captured after 24 hours with and without filter (left to right (24h); a ,b); four protocols P1, P2, P3, P3-P (top to bottom).

(allowing for aggregates to be immersed back in a significant volume of bulk liquid SA), after 24 hours, the surfaces were brought into contact again and new Newton rings were captured for all films except for P2-P which is shown in Fig. 3.14. Overall, we were still able to find aggregates after 24 hours in all films, (observed in FECO for P2-P) which indicates that they did not dissolve (even when immersed in dilute 'free floating' SA solutions) and therefore that aggregation is an irreversible process, likely because it involves denaturation of proteins promoting their tight and strong binding to each other.

3.4 Mechanical properties of aggregates

Following structure, density, and stability, we next assessed mechanics of the shear-induced aggregates, by measuring their stiffness *in situ*. Young moduli of all aggregated films were extracted from normal force profiles (recorded post-shear) using the Johnson's contact mechanics equation. Our method and model are described at length in Chapter 2 Section 2.6. Figure 3.17 summarizes the compressive Young's moduli measured in all protocols. P1 and P2 were the most compliant films with similar low stiffness (E = 25.3±4.0 kPa (n=7) and E = 21.6±2.1 kPa (n=6), respectively). P2-P films were significantly stiffer than P2 marked by '*' (E= 48.73 ±10.89 kPa (n=2)). P3 films were significantly stiffer (E = 109.2±9.3 kPa (n=5))

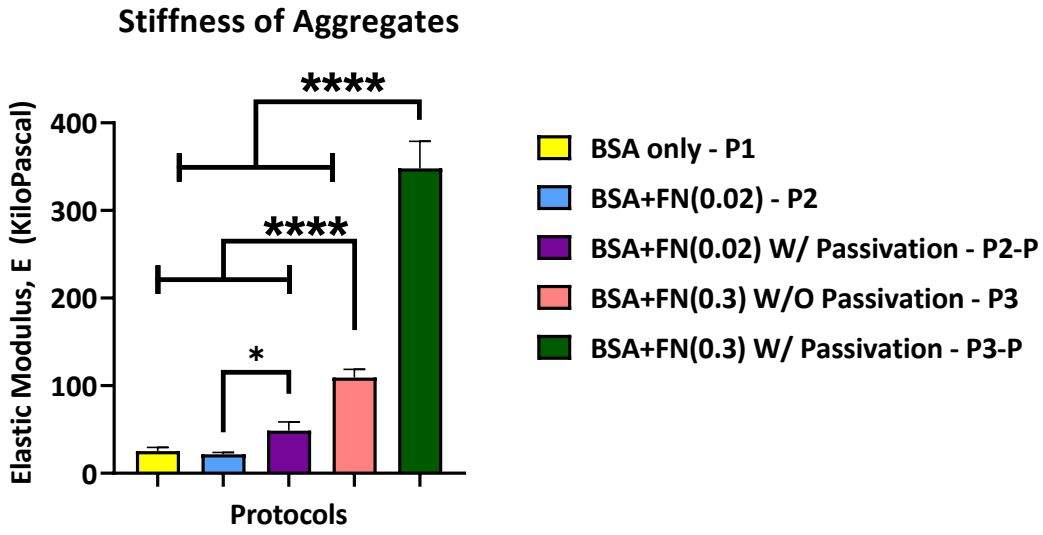

*Figure 3.17 Young's moduli measured in compression, on all four films. P values < 0.01 are indicated by * and P values < 0.0001 are indicated by ****.*

than P1 and P2 and P2-P films. Remarkably, P3-P films were the stiffest of all films (E = 348±22.7 kPa (n=3)), with a Young's modulus exceeding three times that of P3 films and more than ten times that of P1 and P2 films. These mechanical results are consistent with the IR structural data found in Section 3.2.3, indicating a correlation between density and stiffness, with denser aggregates exhibiting stiffer properties, as expected.

3.5 Mobility of aggregates

Since our dynamics data of sections 3.1 and 3.3 indicate that aggregates were able to form, merge and align in the contacting junction, we investigated more accurately their mobility during the shear process. This study was also an attempt to distinguish the role of molecular interactions *within* aggregates (mostly SA-SA interactions) from that of molecular interactions *between* aggregates and shearing surfaces (mostly SA-FN interaction) in friction, as reported next in Section 3.7. As a measure of mobility, we evaluated the displacement of aggregates by comparing FECO snapshots of the sheared junction prior and after surface separation following shear. Namely, at the end of each shear experiment, surfaces were separated for 1 hour then brought back into contact at the same position (and similar applied load) while intensity discontinuities in the even FECO fringes were tracked to observe if aggregates had changed location in the contact (this method is explained in Chapter 2, Section 2.7).

Fig 3.18 shows representative FECO patterns recorded prior (top panel) and after (bottom panel) separation over P1 sheared films. Horizontal and vertical dashed lines have superimposed onto the FECO snapshots to facilitate the observation of aggregates displacement (if any). We notice that (i) more aggregates are visible on the bottom panel than on the top one, and (ii) the aggregates initially visible in the upper section of the FECO have moved vertically. This suggests probable displacement of the BSA aggregates, which are only weakly bound to the surfaces in absence of FN (used as an "adhering" agent in all other films). The presence of additional aggregates at the bottom section of the FECO can be explained by the higher load applied after surface separation, leading not only to a greater surface area (comprising the previously sheared zone and its surroundings) but also to some pressure-induced displacements of aggregates. Both phenomena indicate mobility of initially existing aggregates.

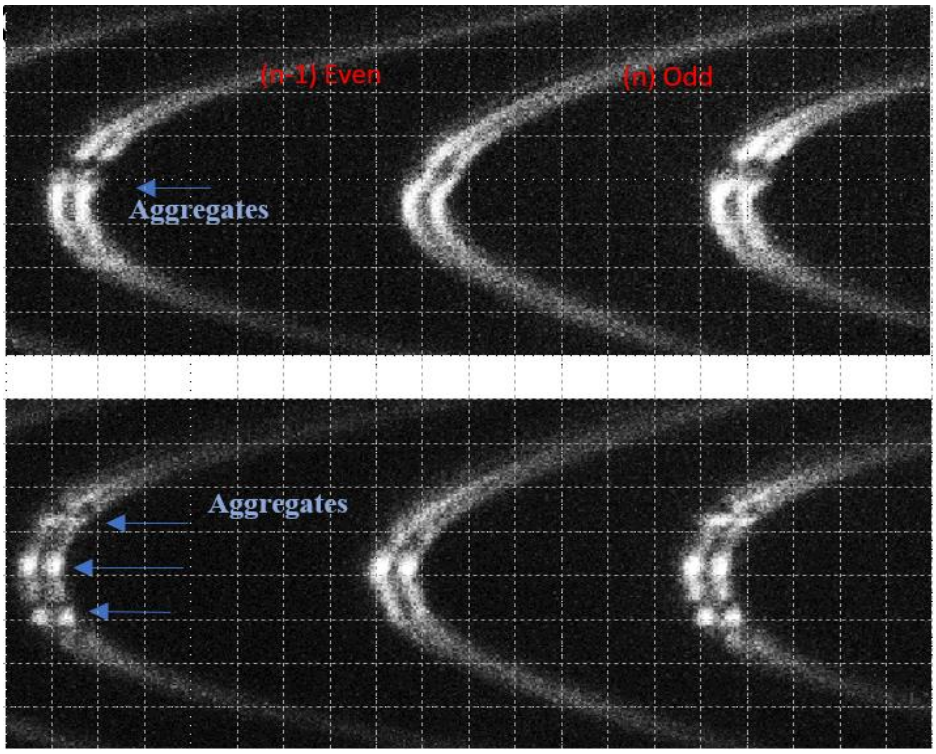

Figure 3.19 FECO snapshots of a P1 film sheared junction prior (top panel) and after (bottom panel) surface separation following shear.

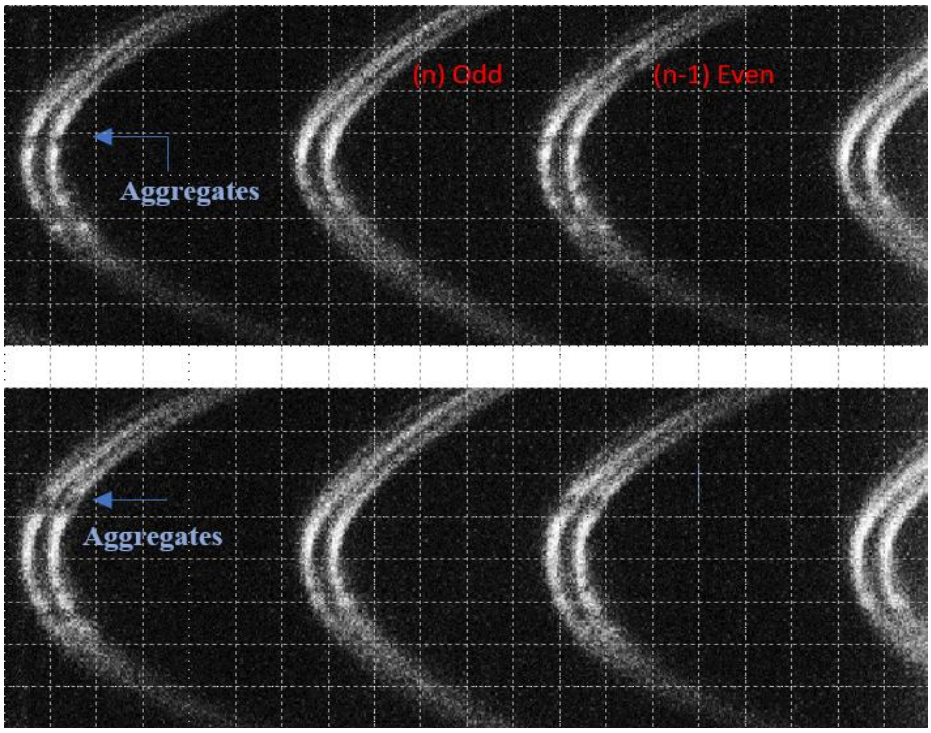

Figure 3.18 FECO snapshots of a P2 film sheared junction prior (top panel) and after (bottom panel) surface separation following shear.

The data we collected on P2 films were more pertinent, as the applied load prior and after surface separation was the same, allowing us to visualize the exact same sheared area and facilitate our analysis of displacement. Fig 3.19 shows representative FECO patterns recorded prior (top panel) and after (bottom panel) separation over P2 films. By following the blue arrow pointing at aggregates between top and bottom panels, it is clear that they had moved up by circa half cubic grid (corresponding to ~4 microns). Note that, less obvious but still detectable, the aggregates located at the bottom section of the FECO had been moved towards the bottom of the contact, indicating an overall displacement of aggregates from the center to the periphery of the junction when subjected to normal applied load/pressure.

Next we followed the same tracking method in P2-P, P3 and P3-P films, however, we could not notice any significant displacement of aggregates so we decided not to display the FECO associated with those experiments. These results suggest that the interactions between aggregates and surfaces in P3 and P3-P systems seem high enough to increase aggregate adhesion and prevent (or at least notably restrain) aggregate mobiliy between the surfaces.

Surprisingly, rather than showing aggregates mobility, P3 films exhibited another interesting systematic behavior, as observed in all normal force runs performed after shear

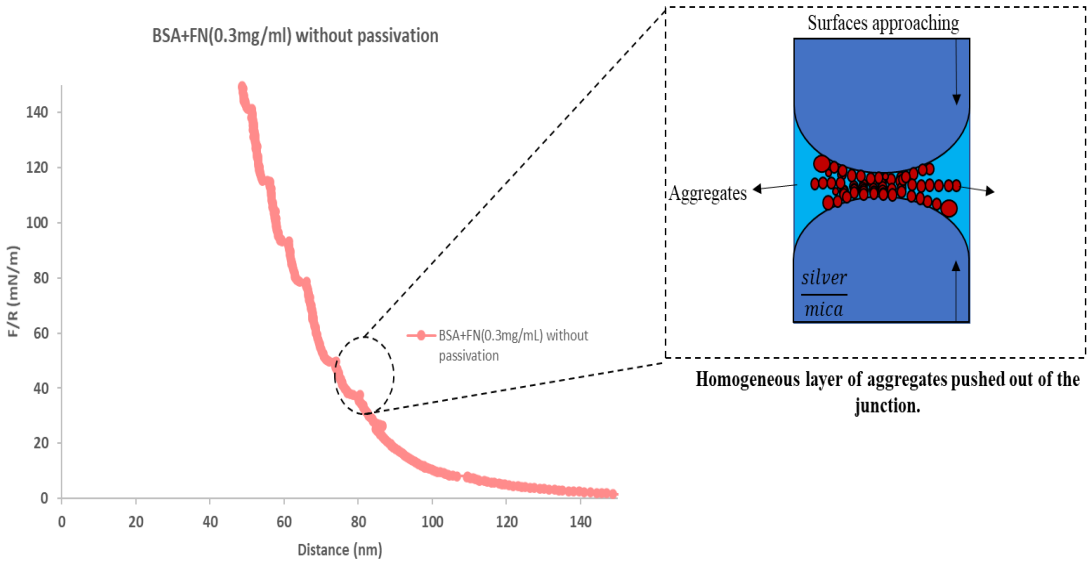

Figure 3.20 Representative normal force curve measured on P3 films, as performed following a shear experiment, and exhibiting numerous steps/jumps of similar size.

(n=5). Figure 3.20 shows one of these force runs, obtained when the surfaces were slowly brought back into contact. Small reproducible 'jumps' or otherwise referred to as "steps" were noticed, which appeared when film thickness reached circa 80 nm down to circa 50 nm when hard wall was reached. The size of these steps was analyzed in detail, as shown in Fig. 3.21

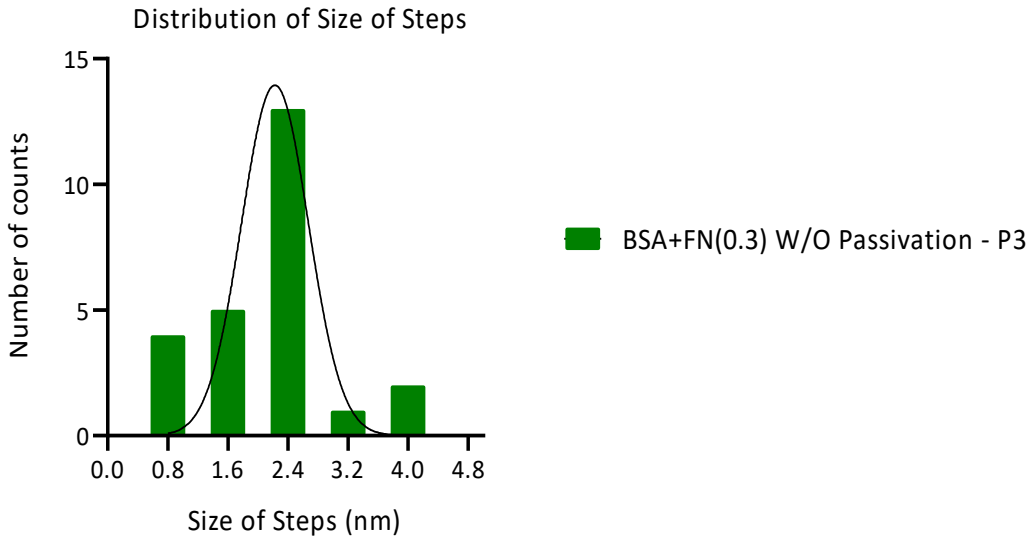

Figure 3.21 Average size of the steps/jumps detected in Fig. 3.20, plotted with a bin width of 0.8 nm and fitted to a Gaussian distribution (n = 6).

where all steps of all force runs were counted, and steps size distribution was fitted with a non-linear regression (gaussian) to extract the best fit values of mean and standard deviation. The step size was found to be $2.2 \pm 0.7\ nm$. This mean step value is particularly interesting because it could correspond to the radius of gyration of single human SA molecules ($2.7 \pm 0.3\ nm$), as estimated by A Mikhail et.al. in aqueous solutions.[6] Therefore such sequence of identical steps measured in the force runs strongly suggests shear-induced layering of albumin molecules within the junction, and sequential ejection of single SA layers (likely the layers located at the middle of the film since the external ones are strongly bound to the mica surfaces by FN) upon increased pressure, as schematized in the inset of Fig. 3.20. This peculiar behavior is further discussed in Section 4.4.2.

3.6 Friction forces and their evolution during aggregation

Friction forces were measured simultaneously to the film thickness and aggregate formation reported in Section 3.1, at all times during shear. Figure 3.22 summarizes the evolution of the friction force during time of shearing, for all films. To facilitate comparison between all conditions, the instantaneous coefficients of friction were also calculated in each case, by simply dividing the instantaneous friction force by the normal applied load (here typically around 1.5 mN) and averaged. Mean and standard deviation of both friction forces and corresponding averaged coefficients are indicated in the caption of Figure 3.22. The first interesting feature is that, although the friction forces were nearly constant in the case of P1 and P3-P films, which means friction had reached a steady state (equilibrium), they would steadily increase in P2, P2-P and P3 films, even after one hour of shear, suggesting that structural or orientational rearrangements were still occurring in the films, leading to more dissipation. The second distinct characteristic is that, although the magnitude of the friction forces varied from one film to another (from circa 0.6 mN to 0.8 mN), in average, the corresponding friction coefficients were similar on all films, namely $\mu \sim 0.5$ (with an exception for P3-P films which seemed to exhibit a slightly lower coefficient with $\mu \sim 0.4$). Here it is important to prompt that no mica surface damage was ever observed during those measurements, ensuring that all films under shear are experiencing wearless friction.

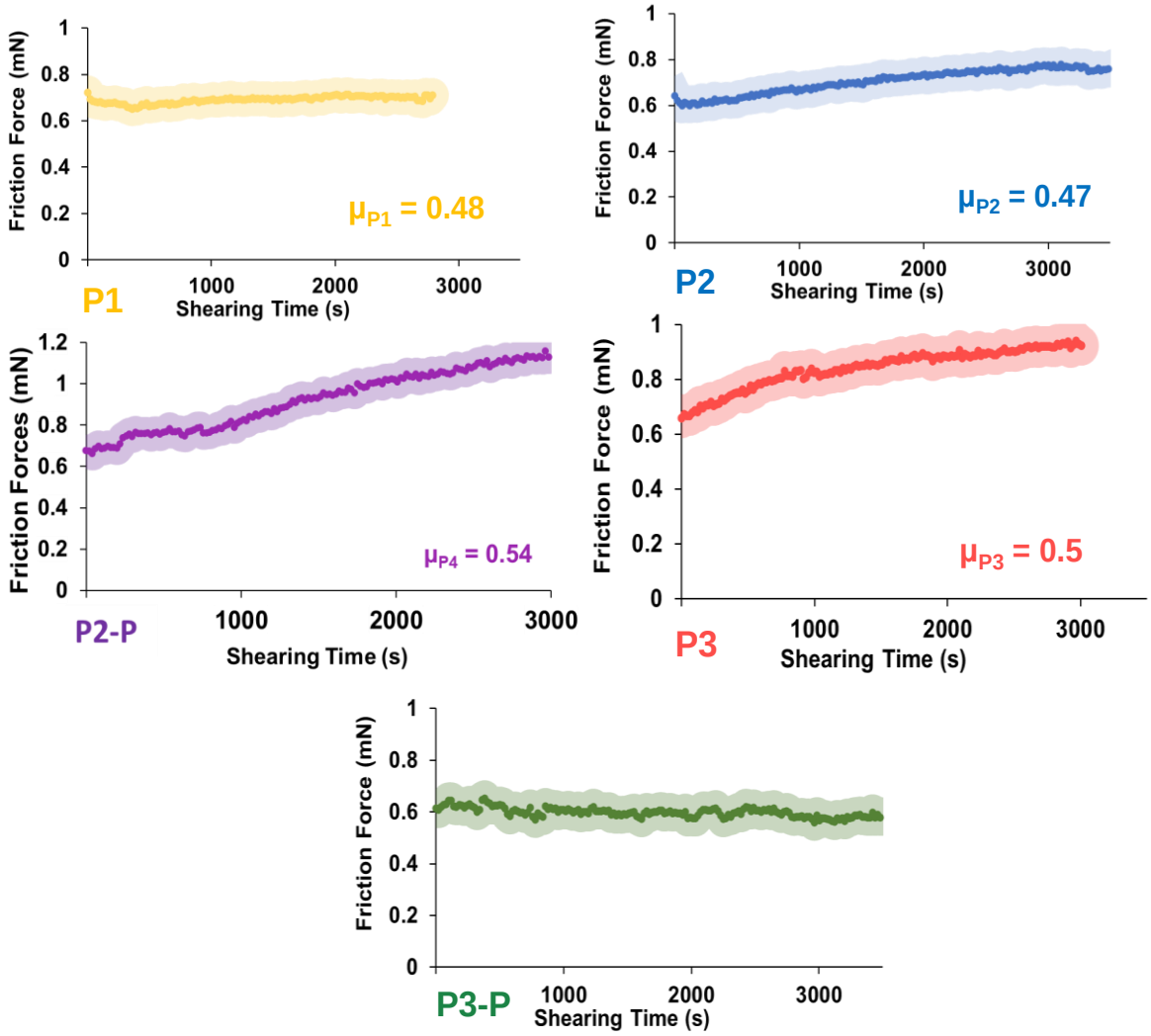

Figure 3.22 Average friction forces vs. time for P1 (avg force = $0.7 \pm 0.2\ mN$, $\mu_{P1} \approx 0.48 \pm 0.1$ *, n=7), P2 (avg Force =* $0.7 \pm 0.1\ mN$ *;* $\mu_{P2} \approx 0.47 \pm 0.04$ *; n=6) , P2-P (avg Force = 0.8 ± 0.1* mN *;* $\mu_{P2'} \approx 0.54$ *± 0.05 ; n=2) P3 (avg Force =* $0.8 \pm 0.3\ mN$ *;* $\mu_{P3} \approx 0.5 \pm 0.2$ *; n=5) , P3-P (avg Force =* $0.6 \pm 0.1\ mN$*;* $\mu_{P4} \approx 0.4 \pm 0.05$ *; n=5).*

3.7 Composition of Aggregates

Laser scanning confocal microscopy was used in complement to characterize the composition of aggregates, more specifically to understand if they comprised only BSA (shearing medium protein) or both BSA and FN (surface coating protein). To do so, BSA was labelled using Alexa-488 green fluorophores and FN was labelled using Alexa-594 red fluorophores prior to SFA shear experiments, as explained in detail in Chapter 2 section 2.8. The sheared surfaces were then unmounted and imaged via confocal microscopy, using sequential imaging of both fluorophores, as summarized in Figure 3.23. The green channel (Fig 3.23-A) displays the light collected using green laser excitation (488 nm), showing the BSA contents of aggregates (or rather agglomerates of aggregates) found at the surface. The red channel (Fig 3.23-B) displays the light collected using red laser excitation (633 nm), showing the FN contents of aggregates. Finally, the third channel (Fig 3.23-C) shows the overlay of both the green and the red channels indicating that both colors perfectly colocalized (yellowish result), and revealing that aggregates are composed of both BSA and FN molecules. This experiment was carried out for the protocol $P2$ only for the constraints mentioned in Chapter 2, section 2.8.

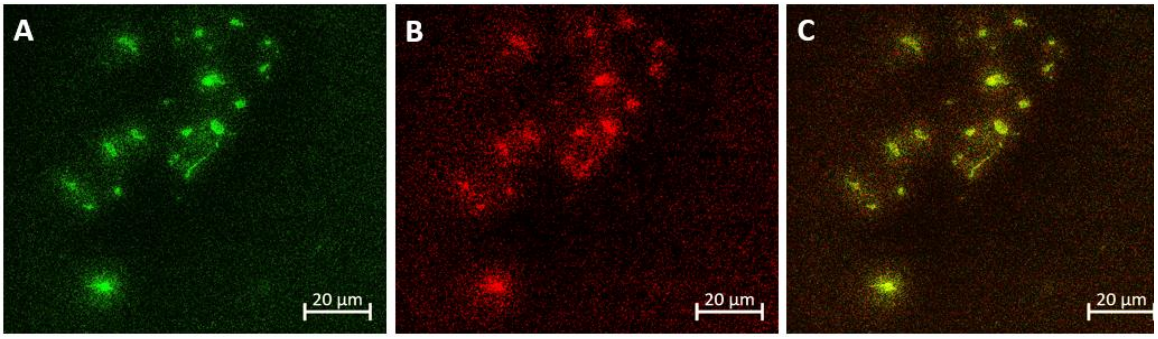

Figure 3.23 Confocal microscope images showing the various channels indicating the composition of agglomerates of aggregates. (Left to Right) A) Channel 1 showing BSA only, B) channel 2 showing FN only, C) combination of both.

3.8 References

1. Samak, M. S. Role of serum albumin aggregation in lubrication and wear protection of shearing surfaces. *MSc Thesis Univ. Ottawa* (2019).

2. Cook, S. G. Mechanism of synovial fluid of lubrication at the molecular and tissue scale. (2019).

3. Andresen Eguiluz, R. C. *et al.* Fibronectin mediates enhanced wear protection of lubricin during shear. *Biomacromolecules* **16**, 2884–2894 (2015).

4. Cook, S. G. *et al.* Dynamics of Synovial Fluid Aggregation under Shear. *Langmuir* **35**, 15887–15896 (2019).

5. Banquy, X., Lee, D. W., Das, S., Hogan, J. & Israelachvili, J. N. Shear-induced aggregation of mammalian synovial fluid components under boundary lubrication conditions. *Adv. Funct. Mater.* **24**, 3152–3161 (2014).

6. Kiselev, M. A., Gryzunov, Y. A., Dobretsov, G. E. & Komarova, M. N. The size of human serum albumin molecules in solution. *Biofizika* **46**, 426–427 (2001).

Chapter 4 – Discussion

4.1 Overview

In this thesis, we have sheared serum albumin (SA) films between model surfaces, and we have investigated in detail the structural changes occurring in the films during the shearing process, which led to aggregate formation. More specifically, we have characterized the dynamics of formation of aggregates, their materials properties, and their role in lubrication and surface protection. For our extensive study, we have used the SFA technique that allowed us to simultaneously (i) apply shear, (ii) record (lateral) friction forces, (iii) quantify film thickness, (iv) establish the presence, size and mobility of aggregates, and (v) measure film refractive index. Additionally, the SFA allowed us to perform normal force measurements prior and post shear to measure the stiffness of the aggregates formed. To distinguish the roles of protein-surface interactions from protein-protein interactions in aggregate formation, we have coated our model surfaces, made of atomically smooth mica, with varied concentrations of fibronectin (FN) and we have used diverse incubation protocols (w/ and w/o surface passivation) prior to shearing the SA films. All other parameters were kept constant to ensure consistency between our measurements: shearing parameters were set at 0.05 Hz shearing frequency and 20V shearing voltage (corresponding to a distance sheared of 70 μm and a shearing velocity of 3.5 μm/sec) while normal loads were kept low at 1–2 mN, corresponding to compressive pressures of 0.5–1 MPa. These parameters were based on previous findings from our group, reporting that they were optimum for systematic aggregates formation.[1] Finally, we used laser scanning fluorescence microscopy to gain information on the composition of aggregates formed. To this end, both SA and FN were labelled with distinct Alexa fluorophores prior to SFA shear measurements, SFA surfaces covered with aggregates (post shear) were then unmounted, dried, and imaged using sequential laser lines. Fluorescence colocalization was then analyzed to assess the presence of either SA and/or FN within the aggregates.

In this Chapter, we first examine the evolution of film thickness and dynamics of aggregation in SA and FN + SA films, in terms of molecular concentrations and conformations. We then discuss in detail the structural (size, shape, distribution), compositional, and mechanical properties of the aggregates formed, in terms of aggregates

density, protein denaturation/unfolding, and molecular entanglement. More specifically, we consider the effect of the linker protein FN (present at the mica surface) on aggregates' mobility and coalescence, namely on the ability of aggregates to either freely move in the shearing junction (and be expelled) or to be trapped in the junction and merge with each other. We also discuss aggregates' longevity and debate the idea of irreversible entangled structures composed either of denatured SA or denatured SA entangled with unfolded/denatured FN. Finally, the last section focuses on the correlation between the above-mentioned aggregates' materials properties and lubrication aspects, by discussing their role in friction and protection of the confining surfaces against wear.

Importantly, as P1 protocols simply consisted in shearing pure SA between bare mica surfaces (without any FN), they were used as controls to determine the role (if any) of FN; while further comparing P2 (0.02 mg/mL FN) with P3 (0.3 mg/mL FN) protocols allowed us to understand whether the role of FN was concentration dependent. Additionally, the role of surface passivation via low concentrations of SA (to prevent nonspecific interactions) prior to shear in larger more physiological SA bulk concentrations was unraveled by comparing our results obtained through P3 (w/o passivation) and P3-P (w/ passivation) protocols using high concentration of FN and P2 (w/o passivation) and P2-P (w/ passivation) using low concentration of FN.

4.2 Evolution of film thickness and dynamics of aggregation

As first reported in Chapter 3 section 3.1.1, when subjected to shear, all SA films undergo shear-induced transformation with sustainable film thickness increase accompanied by aggregate formation, however, the magnitude of film thickening, and the rate of aggregates' formation depend on the protocols used. While the post-shear film thickness for the first three protocols (P1, P2, P2-P and P3) was similar in the range of 110–120 nm, P3-P films exhibited much higher thickness at the end of shear, reaching nearly 300 nm. This difference may be attributed to the presence of high FN concentration at the surface, and to the numerous interactions between SA molecules and the underlying FN layer occurring in P3-P films. However, if this were the case, P3 films (same FN concentration as P3-P) should exhibit similar thickening; instead P3 films overall thickness was more similar to that of P2 films,

forming aggregates even slower than P2. Therefore, it is clear that the passivation process (employed in P3-P but not in P3 protocols) also plays a role in the dynamics of film thickening.

FN is known for its ability to change its conformation depending on physical and chemical factors that directly affect its degree of unfolding and availability of its binding sites. FN + BSA films have previously shown to have reduced film thickness with respect to FN only films. Using similar FN concentrations, Andresen *et al.* reported initial film thickness (D_0) for pure FN films (0.3 mg/mL) to be $61 \pm 16\ nm$ falling down to 39 ± 6 nm in presence of BSA[2], which is within the range of thickness found for P3-P films (here $D_0 = 40.2 \pm 6.5\ nm$). This thickness decrease could indicate either exchange of BSA with FN at the mica surface and/or collapse of the FN layer. Without protein exchange or film collapse, since pure BSA films have a thickness of circa 22 nm, FN + BSA films are expected to be circa 83 nm thick (namely 61 nm + 22 nm). However, FN + BSA films are either 40.2 nm thick (P3-P, following BSA passivation) or 24.2 nm thick (P3, in absence of BSA passivation). Andresen *et al.* ruled out the possibility of protein exchange at the surface since, using Fluorescence Resonance Energy Transfer (FRET) labeling of FN, they reported that, when adsorbed onto curved mica, FN extends and partially unfolds at the surface, which restrains exchange between the large FN molecules (M_w = 250 kDa) already bound onto mica and the smaller BSA molecules (M_w = 65 kDa) added later.[2] FN unfolding is then enhanced upon addition of BSA, as BSA molecules (usually used as blockers of nonspecific interactions) bind to hydrophobic pockets/residues hidden in the core of the secondary structures (modules) of FN and therefore need to unravel these FN modules to access them [3]. As a result, FN + BSA films collapse at the mica surface, greatly reducing film thickness, but the magnitude of film collapse nevertheless depends on the amount of BSA added, or rather on the concentration of BSA solutions to which they are exposed. FN concentrations are identical in P3 and P3-P films, however, P3-P films are twice as thick as P3 films, which can be attributed to a nearly total collapse of the FN + BSA layer in P3 films likely due to complete unfolding of FN. Surprisingly, although one would expect FN unfolding to be commensurate with overall BSA amount added, the exposure of FN to very low BSA concentration (0.02 mg/mL) prior to shearing in highly concentrated BSA (8 mg/mL), called passivation phase, seems to rescue FN from total unfolding and to restrict complete collapse of the FN + BSA layer, which is

why we believe that FN remains only partially unfolded in P3-P films. However, this effect of BSA passivation holds true only when the FN concentration is high. At low concentration of FN even with passivation we do not notice a significant increase in film thickness (as seen in P2 vs P2-P). Low concentration of FN (0.02 mg/mL) with passivation shows an initial film thickness increase difference of ~ 20nm could be attributed to the interaction between the FN+BSA but insufficient amount of FN eventually leads to same aggregate size between P2 and P2-P.

The complete collapse of the FN layer in P3 films promotes the formation of a molecular smooth layer of fully unfolded FN strongly attached to mica, which enables SA to form homogeneous aggregates (comprising mostly SA molecules), likely coexisting with multiple layers of SA molecules. This finding was deduced from both the narrow distribution of aggregates size in P3 films (Fig 3.11) and the visible "steps" measured in force profiles post shear (Fig. 3.18), as discussed further in section 4.3. On the other hand, partial FN unfolding in P3-P films leads to higher film thickness than in P3 films, which in turn facilitates formation of aggregates (likely composed of both FN and SA molecules) through the ingress of new, uncompressed and unsheared SA molecules from the bulk SA reservoir into the sheared junction. Overall, FECO imaging (shown in Chapter II Figs. 3.2, 3.4, 3.6, 3.8) reveals profound changes in all sheared films that evolve from dense and highly viscous fluid films, homogeneously distributed in the entire contacting junction into heterogeneous mixtures composed of 'inhomogeneities' of higher refractive index (discernible as ripples on even FECO fringes that were attributed to the presence of small aggregates) surrounded by a liquid phase. As shear is prolonged, larger aggregates form, which are denser than the bulk SA reservoir and are able to bind to the mica surfaces via specific SA-FN interactions. [1]

Along with exhibiting the highest initial thickness D_0 and the highest thickening ΔD when shear starts, P3-P films are also the fastest to form aggregates (after circa 9 sec) with respect to all other conditions (after circa 20 sec). As shear continues, those aggregates continue growing at the fluid/fluid interface (initially only visible on even FECO fringes) till clear local deformations of the mica surfaces become evident on both even and odd FECO fringes, indicating that they are large enough to obstruct light in the junction. Overall, P3-P films form the biggest and the densest aggregates, likely due to strong interactions between SA and the underlying FN layer leading to entanglement of partially unfolded FN with

numerous SA molecules, a phenomenon well documented before[1,2,4,5]. Whereas shear-induced aggregation rates were similar in P1, P2 and P3 films, suggesting that there was minimal interaction (or none) between SA and the underlying unfolded FN layer in those films.

To further understand the ability of FN to interact with BSA molecules, and the role of such interactions in aggregates formation (and associated lubrication as discussed later), we analysed aggregates mobility during growth by tracking their position through FECO imaging. P3-P films showed maximum migration of aggregates from the middle (where they started forming) to the edges of the shearing junction. More specifically, our results show that, as they grew, these initially small and randomly distributed aggregates tended to gradually align and coalesce to form "strings" resulting in rod-like shaped aggregates oriented roughly 45° with respect to the shear direction. This phenomenon was further confirmed by the full picture of the junction post shear obtained via newton rings at the end of shear. P3 films tended to show similar behaviour with less extreme migration, as we noticed some aggregates at the edges of the sheared junction (Chapter 3 Fig. 3.6). Instead, such migration was neither observed in P1 nor in P2 films, in which aggregates stayed randomly distributed across the contact junction through the whole growth process.

Collectively, our findings indicate that strong FN–SA interactions promote the formation and the growth of large agglomerates through the mobility and coalescence of initially small and fast forming aggregates within the junction. FN–SA interactions affect (i) intra-aggregates forces leading to entanglement between unfolded FN and SA molecules within aggregates, responsible for aggregates high density and rigidity (as discussed later in Section 4.5), and (ii) anchoring/adhesion forces between aggregates and mica surfaces, responsible for aggregates mobility/retention in the shearing junction and associated lubrication (as discussed in Section 4.7).

4.3 Size, distribution, and morphology of aggregates

We performed force runs prior and after shear to estimate aggregates size by comparing the onset of repulsive forces before and after aggregates formation. Onsets of repulsion correspond to the distances between surfaces prior to "contact", in other words, to the thickness of the confined films and/or to the size of aggregates (if any) present in the junction, before compression. The main limitation of such method is that onsets of repulsion

only assess the size of the largest aggregates present in the junction, as they are the ones "touching" first the opposing surface when surfaces are pressed against each other. For such reason, we used a complementary method to visualize all noticeable aggregates at once (via FECO scanning of all cross sections of the sheared zone) to estimate not only their size but also to provide additional details such as their number, location, shape, and overall size distribution. Finally, morphology of aggregates was assessed separately using a top view camera of the junction post shear, although our pics are of low resolution, they allowed us to estimate aggregates overall location and shape.

Overall, onsets of repulsion data post shear (Fig. 3.10) indicate that P3-P aggregates were by far the largest ($386 \pm 26\,nm$) ones, followed by P2 and P2-P aggregates ($252 \pm 6\,nm$ and $247 \pm 12.91\,nm$, respectively) while P1 and P3 films contained smaller aggregates of similar size (in the range of 180–184 nm). This trend in aggregate size was confirmed by our complementary FECO scanning method (Fig. 3.11), which showed that P3-P films contained the largest aggregates ($359.6 \pm 24.4\,nm$), followed by P2-P ($214 \pm 30.8\,nm$), P2 ($184.3 \pm 20.6\,nm$), P3 ($155.9 \pm 7.2\,nm$) and P1 ($121.9 \pm 19.5\,nm$) films, however, our FECO scanning also revealed that P3-P aggregates were extremely heterogeneous in size, followed by P2-P, P2 and P1 (broad distributions), while most P3 aggregates had similar size (very narrow distribution). As mentioned previously in Section 4.2, P3-P films form the biggest aggregates when they are subjected to shear, likely due to strong interactions between SA and the underlying FN layer leading to entanglement of partially unfolded FN with numerous SA molecules. As FN is only partially unfolded (due to passivation of P3-P films), we suspect that many FN molecules are weakly bound to mica surface, and therefore able to (i) detach from the surface when they are bound to SA, (ii) be dragged into aggregates under shear, and (iii) allow aggregates to roll in the junction leading to the formation of elongated rod-like "strings" of aggregates. P3-P aggregates are therefore big as they comprise not only numerous bound SA but also a large quantity of partially unfolded FN that has detached from mica. The broad distribution of P3-P aggregates' size (here size refers to diameter as length was not estimated) can be attributed to variable rolling distances of aggregates from the center (where they form) to the edges (where they grow and coalesce) of the junction, leading to variable ratios of FN versus SA present hence to different sizes.

On the other hand, P3 films form significantly smaller aggregates even though FN concentration at surfaces is the same as in P3-P, likely due to complete unfolding of the underlying FN layer. As FN is fully unfolded (due to absence of-of P3 films), we suspect that most FN molecules are (i) strongly bound to the mica surface on one side, (ii) loaded with a layer of numerous (likely denatured) SA molecules tightly bound to their hydrophobic pockets on the other side, (iii) nearly unable to detach from the surface, even under shear. As a result, P3 aggregates are much smaller than P3-P ones because they comprise only/mostly SA molecules that are dragged into aggregates under shear, leading to the formation of initially small aggregates able to roll on top of a smooth surface made of denatured SA (strongly bound to underlying unfolded FN) and evolving into elongated rod-like "strings". Another sign that P3 aggregates are made nearly exclusively of SA molecules is that their size is very close to that of P1 aggregates (SA only films), with only a difference of 34 nm, which could correspond to the thickness of the extra layer of fully unfolded FN bound to each mica surface in case of P3 films (since the thickness of partially unfolded FN is 39 nm).[2] The narrow size distribution of P3 aggregates is more complicated to explain, however, it is probably linked with the stepwise force run profile detected only in P3 films, namely the presence of numerous vertical jumps synonymous of the formation of molecular layers in the junction. Such behaviour would suggest that small SA aggregates of characteristic aggregate number/size are in equilibrium with SA layers that are expelled one after each other when surfaces are pressed against each other. Such stepwise behaviour reinforces the idea of molecularly smooth surfaces (here made of one layer of denatured SA molecules tightly bound to an underlying fully unfolded FN layer covering the mica), as rough surfaces have been shown to prevent such molecular layering.[6] This phenomenon is discussed in more detail below, in Section 4.4.2 dedicated to aggregates' mobility.

Additionally, our data indicate that P2 aggregates are the second largest aggregates formed under shear. As the only difference between P3 and P2 is the FN concentration, we can only attribute the size difference to different amounts of FN present at the surface, however, higher FN concentrations lead to smaller aggregates, which can appear counterintuitive. This can be easily explained by the fact that, as explained above, when FN concentration is high and no passivation is performed, FN forms a dense (and smooth) layer

of fully unfolded FN molecules tightly bound to the mica surface, ensuring that most aggregates formed are made exclusively of SA molecules. Instead, when FN concentration is low, FN forms a sparce layer (of unfolded molecules as well) at the mica surface. Upon shearing in highly concentrated SA, some FN molecules might exchange and detach from the mica and be dragged into aggregates together with SA. The aggregates formed in P2 films are therefore larger than those found in P3 films because of the presence of unfolded FN even though the ratio of FN versus SA molecules within P2 aggregates is probably much smaller than those found in P3-P films (discussed above in this section). This is further reinstated using P2-P films as they formed aggregates the same size of P2 even with passivation. Aggregate composition is discussed in more details later in Section 4.6.

Regarding aggregates shape, we used a top view camera to capture pics of the entire junction and, although those pics were of low resolution, they allowed us to estimate aggregates overall location and shape. Aggregates in P1, P2 and P2-P films were round and randomly distributed in the junction at all times during the entire shearing experiment (Fig. 3.12). Instead, as previously mentioned, aggregates in P3 and P3-P started as little spheres in the center of the contact and would gradually align in strings of aggregates before finally merging into long rod-like agglomerates. Those strings of aggregates were found longer and extending far beyond the sheared area in P3-P films (Fig. 3.12), suggesting that mobility/rolling and coalescence of aggregates were also affected by the magnitude of FN–SA interactions at the surface, which is discussed in detail in Sections 4.4 and 4.7. Such shear-mediated aggregates' growth mechanism was previously reported in synovial fluid sheared between mica surfaces by Banquy and coworkers as "rolling snowball" mechanism,[5] where small agglomerates would first form and later become large rod-like agglomerates able to roll and orient in the sheared junction.[1,2,4,5]

4.4 Durability and mobility of aggregates

4.4.1 Durability/stability of aggregates

When we quantified the longevity of aggregates to assess their stability over time, we found that all of them, independently on the protocols tested, would subsist 24 hours after surface separation. The aggregates would not dissolve, even after being immersed back in the

droplet of concentrated medium made of 'free floating' SA molecules used as shearing medium. Collectively these results indicate that shear-induced aggregation is an irreversible process, likely because it involves denaturation of proteins promoting their tight and strong binding to each other. This finding reinforces the idea that the aggregates are made of denatured SA and/or denatured SA entangled with unfolded/denatured FN stabilized by strong hydrophobic interactions. Denaturation processes in albumin are well known and have been widely reported, showing that they can lead to the formation of several types of aggregates of varied sizes and density[7]. In our study, denaturation process could have a pure mechanical origin (due to compression and/or shear forces) or an additional thermal origin, as shear generates significant heat increase in the junction (difficult to quantify).

4.4.2 Mobility of aggregates and molecular layering

Although they would not dissolve, aggregates exhibit significant mobility at the surface, either during formation and growth (as mentioned in Section 4.3 in the case of P3 and P3-P films where they migrate and coalesce to form rod-like agglomerates) or after surface separation when they are subjected to new compression (as mentioned for P1 and P2 in Section 3.5).

More specifically, as described in Section 3.5, our FECO analysis of the sheared junction in P1 and P2 films (Fig 3.16 and Fig 3.17) performed prior and after separation of surfaces clearly indicates that surface separation followed by new compression of the films were able to displace significantly the aggregates. This suggests that they are only weakly bound to the surfaces, either because FN (used as an "adhering" agent in all but P1 films) is absent, or because its concentration is too low (0.02 mg/mL) in P2 films to efficiently anchor the aggregates formed to the mica surface. We believe that, in those two cases, pressure and/or shear-induced surface flattening (due to the SFA contact configuration) was responsible for aggregates displacements post-shear in the contacting junction. Interestingly, P3 and P3-P films did not show any sign of aggregates mobility post surface separation, instead, they displayed a different type of migration, as described next. As pointed out in Section 4.3, P3-P films showed maximum migration of aggregates from the middle (where they started forming as little spheres) to the edges of the junction during the shearing phase. As they grew, small and randomly distributed aggregates tended to gradually align and coalesce to form "strings"

resulting in rod-like shaped aggregates oriented roughly 45° with respect to the shear direction. P3 films tended to show similar yet less pronounced migration behaviour (Chapter 3 Fig. 3.6), however, they displayed an additional unique type of mobility phenomenon described below.

As stated in Section 4.2, the normal force runs performed post separation on P3 films exhibited a unique stepwise behaviour (rather than being a continuous repulsive profile as observed in all other films), displaying the presence of numerous steps, i.e., vertical small jumps. The size of these steps was analyzed in detail and found to be $2.2 \pm 0.7\ nm$. This mean step value is particularly interesting because it could correspond to the radius of gyration of single human SA molecules ($2.7 \pm 0.3\ nm$) in aqueous solutions, as reported in various studies. [8–12] Therefore such sequence of identical steps measured in the force runs strongly suggests layering of albumin molecules within the junction, and sequential ejection of single SA layers (likely the layers located at the middle of the film since the external ones are strongly bound to the mica surfaces by FN) when surfaces are slowly pressed against each other. Such arrangement of molecules into layers is rarely observed with proteins, as it requires not only extremely smooth confining surfaces but also very narrow molecular size distribution. We believe that in our case, it is induced by shear and is made possible by the fact that the confining surfaces are smooth enough (FN fully unfolded) to support a molecularly smooth layer of SA bound to it. This stepwise behavior also reinforces the idea that aggregates in P3 are made exclusively of SA molecules.

4.5 Structure and mechanics of aggregates

To assess structure and mechanics of aggregates, we quantified their density and stiffness separately via measurement of refractive index (FECO) and Young moduli (force runs fitted with JKR model), respectively. Our results indicate a clear correlation between density and stiffness in all protocols. P3-P films contained the densest and the stiffest aggregates, followed by P3 films, and finally by P1 and P2 films which contained aggregates with similar low density and low stiffness. These data somehow confirm our previous assumptions regarding the likely structure, conformation and mobility of aggregates. They show that, in P3 and P3-P aggregates, molecular density and stiffness were significantly higher than in P1 and P2 ones, which can be attributed to tighter packing of molecules within P3 and P3-P aggregates. In the case of P3-P films, this tight packing is likely due to the association

of multiple denatured SA molecules entangled with a high number of (partially or fully) unfolded FN molecules, leading not only to high molecular density but also to high rigidity of such aggregates, as unfolded FN is known to exhibit increased stiffness[13]. In the case of P3 films, aggregates were three times more compliant than those found in P3-P films, however, they were nearly ten times stiffer than those in P1 (and P2 films), which is puzzling since we are claiming that they comprise exclusively SA molecules, so they should have similar properties to P1 (SA only films) films. The discrepancy between P3 and P1 could be explained (i) by the presence of the fully unfolded FN layers at the mica surfaces that add rigidity to the system and (ii) by the higher density and layering of SA molecules within aggregates most likely due to low level of denaturation of SA molecules in those films (monodisperse population is a requirement for molecular layering and can only be achieved if most SA molecules retain their secondary/tertiary heart-shaped structure). Finally, P2 aggregates exhibit low density and low stiffness due to low amount of FN present in aggregates (as FN concentration is low, it is easily exchanged/peeled off the mica while shearing) and scarce packing of FN with SA within those rather big structures, unable to roll or coalesce with each other. Instead, P2-P aggregates reveal higher density before shear and after shear, likely due to some effect of the passivation process, even at low FN concentration. The process of passivation could have helped in the entanglement of FN and BSA molecules which otherwise would have collapsed, as it is known that unfolding of FN is induced by SA due to its high affinity towards hydrophobic sites leading to unfolding of FN molecules. Passivation helps in blocking this non-specific interaction.

4.6 Composition of aggregates

Although our study of aggregates' composition via fluorescence confocal imaging is incomplete because it was a complex and challenging experiment, the preliminary data presented in this thesis are promising, as they confirm that aggregates formed in P2 films were composed of both SA and FN molecules. Fluorescent labelling of proteins provides sensitive and robust methods for observing biological process, however, the covalent binding of fluorescent labels to the biomolecules has its disadvantages, as the number of attached fluorophores depends on the protein in use. First, the molecular weight of BSA (65 kDa) is much smaller than that of FN (250 kDa), which translates to much lower amounts of

fluorescent dyes attached to BSA with respect to FN. In such a context, the intensity of the fluorescence measured via confocal microscopy is not an accurate representation of the number of BSA and FN molecules present, but rather of the number of fluorescent dyes bound to the molecules. Second, despite using low concentrations of labelled BSA and labelled FN (solutions would contain 20% of labelled molecules versus 80% of unlabelled ones), there is always a possibility to disturb/destabilize the behaviour of the proteins, not only their folding/unfolding pathway but also their exposure of critical binding sites, both of which could affect the FN–SA aggregation process we attempt to characterize. Third, apart from labelling constrains, locating the very small area sheared (35–40 μm of diameter) within a total surface area of circa 1 cm^2 (overall size of our mica surfaces) was the most laborious step of this experiment and its main limitation, because it required the successive use of 5x, 10x, 20x and finally 40x microscope objectives to localize the sheared location and search for the presence of aggregates. Finally, since the labelling process had to be done prior to SFA experiments that uses continuous white light to monitor interference fringes (FECO) while shearing, the use of fluorescent labels is not ideal as they can (i) reduce the intensity of the FECO detected due to absorbance of the medium, and (ii) be bleached by the white light in use during the SFA experiment, which could then compromise the fluorescent tracking of aggregates. Despite these limitations, our data gave reliable insights on the composition of aggregates for P2. Our sequential fluorescence imaging of P2 aggregates shown in Chapter 3 Fig 3.21 clearly demonstrate that, when merging the fluorescence emitted by BSA (green channel) and by FN (red channel), there is a perfect overlay of both the green and the red channels indicating that both colors perfectly colocalize in space (yellowish result), which means that P2 aggregates are composed of both BSA and FN molecules. This result confirms our assumption that, despite the low concentration of FN, P2 films contain large aggregates composed of both SA and FN due to the scarce and weakly bound layer of FN present at the mica surface, which easily detaches from the mica and rolls along with the aggregating BSA. Note that the size of the aggregates observed in the fluorescence images is not representative of the actual size of the aggregates formed during shear which coexist with the shearing medium (as visualized in FECO and/or measured via force runs). This is because, prior to fluorescent imaging, SFA surfaces had to be separated and dried, which led to merging of existing aggregates into bigger agglomerates due to the capillary forces present upon drying.

4.7 Role of aggregates in friction and wear protection

Last but not least, we monitored the average friction forces (and average friction coefficients) that accompanied the shear transformation of all films, while also keeping an eye on the FECO in order to identify signs of surface damage (if any). Although, in average, the friction coefficients were similar in P1, P2, P2-P and P3 films, namely $\mu \sim 0.5$, P3-P films exhibited a lower coefficient with $\mu \sim 0.4$. Note that P3-P films were also the fastest to exhibit shear transformation, and that they formed the largest and the stiffest aggregates of all films. Together, structure, mechanics and mobility coincide to explain low friction in P3-P films: growth mechanism shows small spherical aggregates being displaced in the contact to form strings of larger aggregates (rod-like agglomerates), suggesting high mobility likely via rolling at the surface. In fact, rolling friction is ensured by (i) low yet substantial adhesion of the aggregates with the surface (preventing slippage), and by (ii) high stiffness of the aggregates which minimizes deformation hence contact area with the surface. The third element that contributes to minimizing the friction is the large size of P3-P aggregates, here ~ 390 nm, which ensures large gap between surfaces during shear and therefore efficient ball bearing lubrication.

P3 films also displayed migration and merging of aggregates into rod-like agglomerates, however, their friction coefficient was higher than in P3-P. This could be attributed to less efficient rolling friction due to (i) lower stiffness of aggregates that deform more upon pressure and increase their contact area with the surface, (ii) smaller size of aggregates, which decreases the gap between shearing surfaces, (iii) lower magnitude of SA–SA interactions at the surface enabling some partial slip instead of pure rolling. As P2 aggregates were larger than P3 ones, we could have expected a lower friction, however, that was not the case probably because they were even more compliant than P3 aggregates, which would restrict rolling even more. Another factor is that P2 aggregates were made a mix of denatured SA entangled with unfolded FN peeled from the surface, and it known that fully unfolded FN acts as a poor lubricant resulting in higher friction. [2] (Note that this could also affect P3 films in areas that are not covered by BSA, exposing unfolded FN at the surface). P2-P aggregates had similar size yet higher density than P2 aggregates, which seems to promote an even higher increase in friction through time. This could be attributed to the lower

effect of BSA passivation when the FN concentration is low, leading to slow and continuous growth aggregates fed by FN peeled from the surface and entangling with SA, as observed in P2.

Here it is important to prompt that no mica surface damage was ever observed during those measurements, at least through the duration of these experiments. This demonstrates the remarkable surface protective abilities of SA films and the role of FN in (i) retaining SA molecules and associated aggregates in the contact, which keeps surfaces well separated at all times and (ii) ensuring rolling of aggregates, which lowers the friction and promotes overall better lubrication and protection.

4.8 Proposed mechanisms

In this short section, we propose qualitative views/mechanisms of aggregates formation that summarize our data, in terms of film organization and molecular concentration/conformation. Figure 4.1 proposes shear-induced transformations occurring in P1 (BSA only) films. Panel A shows the mica surface following incubation with BSA (green structures), in which few BSA molecules are (weakly) bound to mica, while most of them are free floating in the shearing medium. Note that all BSA molecules retain their heart-shaped folded conformation. Panel B shows the surface as shearing starts, evolving to a heterogeneous mixture of small aggregates composed of both heart-shaped and denatured (elongated) molecules coexisting with free floating and few surface-bound BSA.

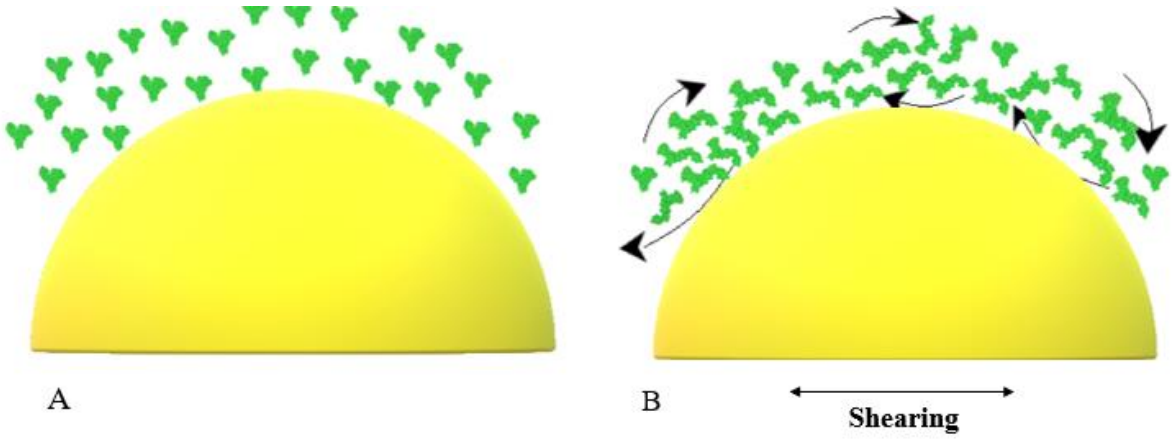

Figure 4.1 Schematics of proposed mechanism for BSA only (P1) films. Side view of mica surface (A) before shear and (B) while shearing. Green: BSA.

Figure 4.2 proposes shear-induced transformations occurring in P2 (BSA + low FN concentration, w/o passivation) films. Panel A shows the mica surface following incubation with FN (red) then BSA (green), in which FN is unfolded due to the binding of some BSA while other BSA molecules are (weakly) bound to mica due to the low concentration/coverage of FN. Finally, most BSA is free floating in the shearing medium. Panel B shows the surface as shearing starts, evolving to a heterogeneous mixture of bigger aggregates composed of both heart-shaped and denatured (elongated) SA molecules as well as some unfolded FN that has detached from the mica. Aggregates are large but heterogeneous in size and ratio of FN versus SA is low. The mechanisms by which P2-P films formed aggregates were similar to that for P2 films. Despite forming denser aggregates (likely due to tighter molecular binding), the size of aggregates and friction forces measured in P2 and P2-P films were identical, which was attributed to the ability of unfolded FN to detach from the mica and feed aggregates together with (likely unfolded) SA.

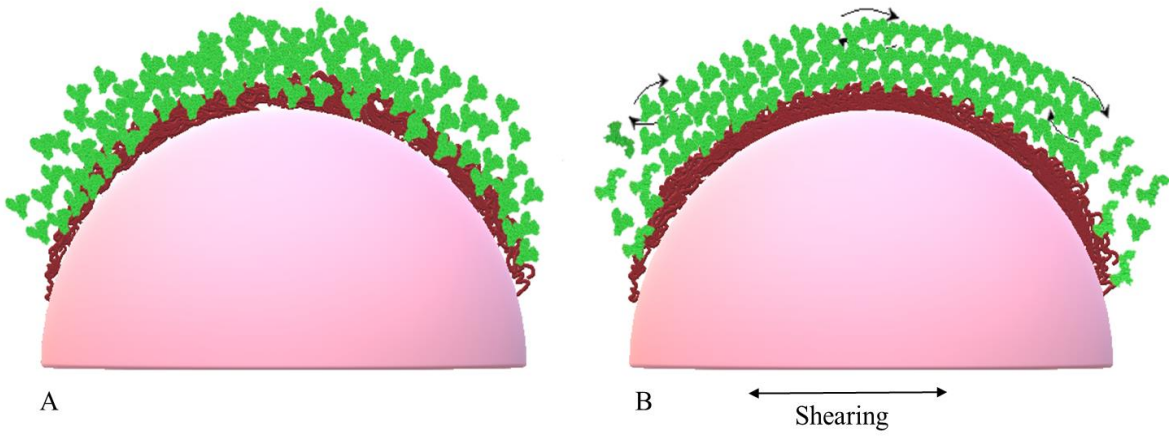

Figure 4.3 Schematics of proposed mechanism for $BSA + FN_{0.3}$ w/o passivation (P3) films. Side view of mica surface (A) before shear and (B) while shearing. Green: BSA; Red: FN.

Figure 4.3 proposes shear-induced transformations occurring in P3 (BSA + high FN concentration, w/o passivation) films. Panel A shows the mica surface after incubation with large amounts of FN (red) followed directly by large amounts of BSA (green), in which fully unfolded FN is now covering and tightly bound to the entire mica surface (on one side) while bound to a dense layer of BSA molecules, likely denatured (on the other side). No BSA is bound to mica and most BSA is still free floating in the shearing medium. Panel B shows the

surface as shearing starts, evolving into a homogeneous mixture of small aggregates composed exclusively of SA molecules that can easily roll at the surface, coexisting with layers of heart-shaped SA molecules that can be expelled from the junction when surfaces are slowly pressed against each other.

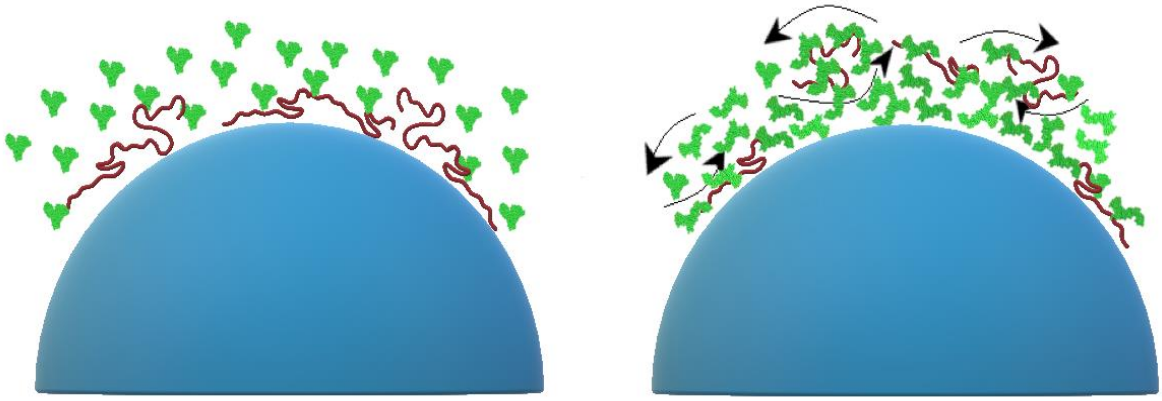

Figure 4.2 Schematics of proposed mechanism for $BSA+FN_{0.02}$ $(P2)$ films. Side view of mica surface (A) before shear and (B) while shearing. Green: BSA; Red: FN.

Figure 4.4 proposes shear-induced transformations occurring in P3-P (BSA + high FN concentration, w/ passivation) films. Panel A shows the mica surface following a 3-steps incubation with (i) large concentration of FN (red), (ii) very low amount/concentration of BSA (passivation phase), and (iii) large amount of BSA (shearing medium). Here the passivation phase was able to rescue FN from complete unfolding: partially unfolded FN is covering the entire mica surface (on one side) while bound to BSA molecules (on the other side). No BSA is bound to mica and most BSA is still free floating in the shearing medium. Panel B shows the surface as shearing starts, evolving to a heterogeneous mixture of very large and dense aggregates composed of SA molecules strongly bound and entangled to a large amount of partially unfolded FN that has detached from the mica. Aggregates are large (but heterogeneous in size), and ratio of FN versus SA is high, which confers high aggregates' stiffness and overall better separation between surfaces.

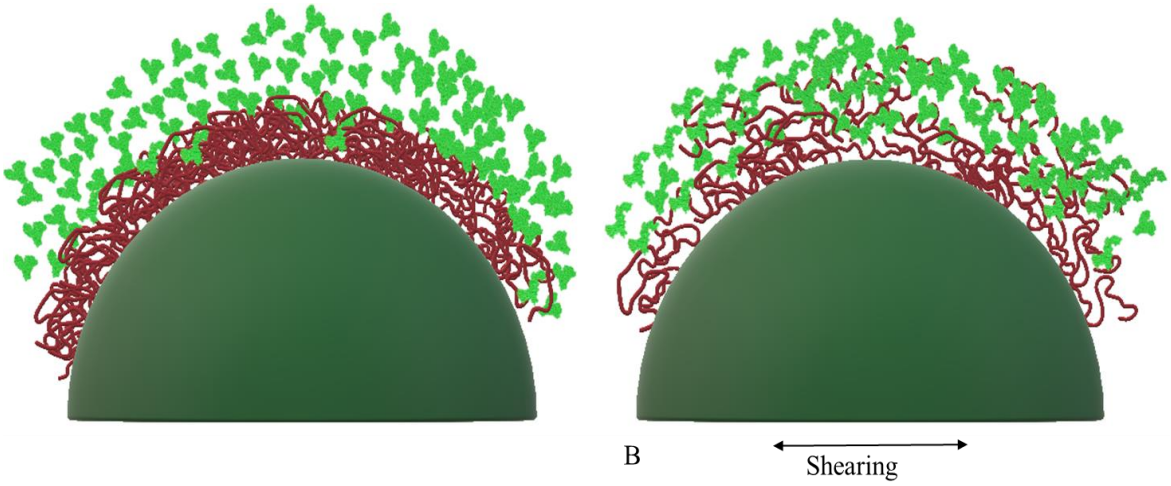

Figure 4.4 Schematics of proposed mechanism for $BSA + FN_{0.3}$ w/ passivation (P3-P) films. Side view of mica surface (A) before shear and (B) while shearing. Green: BSA; Red: FN.

4.9 Still unclear and what experiments do you propose to clarify mechanisms.

Despite investigating individual characteristics of SA and FN, more confocal microscopy experiments are needed specially to assess the composition of aggregates in both P3 and P3-P films. This would help us establishing a better correlation between composition, structure and friction of aggregated films in general, and also understanding if FN and BSA contribute equally in producing large, dense aggregates in P3 (unexpected) and P3-P (expected) films. Additionally, freeze drying of the contact junction post shear followed by a technique such as atomic force microscopy (AFM) or scanning electron microscopy (SEM) to image aggregates would enable precise understanding of individual aggregate shape, size, and even alignment. AFM could also be complementary in better understanding the adhesion and mobility of aggregates at the surface, although those experiments are expected to be highly challenging, as they would require keeping SFA surfaces in the shearing liquid while transferring them to the AFM liquid cell for imaging. Finally, collecting all aggregates formed and performing x-rays or light scattering would allow us to have a more precise idea of aggregate structure.

4.10 References

1. Cook, S. G. *et al.* Dynamics of Synovial Fluid Aggregation under Shear. *Langmuir* **35**, 15887–15896 (2019).

2. Andresen Eguiluz, R. C. *et al.* Fibronectin mediates enhanced wear protection of lubricin during shear. *Biomacromolecules* **16**, 2884–2894 (2015).

3. Little, W. C., Schwartlander, R., Smith, M. L., Gourdon, D. & Vogel, V. Stretched extracellular matrix proteins turn fouling and are functionally rescued by the chaperones albumin and casein. *Nano Lett.* **9**, 4158–67 (2009).

4. Samak, M. S. Role of serum albumin aggregation in lubrication and wear protection of shearing surfaces. *MSc Thesis Univ. Ottawa* (2019).

5. Banquy, X., Lee, D. W., Das, S., Hogan, J. & Israelachvili, J. N. Shear-induced aggregation of mammalian synovial fluid components under boundary lubrication conditions. *Adv. Funct. Mater.* **24**, 3152–3161 (2014).

6. Israelachvili, J. & Gourdon, D. Putting liquids under molecular-scale confinement. *Science* **292**, 867–868 (2001).

7. Borzova, V. A. *et al.* Kinetics of thermal denaturation andaggregation of bovine serum albumin. *PLoS One* **11**, 1–29 (2016).

8. Kiselev, M. A., Gryzunov, Y. A., Dobretsov, G. E. & Komarova, M. N. The size of human serum albumin molecules in solution. *Biofizika* **46**, 426–427 (2001).

9. Gekle, M. Renal tubule albumin transport. *Annu. Rev. Physiol.* **67**, 573–594 (2005).

10. Tojo, A. & Kinugasa, S. Mechanisms of glomerular albumin filtration and tubular reabsorption. *Int. J. Nephrol.* **2012**, (2012).

11. Peters, T. Serum Albumin. *Adv. Protein Chem.* **37**, 161–245 (1985).

12. Tay, M., Comper, W. D. & Singh, A. K. Charge selectivity in kidney ultrafiltration is associated with glomerular uptake of transport probes. *Am. J. Physiol. - Ren. Fluid Electrolyte Physiol.* **260**, 549–554 (1991).

13. Klotzsch, E. *et al.* Fibronectin forms the most extensible biological fibers displaying switchable force-exposed cryptic binding sites. *Proc. Natl. Acad. Sci. U. S. A.* **106**, 18267–18272 (2009).

Chapter 5 – Conclusions and future directions

5.1 Main conclusions

Current approaches that seek to elucidate the remarkable lubrication of synovial fluid usually focus on the roles of hyaluronic acid and lubricin and frequently overlook the role serum albumin (SA) although it represents 90% of the protein content of synovial fluid. In this thesis, we have combined the Surface Forces Apparatus (SFA) with confocal microscopy to investigate the tribological and structural properties of SA films when sheared between model mica surfaces, coated (or not) with a layer of the linker protein fibronectin (FN) of varied concentration and conformation.

Our data indicate that, when they are sheared, all SA films are able to replicate the transformation previously reported for synovial fluid, i.e., they exhibit abrupt film thickening and formation of numerous long-lived aggregates accompanied by low friction and efficient surface protection against damage. More specifically, our investigation of varied FN coatings and incubation protocols (w/ and w/o BSA passivation) reveals that:

(i) Strong anchoring of SA to shearing surfaces via FN not only accelerates aggregation but also promotes the formation of denser and stiffer aggregates that enable efficient rolling friction (third body / ball bearing lubrication), which keeps surfaces apart and ensures prevention against damage.

(ii) The resulting structure and composition of aggregates depend on the concentration and conformation of the FN layer used to coat the mica surfaces: high FN concentrations followed by SA passivation promote the formation of large and dense aggregates made of denatured SA tightly bound to partially unfolded FN that has detached from mica. Instead, high FN concentrations without SA passivation lead to complete unfolding of FN and promote the formation of smaller and more compliant aggregates made exclusively of SA, while FN stays firmly attached to the mica.

(iii) Aggregates formation is the result of shear alignment, shear stretching of both SA and FN molecules that have lost (partially of fully) their initial conformations, i.e., have unfolded due to combined mechanical and thermal effects. Such aggregation mechanism is therefore largely irreversible, which makes aggregates very stable and long-lived in the contact.

5.2 Extending our findings to joint and implant lubrication

As mentioned in Chapter I, mica is atomically smooth, rigid and non-porous, which makes it structurally and mechanically different cartilage, which is heterogeneous, rough, compliant and highly porous. Because of these differences, caution must be used in generalizing our findings beyond rigid surfaces. Nevertheless, using these model surfaces allows us to evaluate accurately the structure-tribology relationship of thin lubricating films by ensuring that all shear-induced events measured can be attributed to changes in the interfacial lubricant, i.e., to phenomena occurring at the junction *between* surfaces rather than *within* surfaces. Our results are therefore applicable to other tribosystems involving rigid surfaces, in particular most artificial joints.

Nevertheless, although articular joints are complex multi-component systems and therefore difficult to model at the molecular level, our SFA approach could also be seen as a way to reduce such complex tribosystem to a 'single asperity' whose dimensions would be similar to those found in cartilage. Typically, surface asperities in cartilage have a height of 1–10 μm and a mean distance between asperities from 1–50 μm. Under pressure, these asperities are expected to deform and reach a contact area of 20 to 100 μm in diameter, which are exactly the geometrical characteristics of the 'single asperity' junction that can be attained with the SFA using mica surfaces as model surfaces. Hence the advantage of using mica is that, in contrary to the cartilage surface, any shear-induced changes in the interfacial fluid between contacting asperities can be accurately observed.

In this context, the formation of large and long-lived aggregates associated with the efficient surface protection we observed in SA films indicates that globular proteins may play a prominent role in the aggregation phenomena previously reported in the literature for synovial fluid. Additionally, while the formation of aggregates in synovial fluid and the

development of wear-protecting “protein gels” in fetal bovine serum had been previously observed in separate studies, our findings correlate both phenomena by suggesting that SA aggregation and surface protection against damage are intimately connected, and that this connection might be at the heart of the highly efficient lubrication of synovial fluid. Our results are applicable to various rigid systems such as artificial joints, in which the dynamic aggregation of SA may play a pivotal lubricating role by providing an ‘on demand’ wear protecting protein cushion in response to high normal loads and shear stresses. Although it will be of future interest to investigate SA aggregation between cartilage-mimicking surfaces to elucidate its role in natural joints, the identification of a self-replenishing, shear-induced lubricating mechanism mediated by the aggregation of globular proteins advances our current understanding of joint implants’ lubrication with implications for future design and therapeutic interventions.

Therefore, in the future, our technique could be used for systematic characterization of adsorption, aggregate formation, and lubrication of protein films on a variety of implant materials with different surface properties to advance our understanding of structure-function relationship of protein films and improve both the design and the materials properties of artificial joints.